University of Alberta

Investigation of Nanofluidics Using Molecular Dynamics Simulation

by

Cunkui Huang

A thesis submitted to the Faculty of Graduate Studies and Research in partial fulfillment of the requirements for the degree of **Doctor of Philosophy.**

Department of Mechanical Engineering

Edmonton, Alberta

Fall 2007

Your file Votre référence
ISBN: 978-0-494-32979-5
Our file Notre référence
ISBN: 978-0-494-32979-5

Abstract

In this thesis, molecular dynamics (MD) simulations were applied to study fluid transport through two nano devices (i.e., a membrane and a nanosyringe) and fluid properties in isothermal-isobaric (NPT) ensembles.

To mimic a pressure-driven flow through a finite length channel, a novel non-equilibrium molecular dynamics (NEMD) simulation approach was proposed in this thesis. The major feature of this method is that the constant but different level pressures in two reservoirs are generated by using two self-adjusting plates on which two external forces/pressures are exerted. This method has been examined and found that it works well. Using this method and the conventional continuum theory, a comparative study between continuum and atomistic approaches was performed in a nano-scale system. Simulation results show that the Naveir-Stokes (N-S) equations under no-slip boundary conditions can be used to predict fluid transport through the channel approximately if the solid wall-liquid have the neutral-like interactions.

Fluid transports through two different nanosyringes were studied by using an injection method in this thesis. First, the transport mechanism of fluid in a small nanosyringe was investigated by using a liquid in which no ions were present. The NEMD simulation results elucidate unexpected wavelike liquid transport motion in the nanosyringe. Second, the effect of the extra-pairwise positive/negative ions on fluid motion and ion distributions in the channel was investigated

in a larger nanosyringe. The simulation results show that the extra-pairwise positive/negative ions have significant influence on both fluid motion and ion distributions in the channel of the nanosyringe.

The NEMD simulation method proposed in the study was extended to investigate the fluid properties in NPT ensembles by applying two equal external pressures on the two self-adjusting plates. This method was examined by performing equilibrium molecular dynamics (EMD) simulations in two different NPT ensembles. The EMD simulation results showed that this method works well. Using this method and the approach applied in canonical (NVT) ensembles commonly, the role of attractive force or cutoff distance was studied in both NVT and NPT ensembles. The EMD simulation results exhibit that the attractive force plays important roles on determining thermodynamic properties.

ACKNOWLEDGEMENTS

During this work, I have been in contact with many individuals, and it is their help by various means that makes this work possible.

First of all, I would like to express my deep gratitude to my supervisors, Prof. Larry Kostiuk and Prof. Phillip Choi (Chemical and Materials Engineering), for their guidance, help, encouragement and support during the period of my Ph.D. program.

I would also like to thank my previous supervisors, Prof. Krishnaswamy Nandakumar (supervisory committee member at present) and Prof. Daniel Y. Kwok (presently at the University of Calgary), for their initial guidance and support. I am also indebted to the professors in the Examining Committee: Profs. Jeff Chen, Payam Rahimi and Andre McDonald, for taking time out from their busy schedules to read my thesis and attend my examination.

I am grateful to my former and present colleagues in our research group for generously sharing their expertise and experience with me. I would also like to thank the financial supports from the Ph.D. Scholarship at the University at Alberta, the Postgraduate Scholarship from NSERC, the Walter H Johns Graduate Fellowship at the University of Alberta, and the Department of Mechanical Engineering (teaching and research assistantships).

Last but certainly not least, a deep gratitude to my family, especially my wife Xiaoli and my daughter Veeda, is perhaps a standard, but nevertheless a truly meant one.

Table of Contents

List of Figures

NOMENCLATURE

A ..... cross-section area

a ..... acceleration; coefficient

b ..... coefficient

BC ..... boundary condition

D ..... dimensions

D_s ..... self-diffusion coefficient

$DCV - GCMD$

dual-control-volume grand-canonical molecular dynamics

dt ..... time step

EMD ..... equilibrium molecular dynamics

$\overrightarrow{\mathbf{F}}$ ..... force

g^* ..... gravity

$g(r)$ ..... radial distribution function

k_b ..... Boltzmann's constant

K_w ..... stiffness of spring

m ..... particle mass

M ..... number of molecules in self-adjusting plate

MD ..... molecular dynamics

MSD ..... mean square displacement

N ..... particle number

N_D ..... number of dimensions

NEMD .... non-equilibrium molecular dynamics

NPH ..... isoenthalpic-isobaric ensemble

NPT ..... isothermal-isobaric ensemble

NS ..... Navier-Stokes equation

NVE ..... microcanonical ensemble

NVT ..... canonical ensemble

P ..... pressure

q ..... charge

Q ..... parameter of the mass of heat bath

r ..... radial distance

R ..... radius

r_c ..... cutoff distance

r_{ij} ..... intermolecular distance

t ..... time

T ..... temperature

Tr ..... trace of stress tensor

u ..... velocity

V ..... volume

$\overrightarrow{V}$ ..... velocity

WCA ..... WCA theory proposed by Weeks, Chandler and Andersen

$\mathbf{x}$ ..... position

$\mathbf{y}$ ..... position

$\mathbf{z}$ ..... position

ε ..... molecular energy scale; fluid permittivity

ϵ_0 ..... dielectric permittivity of vacuum

ϵ_r ..... relative permittivity of liquid

κ ..... compressibility

λ ..... scaling factor used in Berendsen thermostat

μ ..... dynamic viscosity

ν ..... kinematic viscosity

ξ ..... friction coefficient used in Nose-Hoover thermostat

ρ ..... density

ρ_n ..... number density

σ ..... molecular length scale; stress tensor

τ ..... characteristic time of Lennard-Jones potential

ϕ ..... intermolecular potential

$\forall$ ..... volume

CHAPTER 1

INTRODUCTION

Nanofluidics is often defined as the study and application of fluid flow in and around nanosized objects [1]. The development of new technologies, e.g., the invention of new tools (atomic force microscopy, scanning tunneling microscopy, etc.) and explosive growth of computer power over last few decades, have made the study of nanofluidics by either experiments or numerical simulations much more accessible. Molecular dynamics (MD) simulation is a powerful method, initialed in the late 1950s by Alder and Wainwright [2–4], that has been used to study nanofluidics by many researchers.

1.1 Fluid Transport through a Finite Length Nanopore

Fluid transport through a finite length nano channel plays an important role in many natural phenomena and industrial processes [5–21] including protein translocation, DNA transfer across nuclear pores, gene swapping between the guest and host bacteria through pili [5–10, 13–18], membrane separation of mixtures [19, 20], electrokinetic micron size channel battery [21], etc. The transport properties of fluid in such small confined channels, for example the size of channel less than 10 molecular diameters, deviate from their bulk behaviors and

the continuum or Newtonian hypothesis may not be valid [1, 22–25]. In this case, MD simulation was used as a powerful method to study various phenomena, such as DNA and RNA transport through finite length nanopores [5, 7–9], liquid transport/diffusion through membrane [11, 19, 22, 26–32], Couette flow [33–41], Poiseuille flow [24, 25, 34, 36, 42–49], etc. Using this method, many new phenomena have been found, such as oscillatory distribution of density in the direction normal to solid wall [24, 25, 34–38, 43, 44, 46, 50–52], fluid slip with solid surfaces [33, 35, 36, 43], stick-slip motion in boundary lubrication [53], etc. But there are still huge challenges in this area waiting to be understood.

Several non-equilibrium molecular dynamics (NEMD) algorithms have been developed to deal with fluid transport through a finite length nanopore whose ends are connected to two reservoirs. The approaches most commonly used at present are the external-field driven NEMD simulation [26, 29, 44] and dual-control-volume grand-canonical molecular dynamics (DCV-GCMD) simulation [19, 27, 31, 54–61]. In the first method, an external force, such as gravity-like force or electrical force, is exerted on each particle (electric field in the case of charged particles) and causes them to be transported through the channel. The pressure fields in the reservoirs (located at the front and back nanopore), generated by this method, is not a constant but a function of distance in the force direction. Zhu et al. [29] used this approach to generate a pressure difference across a membrane and investigated the water transport through the membrane by either applying an external constant force to all water molecules or only to those water molecules located outside of the channel. Their results show that the flux of water through the membrane for the first case is 1.6-3.5 times of the second one, i.e., the flux is not a unique function of the pressure gradient. Therefore, more research work was still needed in order to model a pressure-

driven transport through a finite length channel accurately. The second method (DCV-GCMD) utilizes the difference in the chemical potentials (or densities) in two reservoirs to induce fluid transport through a channel. For this approach, there are some deficiency. First, particle insertion and deletion is required to maintain constant, but different level chemical potentials (or densities) in the two reservoirs. Inserting and deleting particles would disturb the dynamics of the system [27], especially for a dense system. Secondly, there is an open question on how to assign the velocities of molecules which are inserted in the control volumes. In literature [54, 55, 58, 59], some authors added a streaming velocity to the thermal velocity of newly inserted molecules in order to eliminate the discontinuity of the flux which would occur at the boundary of the control volumes, while others did not. Theoretically, adding a streaming velocity to the molecules which are inserted in the control volumes is reasonable. However, the streaming velocity in the control volume depends on the position where molecules are inserted. Actually, the streaming velocity is an unknown value in the control volumes. Using the average value calculated from the flux by some authors is a reasonable approximation, but still induces some uncertainties.

1.1.1 A Novel Pressure-Driven NEMD Method

In practice, fluid transport through a finite length channel driven by a constant pressure gradient is one of common cases faced in science and engineering problems. The methods described previously, however, are not suitable to describe the process of a pure pressure driven flow. In this thesis, an alternative approach [62, 63] is proposed to mimic this practical situation, i.e., fluid transport through a finite length nanopore (e.g., nanopores in a membrane) driven by a constant pressure gradient. The main feature of this novel method is that the

constant pressure fields in the front and back reservoirs, which are connected to the inlet and outlet of the nanopore, are generated by using two self-adjusting plates on which two external forces/pressures are exerted. The advantages of this method are that it overcomes the disadvantages existed in the external-field driven NEMD simulations and the DCV-GCMD method, and functions well for dense systems. This method not only can be used to study monatomic flows, but also suitable to investigate multi-component flows, such as diluted DNA or polymer molecules suspending in a solvent being transported through a finite length nanopore driven by a constant pressure difference or a combination of pressure difference with electrical field.

To demonstrate this novel approach, non-polar liquid argon was chosen as the working medium. Simulations with a fixed upstream pressure and four different back pressures were carried out under the same solid wall-liquid interaction. The detail description of the method and results will be provided in Chapter 3.

1.1.2 Effect of Solid Wall-Liquid Interaction on Liquid Transport

The effect of solid wall-liquid interaction on fluid transport through small confined channels has been studied by many researchers, for example, Couette flow [33, 38, 40, 51, 52, 64] and Poiseuille flow [25, 34, 37, 42, 64]. In these papers, periodic boundary conditions were applied on the stream-wise direction, which implies steady state flows in infinite length channels. However, the effect of solid wall-liquid interaction on liquid motion through a finite length channel has received little attention.

The pressure-driven NEMD method [62], proposed in this thesis, was applied to study fluid transport through finite length channels. This method was

improved by modifying the formations of two self-adjusting plates and applied to investigate the effect of solid wall-liquid interaction on the flow behavior in a modeled cylindrical nanopore with finite length. The method, results and discussion will be addressed in Chapter 4.

1.1.3 Effect of Entrance and Exit on Liquid Transport

In many earlier MD works involving Couette flow [33–38] and Poiseuille flow [24, 25, 34, 36, 42, 43, 46, 47], periodic boundary conditions were typically used. The results correspond to a steady state flow through an infinite length channel. Such an approach, however, is not suitable to describe the process of fluid transport through a finite length nanopore due to the effects of the entrance and exit of the channel, and the changes of fluid properties in flow direction on fluid transport not to be taken into account. Zhang et al. [19] indicated that the entrance effect of fluids into pores plays an important role in mass transfer and separation process for membrane separation. However, there are few articles published on this issue. Actually, this effect on fluid transport through a nanopore increases as the ratio of length to diameter of the nanopore decreases. Therefore, studying the mechanism of fluid transport through a nanopore that has small ratio of length to diameter, such as a nanopore in a membrane, is important for researchers to better understand many natural phenomena.

To isolate the effect of entrance and exit on liquid transport through a nano-sized channel, two different approaches were applied in this thesis. The first one was the improved pressure-driven NEMD method proposed by author in this thesis, which is applied to carry out the fluid transport through a finite length nanochannel. The other is the external-field driven NEMD simulation which

was used to calculate the fluid motion in an infinite length nanopore (using periodic boundary condition). Two different solid wall-liquid interactions, one weak (the energy scale of solid wall molecules is smaller than that of liquid) and the other neutral (the energy scales for both solid wall molecules and liquid are same), were simulated by using these two different approaches. The NEMD simulation results will be discussed in Chapter 5.

1.1.4 Comparative Study between Continuum and Atomistic Approaches

The classical continuum theory based on the Navier-Stokes (NS) equations assumes that state variables do not vary appreciably on a length scale comparable to the molecular mean free path [65]. However, significant fluctuations in fluid density have been observed in the direction normal to the solid wall by experiment [66] and MD simulations [35, 36]. Consequently, the assumption in the classical NS approach breakdown. However, MD studies on Poiseuille flow indicated that the classical NS behavior can still be a reasonable approach for modeling channel sizes of 10 molecular diameters and greater [23–25, 64]. Todd and Evans [48] carried out the NEMD simulation for a fluid confined to a channel width of 5.1 molecular diameters, they found that the streaming velocity distribution was consistent with that predicted by the classical NS theory, while a different result in the same size channel was found by Travis and Gubbins [25]. Qiao and Aluru [65], in a study of electroosmotic flow, even found that the continuum flow theory could be used to predict bulk fluid flow in channels as small as 2.22 nm, provided that the viscosity variation near the wall was taken into account. From the above studies, one sees that the applicability of NS equations for modeling nano channel flow remains an open problem as many system

parameters remain unexamined.

In conventional NS simulations of macroscopic systems, density and viscosity are two bulk fluid properties that are functions of temperature and pressure. Moreover, no intermolecular interaction between the channel material and the fluid exists. The channel wall acts as a physical boundary at which the fluid velocities normal and tangential to the channel wall are typically set to zero (impenetrability and no slip boundary conditions). In Chapter 6, this conventional approach was applied despite the scale of the system being modeled. The objectives of this study were to compare the results between conventionally applied continuum models based on NS equations to those based on NEMD simulations for the prototypical problem of liquid argon flowing through a finite length nanopore that connects two semi-infinite reservoirs. These reservoirs were held at constant, but different pressures, to establish a steady state flow situation. The basis of the comparison includes the gross measure of the total flow rate through the channel, as well as the more refined descriptors, such as the distributions of pressure, density and velocity in axial and radial directions. The variables manipulated in the NS and NEMD computations were the pressure in the downstream reservoir (for a fixed upstream reservoir pressure), and the magnitude of the intermolecular potential between the liquid and the solid, which makes up of the channel wall. The conclusions, though restricted to the tested case of a finite length cylindrical pore that has a diameter 2.2 nm and length 6 nm, highlight general principles under which the conventional continuum methods are suitable or not to predict the liquid transport through nanopores.

1.2 Nanomedicine: Injection Flow in a Nanosyringe

1.2.1 Flow Mechanism through a Nanosyringe

Application of nanotechnology for treatment, diagnosis, monitoring and control of biological systems has recently been referred to as "nanomedicine" [67, 68]. Research in this area focuses on the identification and transport of precise targets to the appropriate nanocarriers to achieve the required responses. While active research is currently underway for the former, the latter on transport mechanism for nanosyringes is rarely found [67, 68]. In most earlier MD studies, the geometry was a confined channel with periodic boundary conditions; the driven force was a gravity-like force which was exerted on all fluid molecules. This implies that molecules in the channel are dominated by two different kinds of forces, i.e., one is a constant external force and the other is the intermolecular forces. However, a fluid in a nanosyringe is only governed by intermolecular forces. Therefore, the conventional MD method with periodic boundary conditions is not suitable for the study of fluid in a nanosyringe.

In Chapter 7, MD simulations were used to model the transportation of Lennard-Jones liquid in a nanosyringe by using an injection boundary condition. This procedure mimics the physical operation of liquid flow in a macroscopic syringe. To the best of my knowledge, injection flow inside a nanosyringe has not been studied by MD simulation. Hence, it is the focus of this work to examine the liquid transport properties in a nanosyringe with a constant injection velocity boundary condition.

A circular geometry is selected, due largely to its ease of molecular formation and similarity in geometry with physical systems [69]. In chapter 7, both isothermal and adiabatic flows with constant injection velocity were examined.

The NEMD simulation results and discussion will be presented in Chapter 7.

1.2.2 Effect of Extra-Pairwise Positive/Negative Ions in a Nanosyringe

Most solid substances acquire a surface electric charge when they are brought into contact with an aqueous medium. So, electrically neutral liquids have a distribution of electrical charges near the solid surface. This region, known as the electrical double layer (EDL) [50, 70–75], induces electrical phenomena. For long-range Coulombic interactions in a system with periodic boundary conditions, the methods most commonly used are the Ewald summation [13, 76–79] and related techniques, such as the particle mesh Ewald method [75, 80, 81] and the particle-particle particle-mesh method [72, 82]. Daiguji [83] used the Poisson-Nernst-Planck equations, a continuum theory, to investigate the ion transport in nanofluidic channels with height of 30 nm, and concluded that when the channel size is smaller than the Debye length and the channel surface is charged, the channel becomes a unipolar solution of counterions at a concentration that neutralizes the surface charge; the co-ions are essentially repelled from the channel. Qian and Aluru [84] used the continuum modeling based on Poisson-Boltzmann equation and the MD simulations to study the ion concentrations and velocity profiles in nanochannel. In their studies, only counter-ions are present in the channel. They found that the Poisson-Boltzmann theory fails to predict the ion distribution near the channel wall accurately in a channel with a height of 3.49 nm, and the continuum flow theory breaks down in the entire channel for electroosmotic flow in a channel with height 0.95 nm. Thompson [85] also used the MD method to study the electro-osmotic flow in a charged nanopore of diameter 4 nm. In the channel, only counterions and

monotonic non-polar solvent molecules are present. In practice, extra-pairwise positive/negative ions may exist in the channel. Therefore, studying the effect of extra-pairwise positive/negative ions to understand the mechanism of fluid motion through nanosyringes is important.

In Chapter 8, four different cases, i.e., no ions present in liquid, only counterions present in liquid, counterions combining with low concentration of extra-pairwise positive/negative ions present in liquid, and counterions combining with high concentration of extra-pair positive/negative ions present in liquid, were carried out. The Coulomb's law and 12-6 Lennard-Jones potential were used to govern the interaction between ion-ion, ion-liquid, ion-solid, liquid-liquid and liquid-solid molecules.

1.3 Study of Fluid Properties at Equilibrium

1.3.1 A Method for MD Simulations in Isothermal-Isobaric Ensemble

In practice, different systems are often subjected to different conditions. The typical systems encountered in science and engineering are the microcononical (NVE), canonical (NVT) and isothermal-isobaric (NPT) ensembles. The first two have been well studied by many researchers [86–95]. For the third ensemble, it has been regarded as the most difficult to create as the simulation strategy must be able to simultaneously generate instantaneous kinetic energy and pressure fluctuations. Therefore, developing a method that can implement MD simulations in the NPT ensemble easily and robustly is desirable.

The method most commonly used to generate NPT ensemble is so called "extended-phase-space" approach [92, 94, 96–100], in which extra degrees of

freedom are introduced into a system in order to ensure the trajectory generated follow the statistical distributions corresponding to the desired thermodynamic conditions. Andersen [94] was the first researcher to develop such a method. He proposed a Lagrangian in which the volume V acts as an additional variable; pV as an additional potential term to the Lagrangian so that the trajectory average of any property is equal to the isoenthalpic-isobaric (NPH) ensemble average of the properties. Different from the Lagrangian approach, Hoover and other authors [96, 99, 101, 102] proposed the use of Hamiltonians to perform MD simulations in NPT ensembles. Recently, a non-Hamiltonian method was developed by Tuckerman et al. [99, 103] Introducing extra variables into a system can achieve fluctuation mathematically, while the real physical meaning is not clear due to the fact that the motions of molecules described by such equations do not represent a real system. Moreover, introducing more extra variables results in a computational system to be more complicated. Berendsen [89] developed a simple and efficient method, called weak coupling to an external bath, in which a constant pressure was accomplished by re-scaling particle's positions and coordinates at every time step by a factor.

In this thesis, an alternative method based on a physical phenomenon observed in macroscopic systems to perform molecular dynamics simulations in an NPT ensemble is proposed. The major advantage of this algorithm, compared with other methods, is that no extra degrees of freedom are introduced to the system. To test the validity of the method, two systems with different number of molecules (one with 5,150 molecules and the other 10,406 molecules) were performed. The results show that an NPT ensemble can be easily created in which the energy, pressure and the system volume fluctuate simultaneously.

1.3.2 Role of Attractive Force in Molecular Dynamics Simulation

The WCA theory, a perturbation theory, developed by Weeks, Chandler and Andersen [104–107], has been applied to study liquid structures and thermodynamic properties by many researchers [108–112]. In this theory, there are two key assumptions: the first is that the intermolecular potential can be split into the short-ranged repulsive portion and the longer-ranged attractive portion; the second is that the effect of the attractive portion in determining the liquid structure is negligible. As a result, the liquid structure and its thermodynamic properties are determined by a radial distribution function $g_0(r)$ of a repulsive reference liquid that is related to the hard sphere liquid. Weeks et al. compared the $g_0(r)$ obtained from a repulsive reference fluid and $g(r)$ obtained by molecular dynamics (MD) simulations [113]. The agreement between $g_0(r)$ and $g(r)$ is excellent for the system at a high density. At present, the repulsive part of the intermolecular potential proposed in the WCA theory has been referred to as the WCA potential and used frequently in molecular simulations [25, 44, 48, 112, 114–118].

The major difference between the WCA potential and the Lennard-Jones potential is that the former does not include the attractive part, while the latter accounts for its effects. Travis et al. [25] studied the Poiseuille flow of Lennard-Jones fluids in narrow slit pores. They calculated the streaming velocities in the pore by using the WCA potential and the Lennard-Jones potential (truncated at 2.5σ) separately. Their results show that the streaming velocity distributions obtained by two different potentials are not consistent, which was interpreted as that ignoring attractive forces in the WCA potential impacts the fluid transport through the narrow pores. To gain further insights into the effects of attractive force on liquid properties (e.g., density, temperature, pres-

sure and the relationship among them), two ensembles, one canonical (NVT) and the other isothermal-isobaric (NPT) ensembles, were applied in this thesis. The results for a high density NVT ensemble show that the attractive force has an insignificant influence to the radial distribution function $g(r)$, which is consistent with the assumption used in WCA theory. However, the corresponding pressure calculated from the NVT ensemble was found to be strongly dependent on the attractive force. Ignoring the contribution of the attractive force on the pressure calculation will lead to incorrect results, e.g. pressure calculated in NVT ensembles and density simulated in NPT ensembles. The results obtained from the NPT ensemble indicate that all properties of a liquid, including the radial distribution function $g(r)$ and thermodynamic properties, depend significantly on the attractive force. It means that the WCA theory is not suitable for use in NPT ensembles.

The organization of this thesis is as follows: In Chapter 2, the theoretical formalisms used in MD simulations will be introduced briefly; In Chapters $3 \sim 5$, the pressure-driven NEMD method proposed in this thesis and applications of this method used to study different situations will be addressed in detail, e.g. the effect of solid wall-liquid interaction, the impact of entrance and exit on liquid transport through a finite length nanochannel. In Chapter 6, the results obtained by the MD simulations will be compared with those calculated using the continuum theory (Navier-Stokes equations) and the valid conditions under which the conventional Navier-Stokes equations can be used in a nano-sized channel will be extracted. The fluid transport in nanosyringes will be discussed in Chapters 7 and 8. In Chapter 9, a method, extended from the pressure-driven NEMD approach that can be used to perform equilibrium molecular dynamics (EMD) simulations in NPT ensembles, will be discussed. Chapter 10 will show

a systematic study of the role of attractive forces in MD simulations. Finally a brief summary and future work will be introduced in Chapter 11.

Chapter 2

Theoretical Formulations used in Molecular Dynamics Simulation

In MD simulations, the motion of molecules is governed by Newton's second law. The interactions between two molecules, e.g., liquid-liquid, liquid-solid, ion-ion, ion-liquid, ion-solid, are dominated by either the Lennard-Jones 12-6 potential or the Coulomb's law. The equations of Lennard-Jones 12-6 potential and Coulomb's law are

$$\phi_{ij}^{LJ} = 4\varepsilon_{ij}\left[\left(\frac{\sigma_{ij}}{r_{ij}}\right)^{12} - \left(\frac{\sigma_{ij}}{r_{ij}}\right)^{6}\right] \tag{2.1}$$

$$\phi_{ij}^{C} = \frac{q_i q_j}{4\pi\epsilon_0\epsilon_r r_{ij}} \tag{2.2}$$

where ϕ_{ij}^{LJ} and ϕ_{ij}^{C} are the Lennard-Jones and Coulomb potentials, respectively; σ_{ij} and ε_{ij} are characteristic length and energy scales; r_{ij} is the distance between two interacting molecules; q_i and q_j are the partial atomic charges; ϵ_0 and ϵ_r are the dielectric permittivity of vacuum and the relative permittivity of liquid. If molecules i and j belong to the same component, e.g. liquid, σ_{ij} and ε_{ij} correspond to σ_{ll} and ε_{ll}, respectively; if molecules i and j are of different types,

e.g. one is solid and the other is liquid, σ_{ij} and ε_{ij} correspond to σ_{ls} and ε_{ls} which are calculated based on the Lorentz-Berthelot combining rule [119]. To reduce computational requirement, a truncation algorithm for the Lennard-Jones potential is used in all simulations.

For each molecule on the wall, a stiff Hookean spring attaches it to its lattice position with a potential of

$$\phi_{spring} = \frac{1}{2} K_w R^2, \tag{2.3}$$

where K_w is the stiffness of spring and R is the distance of the wall molecules from their lattice sites. To keep the displacement of wall molecules at low level, a large constant stiffness, $K_w = 6000\varepsilon_l\sigma_l^{-2}$ [51], was chosen in this work.

The equations of motion were integrated using a Velocity Verlet algorithm. To prevent a pair of molecules from overlapping or passing through directly in one iteration, two criteria of time step were adopted in NEMD simulations: (1) $dt = a \times \tau$, where a is a coefficient and can be selected between 0.001–0.005; $\tau = (m\sigma_{ll}^2/\varepsilon_{max})^{1/2}$ is the characteristic time of the Lennard-Jones potential, where m is the mass of molecule; (2) $dt = b \times (\sigma_{min}/v_{max})$, where b is a constant and was selected between 0.001–0.01; v_{max} is the maximum relative velocity between two interacting molecules. The second criterion guarantees no interacting molecules overlapping or passing through each other directly in one iteration. In NEMD simulations, the smaller one was chosen as the effective time step and its range was $0.1 - 1\ fs$.

Temperature is one of the important issues in MD simulations, especially for NEMD simulations. If a system has a periodic boundary condition in the flow direction, it can be interpreted as a steady flow (or time independent flow)

in an infinitely long channel. In this case, thermostats have to be applied to release the extra energy added into the system by the external force and also by error accumulations, such as gravity-like force used in NEMD studies. In this thesis, Berendsen thermostats [72, 84, 89] or Nose-Hoover thermostats [90–93, 120, 121] were coupled to the system to mimic isothermal flow (i.e., constant temperature). In the Berendsen algorithm, the instantaneous temperature is pushed toward the desired temperature by scaling the velocity at each step. The scaling factor is given by the following equation

$$\lambda = [1 + \frac{dt}{\tau_T}(\frac{T_0}{T} - 1)]^{1/2} \tag{2.4}$$

where dt is the time step used for numerically integrating the Newtonian's equations of motion; τ_T is a preset time constant; T is the instantaneous temperature and T_0 is the desired temperature. The instantaneous temperature is calculated from,

$$\frac{N_f k_b T}{2} = \sum_i^N \frac{m_i \overrightarrow{\mathbf{u}}_i^2}{2} \tag{2.5}$$

Where k_b is the Boltzmann constant; N is the number of particles in a system; N_f is the total freedom of the system (e.g., $N_f = 3N$ for 3-dimensional problem); $\overrightarrow{\mathbf{u}}_i$ is the peculiar velocity of i^{th} molecule.

In the Nose-Hoover thermostat, Newton's equations of motion are modified as

$$m_i \dot{\overrightarrow{\mathbf{v}}}_i = \overrightarrow{\mathbf{F}}_i - \xi m_i \overrightarrow{\mathbf{v}}_i \tag{2.6}$$

$$\dot{\xi} = \frac{1}{Q}(\frac{T}{T_0} - 1) \tag{2.7}$$

where m_i and $\dot{\overrightarrow{\mathbf{v}}}_i$ are the mass and acceleration of the i^{th} particle; $\overrightarrow{\mathbf{F}}_i$ are the total force acting on the i^{th} particle; ξ is a friction term in the equations of

motion; Q is a parameter of the mass of heat bath, and control the speed of response of the heat reservoir.

The self-diffusion coefficient can be calculated using the Einstein equation [122–125] that is expressed as

$$D_s = \frac{1}{2N_D(t-t_0)}\langle|\vec{\mathbf{r}}_i(t) - \vec{\mathbf{r}}_i(t_0)|^2\rangle \tag{2.8}$$

which is valid in the limit that $(t - t_0) \rightarrow \infty$. In the equation, N_D is the dimensions (N_D = 1, 2 or 3 for 1-, 2- or 3-dimensional problem); $\vec{\mathbf{r}}_i(t)$ is the position of the tracer particle at time t; $\vec{\mathbf{r}}_i(t_0)$ is the location of the tracer particle at initial time t_0 chosen in simulations; the angular bracket denotes ensemble averaging. The term, $\langle|\vec{\mathbf{r}}_i(t) - \vec{\mathbf{r}}_i(t_0)|^2\rangle$, is called the mean square displacement (MSD).

The self-diffusion coefficient can also be calculated using time-dependent velocity autocorrelation function, known as Green-Kubo relation [28, 122, 123]. The mathematical expression of this relation is

$$D_s = \frac{1}{N_D}\int_0^\infty \langle\vec{\mathbf{v}}_i(t)\cdot\vec{\mathbf{v}}_i(0)\rangle dt \tag{2.9}$$

where $\vec{\mathbf{v}}_i$ is the velocity of i^{th} molecule.

The stress tensor for a microscopic system of particles is calculated by the Irving-Kirkwood method [126]. In this approach, the stress tensor components consist of two parts, a kinetic part and a configurational part. The equation is

$$\sigma_{\alpha\beta} = -\frac{1}{\forall}\langle\sum_i^N m_i u_{i\alpha}u_{i\beta} + \sum_i^N\sum_{j>i}^N r_{ij\alpha}F_{ij\beta}\rangle \text{ (if } i \in \forall \text{)} \tag{2.10}$$

where $\forall$ is the volume of the computational box defined; N is the total number

of molecules, including those in the images if the system has periodic boundary conditions; m_i is the mass of i^{th} molecule; $u_{i\alpha}$ and $u_{i\beta}$ are the peculiar velocity components of molecule i in the α and β directions; $r_{ij\alpha}$ is the component of the distance vector between molecules i and j in α direction; and $F_{ij\beta}$ is the component of the force between molecules i and j in β direction. In MD simulations in this thesis, N is a molecular number in an enlarged volume by extending computational box in each direction one cutoff distance due to the truncating algorithm used. The first and second terms of right-hand side in the above equation describe the kinetic contribution and the configurational or potential contribution, respectively.

The constitutive pressure is defined as the trace of the stress tensor:

$$P = -\frac{1}{3}Tr(\sigma_{\alpha\beta}) \tag{2.11}$$

Dynamic viscosity, according to the linear response theory, can be expressed as a time integral of a microscopic time-correlation function in equilibrium stage [127], and is calculated by the following equation,

$$\mu = \frac{\forall}{k_b T}\int_0^\infty \langle \sigma_{\alpha\beta}(t)\sigma_{\alpha\beta}(0)\rangle dt \tag{2.12}$$

where k_b is the Boltzmann constant; T is temperature.

The time-averaged density and streaming velocity in the channel are calculated by counting volume fraction instead of an entire molecule, i.e. each molecule is divided into several pieces by the grids. Each piece for a signed molecule has different volume fraction, but same velocity in different cells formed by grids. The advantages of this method is that it can quickly obtain the density and streaming velocity profiles, especially for a small system with finite number

of molecules. The time-averaged number density is expressed as

$$\overline{\rho}_{ij} = \frac{\sum_{l=1}^{M} \sum_{k=1}^{N} f^{k}{}_{ij}(dt)_l}{\forall_{ij} \triangle t} \tag{2.13}$$

where i and j are the index numbers of the grid in axial and radial directions; M and N are the iteration number and total molecules in the system; f_{ij}^{k} is the volume fraction of the k^{th} molecule in grid i and j; $(dt)_l$ is the time step at the l^{th} iteration; $\forall_{ij}$ is the volume of grid i and j and $\overline{\rho}_{ij}$ is the averaged number density in grid i and j in period $\triangle t$.

The streaming velocity is calculated by

$$\overline{V}_{ij} = \frac{\sum_{l=1}^{M} \sum_{k=1}^{N} f^{k}{}_{ij} v_z^k (dt)_l}{\forall_{i,j} \overline{\rho}_{ij} \triangle t} \tag{2.14}$$

where v_z^k is the velocity component of k^{th} molecule in z direction; $\overline{V}_{ij}$ is the streaming velocity at grid i and j in period $\triangle t$.

Chapter 3

Molecular Dynamics Simulation of a Pressure-Driven Liquid Transport Process in a Cylindrical Nanopore Using two Self-adjusting Plates

[note: this chapter is closely related to the published work in the Journal of Chemical Physics 124, 234701 (2006)]

3.1 Molecular Dynamics Simulation and Methodology

The problem considered models a nanopore membrane (based on a regular array of channels) of finite thickness that separates two semi-infinite reservoirs. The pressures in the reservoirs were to be maintained at fixed, but different, levels to cause flow through the membrane. To make this problem computationally tractable, the flow through just one of the channels in the membrane was simulated. The channel was a nominally straight cylinder with dimensions of 2.2 nm and 6 nm for the inside diameter and length, respectively. Fig. 3.1 shows the modeled problem geometry in the context of a single snapshot of the NEMD simulation. A Cartesian coordinate system was placed so that the z-axis was

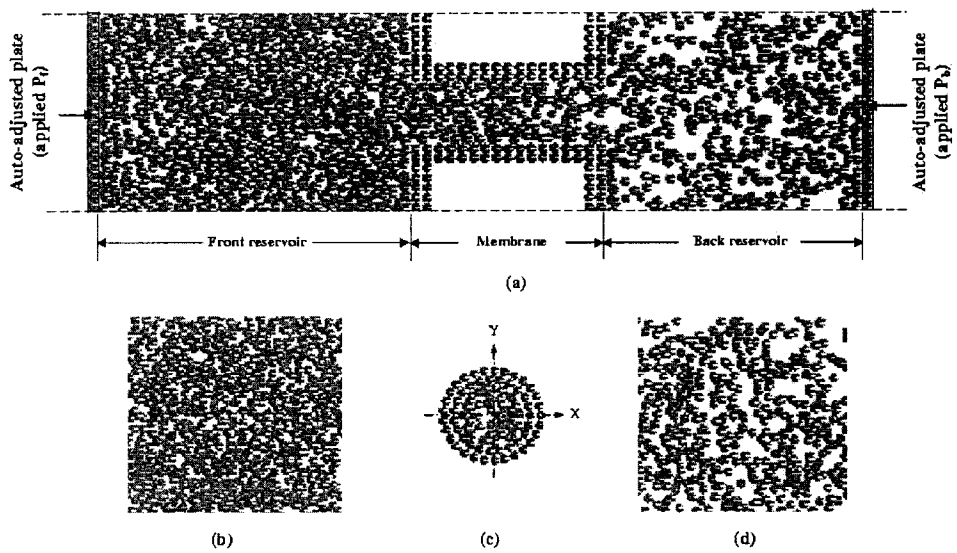

Figure 3.1: Snapshot of single nanopore in a membrane. (a) vertical section through axis of nanopore, (b) cross-section at the middle of the front reservoir, (c) cross-section at the middle of nanopore, (d) cross-section at the middle of back reservoir.

aligned with the centerline of the channel, and the x and y-axes were aligned to the centers of the neighboring channels in the array.

The fluid used in the simulations was made up of 15,088 argon molecules. The solid substrate that defines the membrane boundaries was constructed from two layers of molecules with the same properties as the fluid except that they (2,132 of them) were more or less fixed at their respective lattice positions using very stiff spring constant. Boundary conditions in the fluid reservoirs exploit the periodic arrangement of channels in the x and y-directions, while far field conditions were applied in the z-direction. Using periodic boundary conditions at specified x and y locations establishes some of the limits of the computational domain, but also implies a prescribed spacing of channels in the membrane. For all the calculations performed, the domain lengths in the x- and

y-directions were set at $L_x = L_y = 7\ nm$. As a result, the membrane studied had a porosity of approximately 8 percent, so the channels were essentially independent of each other. The fluid flow far from the inlets or outlets of a membrane can be approximated as one-dimensional and laminar. The approach taken to model these far-field boundaries was to introduce rigid plates, oriented normal to the z-axis, into each of the reservoirs that can move with the flow in the z-direction. These plates also define the limits of the computational domain in the z-direction for the NEMD calculations. The fluid outside the domain was replaced by uniformly distributed forces on the plates equal to the pressures specified for each reservoir. The one-dimensional and laminar flow far from the channel inlet and outlet was achieved computationally by allowing the z-location of the plates to independently self-adjust to maintain the desired reservoir pressures and densities. To reduce the impact of these plates on the fluid around them, they were formed from one layer of molecules with the same properties as the fluid, but with a number density large enough to prevent fluid molecules from penetrating out. To prevent these plates from distorting, an averaged-force component in the z-direction on plate molecule i,

$$\overline{f}_{zi} = (\sum_{i=1}^{M} \sum_{j=1}^{N} f_{zij} + AP_{ext})/M, \tag{3.1}$$

was exerted on each molecule in the front or back self-adjusting plate, where M and N are the numbers of molecules in the self-adjusting plate and in the liquid, respectively; f_{zij} is the z-component force acting on i^{th} plate molecule produced by j^{th} liquid molecule; A is the cross-section area of the reservoirs and P_{ext} is the external pressure exerted on front or back self-adjusting plate. During the simulation it is important that these plates remained far away from

the channel inlet and outlet in order for them not to influence the flow through the channel. Ensuring that these plates did not affect the flow will be explored in the results and discussion section of this chapter.

The initial conditions for the simulation were established by introducing a rigid, impenetrable, no thickness plate across the mid-length of the channel in order to separate the upstream and downstream parts of the flow. The two self-adjusting plates and the molecules in the system were allowed to move until the desired pressures in each of the reservoirs reached thermodynamic equilibrium. During this period, the Berendsen thermostats [65, 72, 89] were coupled to adjust the temperature of the system to be $Tk_b/\varepsilon_l = 1.1$ ($T = 133\ K$), where k_b is the Boltzmann constant and ε_l is the liquid energy scale. Finally, the separation plate was removed and the molecules from the two sides were allowed to transport by pressure differences. The disturbances produced by removing the separation plate was not large due to the small cross section of the channel compared to the reservoirs.

The motion of these spherical liquid molecules is governed by Newton's second law. In earlier external-field driven MD works [25, 34, 36, 42], there were two kinds of forces in Newton's equation, one was the external force applied uniformly on each molecule; the other was the Lennard-Jones force due to the interaction between molecules. In this study, a pressure-driven flow which was only dominated by the interactions between molecules in the channel was modeled. The interactions between liquid/liquid and solid/liquid are governed by a truncated and shifted Lennard-Jones 12-6 potential:

$$\phi(r_{ij}) = 4\varepsilon_{ij}\left[\left(\frac{\sigma_{ij}}{r_{ij}}\right)^{12} - \left(\frac{\sigma_{ij}}{r_{ij}}\right)^{6}\right] - \phi(r_c) \text{ (if } r_{ij} \leq r_c) \tag{3.2}$$

where $\phi(r_c)$ is the truncated Lennard-Jones potential at $r_{ij} = r_c$. The truncated distance used in this thesis was 2.2σ [35, 42], i.e., $\phi(r_{ij}) = 0$ if $r_{ij} > r_c$. In this thesis, liquid argon was chosen as working medium. Its length and energy scales are $\sigma_l = 0.34\ nm$ and $\varepsilon_l = 1.67 \times 10^{-21}$ J [128], respectively.

To model a molecule on a solid wall, a stiff Hookean spring attaches it to lattice position with a potential expressed by equation 2.3. The stiffness used in this equation was, $K_w = 6000\varepsilon_l\sigma_l^{-2}$ [51].

The equations of motion were integrated using a Velocity Verlet algorithm. The effective time step applied in simulations was about $0.1 \backsim 1.0$ fs that depends on the maximum relative velocity between two interacting molecules.

In NEMD simulations, temperature is one of the important parameters. In the present work, we modeled an isothermal flow through a membrane. So, to avoid the effect of temperature on the liquid moving and keep the temperature constant, four Berendsen thermostats [65, 72, 89] were coupled to the system separately, i.e., in the front reservoir, middle nanopore, back reservoir and solid substrate. Four thermostats made the temperatures in each part of the system to be consistent.

The constitutive pressure is defined as minus one-third of the trace of the stress tensor. The stress tensor in this study was calculated by the Irving-Kirkwood method [126].

3.2 Validation and Selection of Parameters

3.2.1 Validation

Before performing the fluid transport through a confined channel, a validation of the MD code was carried out. In this part, MD simulations in a canonical

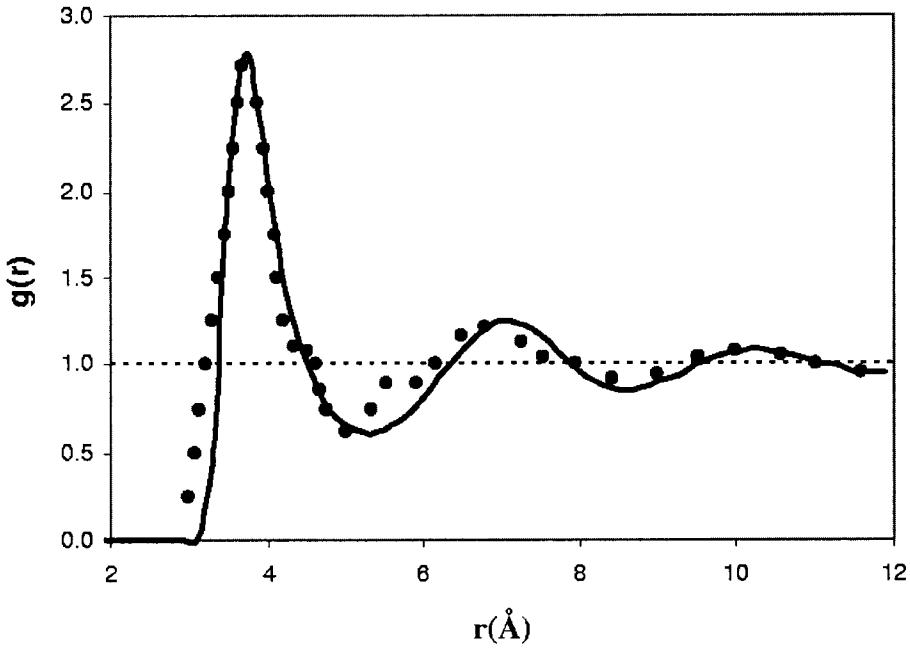

Figure 3.2: Comparison of the radial distribution function of liquid argon obtained by MD simulation (solid line) with Eisenstein and Gingrich's x-ray experimental measurement (filled symbol) at $T = 91.8\ K$ and $\rho = 1.3664\ g/cm^3$.

(NVT) ensemble, i.e., a system consisting of 2,597 argon molecules filled in a cube that was subjected to periodic boundary conditions in x, y and z directions, were performed. Two characteristics of liquid argon, radial distribution function at density $\rho = 1.3664\ g/cm^3$ and temperature $T = 91.8\ K$ and self-diffusion coefficient at $\rho = 1.374\ g/cm^3$ and $T = 90\ K$, were chosen to compare with experimental results. In these simulations, the length and energy scales for liquid argon were $\sigma_l = 0.3405\ nm$ and $\varepsilon_l = 1.67 \times 10^{-21}\ J$, respectively; the time step was 0.5 fs. Fig. 3.2 shows the comparison of the radial distribution function between MD prediction and Eisenstein and Gingrich's experimental measurement [129, 130]. One sees that MD simulation successfully captures the

properties of molecular distribution with respect to distance and the agreement between them is fairly good. The self-diffusion constant can be calculated using Green-Kubo relationship or Einstein equation. Both methods were used and it was found that the two results were consistent, and hence only the latter is presented. In three dimensions, the Einstein equation is expressed as

$$D_s = \frac{1}{6(t - t_0)} \langle | \vec{\mathbf{r}}_i(t) - \vec{\mathbf{r}}_i(t_0) |^2 \rangle \tag{3.3}$$

which is valid in the limit that $(t - t_0) \rightarrow \infty$. Fig. 3.3 shows the mean square displacement of liquid argon obtained at $\rho = 1.374\ g/cm^3$ and $T = 90\ K$ by averaging 1,000 different initial times t_0. The self-diffusion constant, slope of the curve in Fig. 3.3 divided by 6, is $2.38 \times 10^{-5}\ cm^2/sec$. The experimental measurement [131] is $2.43 \times 10^{-5}\ cm^2/sec$. The difference between them is about two percent. These two validating tests show that this MD code works well and can be used to predict the liquid transport properties through a nanopore in a membrane.

3.2.2 Selection of Parameters

In this proposed method, the key parameters besides the energy and length scales, diameter and length of nanopore, include the pressures (P_f and P_b) exerted on the front and back self-adjusting plates, the distances (L_{zf} and L_{zb}) of the plates to the inlet and outlet of the nanopore. To extract a signal from substantial thermal noise in small systems with short time, Koplik et al. [34] studied the external force exerted on each molecule in a force-field driven flow carefully. They found that the value of gravity $g^* = O(0.1)$ in Lennard-Jones units makes molecules in a nanochannel move at an average velocity $u^* = O(0.1)$

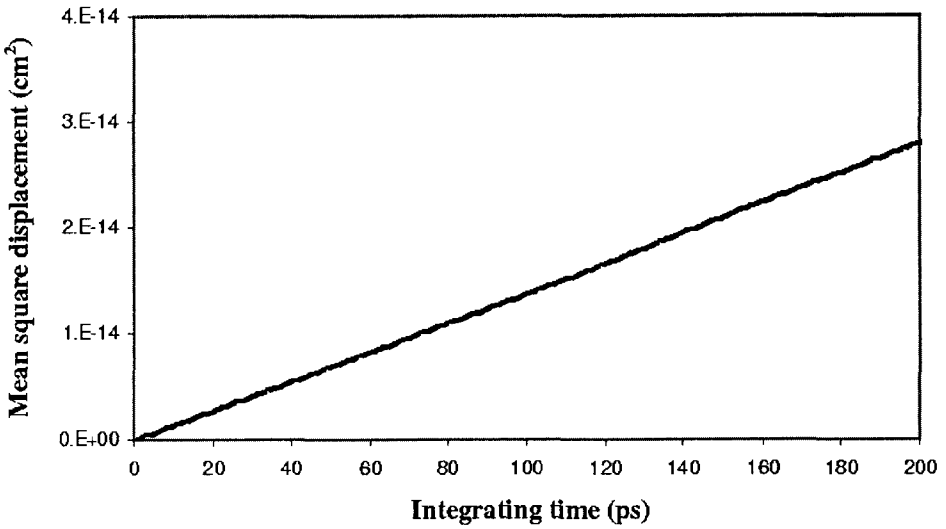

Figure 3.3: Relationship between the mean square displacement of liquid argon and integrating time at $T = 90\ K$ and $\rho = 1.374\ g/cm^3$.

and a Reynolds number $R_e \leq O(1)$. In the present study, this g^* value was used to determine the pressures applied on the self-adjusting plates, i.e., the applied pressures generate the same order of gravity ($g^* = O(0.1)$) on each molecule in the nanopore. The average gravity on each molecule was estimated by the following equation,

$$g^* = \frac{(P_f - P_b)\sigma_l}{10^{27} L \rho_n \varepsilon_l} \tag{3.4}$$

where L and ρ_n are the length of the nanopore and the number density ($1/nm^3$) of liquid molecules in the pore, respectively. In the above equation, the pressure in each reservoir was assumed to be identical and equal to the pressure applied from outside. For liquid argon, a number density, $21/nm^3$ ($\rho = 1.4\ g/cm^3$), was used to estimate g^*. P_b, so called the back pressure, varies from the value of P_f to zero. So, the maximum gravity is a value obtained by the above equation at $P_b = 0$. In this work, $P_f = 80\ MPa$ was chosen, which means $g^*_{max} = 0.13$. In

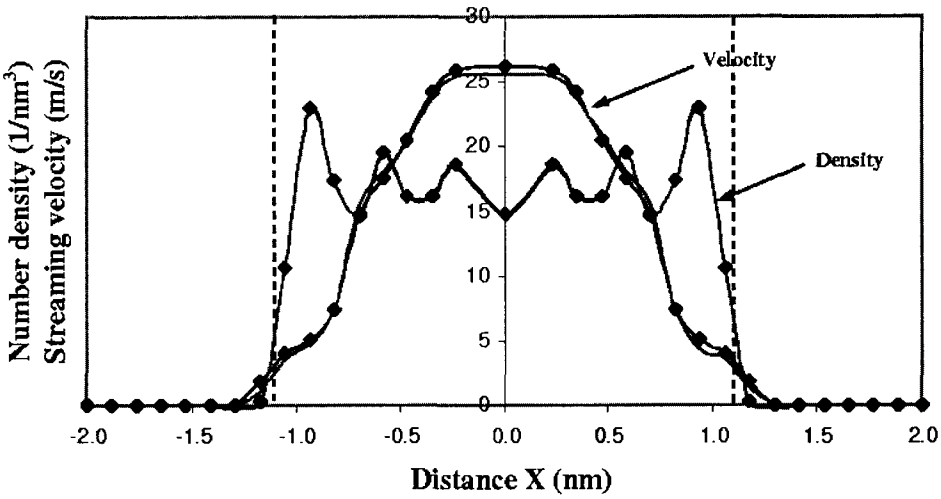

Figure 3.4: Comparisons of number density and streaming velocity distributions obtained in two different periods for case 2; period 1: $L_{zf} = 10.86 - 10.45\ nm$ and $L_{zb} = 5.96 - 6.64\ nm$ (line with symbol ♦); period 2: $L_{zf} = 9.74 - 9.33\ nm$ and $L_{zb} = 7.66 - 8.34\ nm$ (line without symbol). Dashed lines are the internal surface of nanopore.

practice, P_b is not zero, for example, $g^* \approx 0.1$ if $P_b = 0.2P_f$.

The entrance effect of fluids into pores plays an important role in mass transfer and separation processes for membrane separation [19]. In this study, the front and back self-adjusting plates were placed far away from the inlet and outlet of the nanopore to reduce their influence on liquid transport in the pore, while still accounting for entrance and exit effects. The distance for the front self-adjusting plate to the inlet of the pore, L_{zf}, was controlled to be larger than $8.8\ nm$ during simulations. But the distance, L_{zb}, varied from $5.1\ nm$ to $30.6\ nm$ because the volume disturbed by the exit velocity in the back of the nanopore depends on the pressure drop, i.e., large pressure drops produce large disturbed area around the exit of the nanopore. To verify the effect of L_{zf} and L_{zb} on the fluid transport, the case with $P_f = 80\ MPa$ and $P_b = 10\ MPa$ was chosen as

an example, and the time-averaged results obtained during $L_{zf} = 10.86 - 10.45$ nm and $L_{zb} = 5.96 - 6.64$ nm (called period 1, average time $\triangle t = 500$ ps) were compared with those obtained in $L_{zf} = 9.74 - 9.33$ nm and $L_{zb} = 7.66 - 8.34$ nm (called period 2, averaged time $\triangle t = 500$ ps). Fig. 3.4 shows the comparisons of density and velocity distributions with respect to radius during two different periods. In this figure, the solid lines without symbols stand for the results obtained in period 1; the solid lines with symbol ♦ expresses results calculated in period 2. The density distributions in the two different periods are exactly the same; the difference between two streaming velocity distributions is small and negligible. This example shows that the impact of distance L_{zf} and L_{zb} on fluid transport through a nanopore is minor if L_{zf} and L_{zb} are chosen larger than the lengths used in these tests.

3.3 Results and Discussion

3.3.1 NEMD Results

To test whether this proposed method can produce a constant pressure difference across a membrane, four cases with different back pressures, $P_b = 4$, 10, 20 and 40 MPa (called cases 1, 2, 3 and 4), were carried out in this section. Fluid transport in the system studied was a NEMD process. Applying a thermostat was difficult because the local streaming velocity for liquid molecules was not zero. In a rigorous sense, one should distinguish the streaming kinetic energy from the thermal kinetic energy in applying the thermostat. The problem is that the local streaming velocity is not available before performing simulation. The effect of the streaming kinetic energy on temperature was ignored due to the consideration of the streaming kinetic energy being a small fraction of the

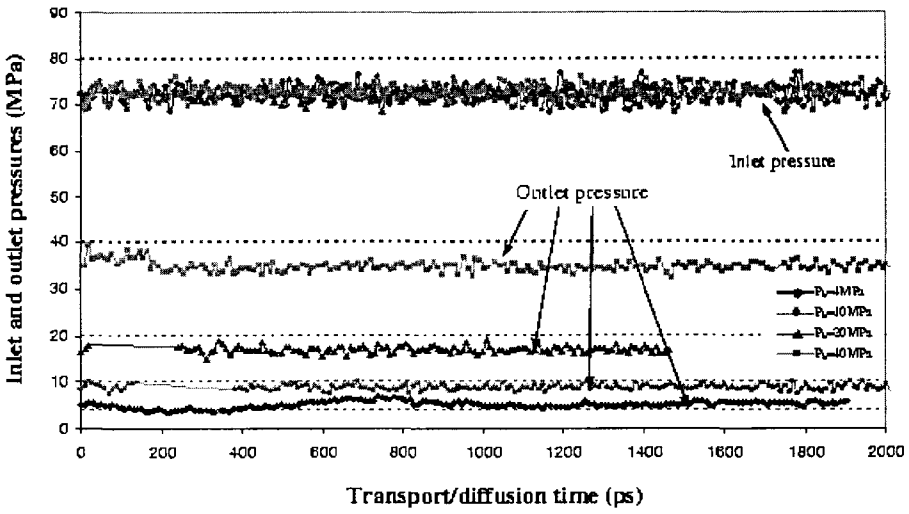

Figure 3.5: Pressures at inlet and outlet of the nanopore as a function of transport time under different back pressures. The dashed lines are the front and back pressures exerted on the front and back self-adjusting plates.

thermal kinetic energy in this study. For example, for a liquid molecule with a streaming velocity 40 m/s in nanopore (refer to Fig. 3.7), the associated streaming kinetic energy is less than 2% of the thermal kinetic energy. We checked the temperature evolution with respect to transport time, and found that time-averaged temperatures ($\triangle t = 10\ ps$) for four cases were the same and were kept constant during the transport process.

The Irving-Kirkwood method was applied to calculate the pressures in entrance and exit parts (called inlet and outlet pressures). The computational boxes for pressure calculation have the length 4 nm in the z-direction for both of them. In the kinetic part of Irving-Kirkwood equation (2.10), the peculiar velocity should be the molecular velocity minus the streaming velocity at the molecular position. But in this work, the streaming velocities in the entrance and exit parts ($< 5\ m/s$ for all cases studied) were much smaller than molecular

thermal velocities. Therefore, the influence of streaming velocity on pressure was small and ignored. Fig. 3.5 shows the inlet and outlet pressure distributions under different back pressures with respect to the transport time. The symbols •, ♦, ■ and ▲ in the figure correspond to the cases 1, 2, 3 and 4, respectively. One sees that the pressures averaged in a short period (e.g., $\triangle t = 10$ ps) fluctuate as the transport process continues. But the pressure stayed more or less constant over a larger time scale, indicating that the method proposed in this study works well and can be applied to perform a fluid transport through nanopores driven by pressure difference. The mean inlet pressure for all cases is about 72.5 MPa; the mean outlet pressures for cases 1, 2, 3 and 4 are 5.13, 8.8, 17.1 and 34.7 MPa, respectively. Comparing these values with those exerted on the adjusted plates, they are close but have some differences, i.e., pressures calculated at the inlet and outlet, except for the outlet pressure of case 1, are smaller than those applied at the front and back adjusted plates. One possible reason for this phenomenon is that molecules around the inlet and outlet, comparing with those far away from inlet and outlet in the reservoirs, possess higher kinetic energy. The outlet pressure of case 1 is slightly larger than the pressure applied on back self-adjusting plate, the physical origin is not clear, but it is worth pointing out that in this case, a phase change occurred at around the exit of the nanopore. Removing the separation plate from the middle of nanopore produced a small disturbance to the pressure field. The duration of this impact on the pressure fields depends on the pressure difference between the inlet and outlet. For the case with the lowest back pressure, the impact time was about 1 ns.

To obtain the density and streaming velocity (V_z) distributions along radial and axial directions, the whole system was divided into 9 axial sections (3

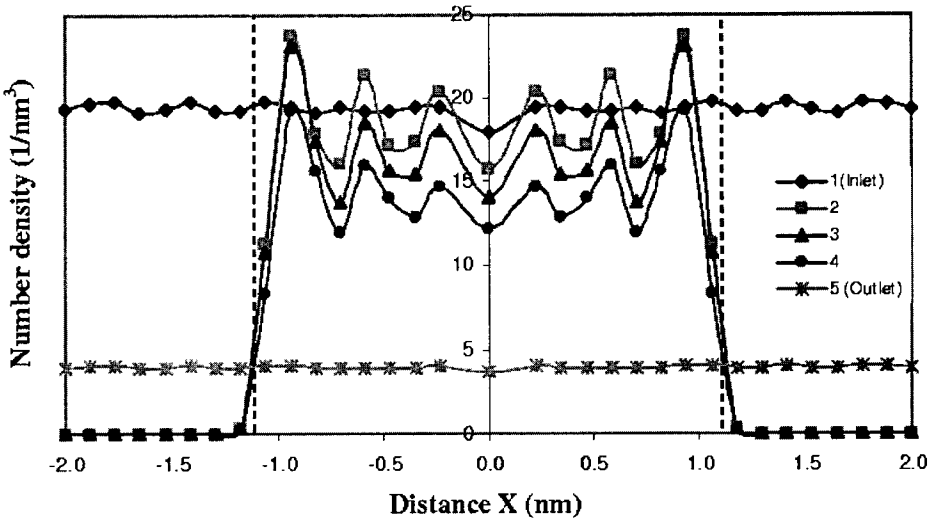

Figure 3.6: Number density distributions at entrance part, nanopore and exit part versus radius for the case with $P_b = 4MPa$. Dashed lines are the internal surface of nanopore.

sections in each of the front chamber, nanopore and back chamber) in axial direction, 32 sections in the radial direction (10 sections in nanopore). The results far away from the inlet and outlet of the nanopore, i.e., first and last two sections in the front and back chambers, were omitted for streaming velocity distributions in radial direction due to our interest in the nanopore and the immediate areas around it. To show the fluid transport in this system clearly, case 1 was taken as an example, and the results for the density and velocity distributions in the radial direction are shown in Figs. 3.6 and 3.7. The density and streaming velocity distributions along z-direction will be presented in the following section. Fig. 3.6 shows the density profiles at the entrance part, nanopore (sections 2, 3 and 4) and exit part. From this picture, one sees that the density profiles in the radial direction are uniform at the front and back of the nanopore, but of an oscillatory form in the nanopore due to the interaction between solid and

liquid. This oscillation distribution is similar to those obtained from Poiseuille and Couette flows in a confined channel [24, 25, 34–36, 38, 43, 46, 50, 51]. Moreover, the six-peak structure of density profile implies that there were three circular liquid layers formed in this small channel with a size of 6.5 molecules, and the densest distribution of liquid molecules located at the layer close to solid substrate. Fig. 3.7 shows the average velocity distributions at different sections. The shape of velocity profiles inside the nanopore are all characterized by having the maximum velocity in the center of the channel as expected, but there is a distinct inflection in the profile near the wall. It is also noted that the mean velocity in the nearest the wall has a non-zero velocity, but care should be taken in interpreting that as a non-slip condition because this velocity strongly depends on the interaction between solid/liquid. The maximum velocity in the nanopore in the flow direction monotonically increases due to the changing density. The velocity profile before the inlet and after the outlet are remarkable similar in shape and show evidence of a fluid jet emerging from the pore. From the density and velocity distributions shown in Figs. 3.6 and 3.7, the number flow rate at different sections in the nanopore were calculated. The results for sections 2, 3 and 4 in the nanopore were 944, 944 and 952 molecules per nano second, respectively. The difference among them was about one percent, which means that a steady flow condition had been reached. To check the consistency of velocity profiles at different cross sections in the nanopore, we normalized them using values at $x = 0$, and results were plotted in the inset of Fig. 3.7. One sees that the normalized profiles of velocity at different cross sections are almost same.

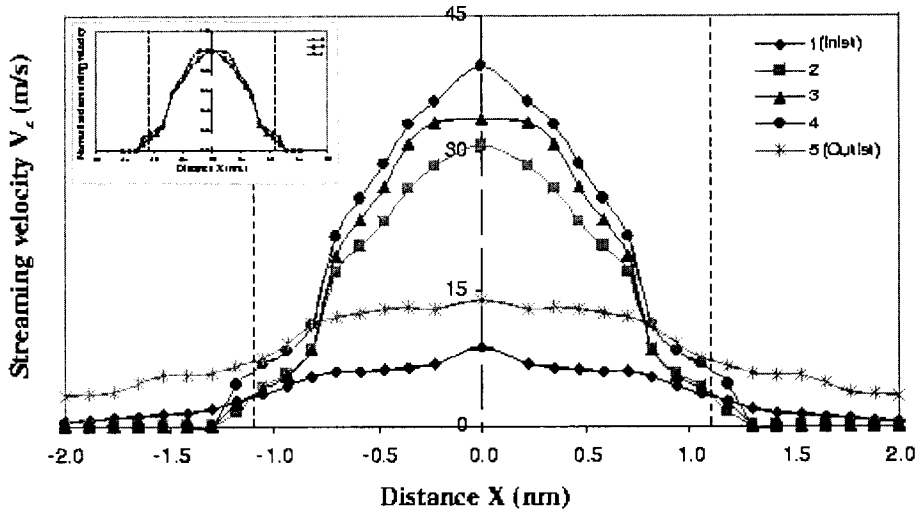

Figure 3.7: Streaming velocity distributions at entrance part, nanopore and exit part versus the radius for the case with $P_b = 4MPa$. Numbers 1 and 5 represent entrance and exit parts; Numbers 2-4 depict sections in the nanopore. The inset in the figure is normalized streaming velocity distributions corresponding to sections 2-4 of this case. Dashed lines are the internal surface of nanopore.

3.3.2 Effect of Back Pressure

In this part, we focus on the study of the effect of back pressure on liquid transport through the nanopore. Figs. 3.8 and 3.9 show the time-averaged density and velocity (V_z) distributions with respect to axial distance z under different back pressures (note: lines are drawn to guide the eyes for the trend of the data). The meanings of symbols are the same as those used in Fig. 3.5. Fig. 3.8 shows density distributions in z-direction having the same pattern for different cases, i.e., density has a near constant distribution in the front reservoir. But when molecules enter the nanopore, density decreases. When molecules reach the vicinity of the outlet, it quickly drops to a level that is close to that of the back reservoir. For the case with lowest back pressures, $P_b = 4MPa$,

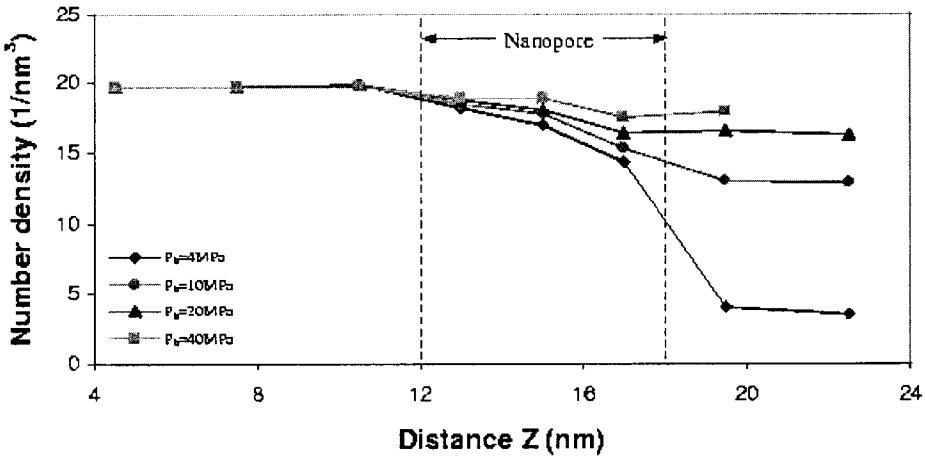

Figure 3.8: Variation of number density distribution as function of distance z under different back pressures (lines are drawn to guide the eyes for the trend of the data).

the significant drop of density at the outlet of the channel implies that a phase change occurs at the outlet of the nanopore. Moreover, this picture gives other information: first, the back pressure has little influence on the density distribution in the front reservoir; second, the decrement of density in the nanopore depends on the back pressure. Fig. 3.9 represents the streaming velocities (V_z) for different cases as a function of distance z. The streaming velocity at the front of the nanopore maintains constant, which is consistent with the density distribution in Fig. 3.8. When molecules approach the inlet and enter the nanopore, they accelerate and the streaming velocity increases dramatically due to the contraction of pass-through area and constant flow rate condition. Once in the nanopore, the streaming velocity changes were mild and depended on the the back pressure. In the back reservoir, the streaming velocity decreases due mainly to the area change.

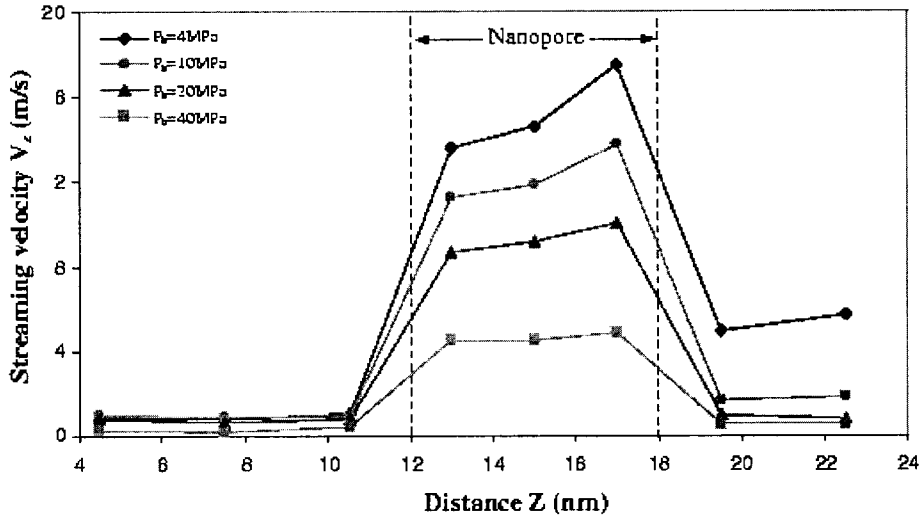

Figure 3.9: Variation of streaming velocity distribution as function of distance z under different back pressures (lines are drawn to guide the eyes for the trend of the data).

To show the effect of back pressure on liquid transport in the nanopore clearly, the value averaged in whole length nanopore was chosen as the characteristic velocity for that radial position. Figs. 3.10 and 3.11 show the density and streaming velocity distributions with respect to radial distance, respectively. For all cases, one sees that the back pressure has no significant influence on distribution patterns, i.e., the density has an oscillatory distribution and the streaming velocity has a quasi-parabolic distribution in the radial direction, but the back pressure impacts the values of density and streaming velocity, i.e., low back pressure corresponding to low density distribution but high streaming velocity in the channel. The inset in Fig. 3.11 gives the normalized velocity distributions of four cases. One sees that they are almost identical. Fig. 3.11 indicates that the magnitude of the streaming velocity is dependent but the

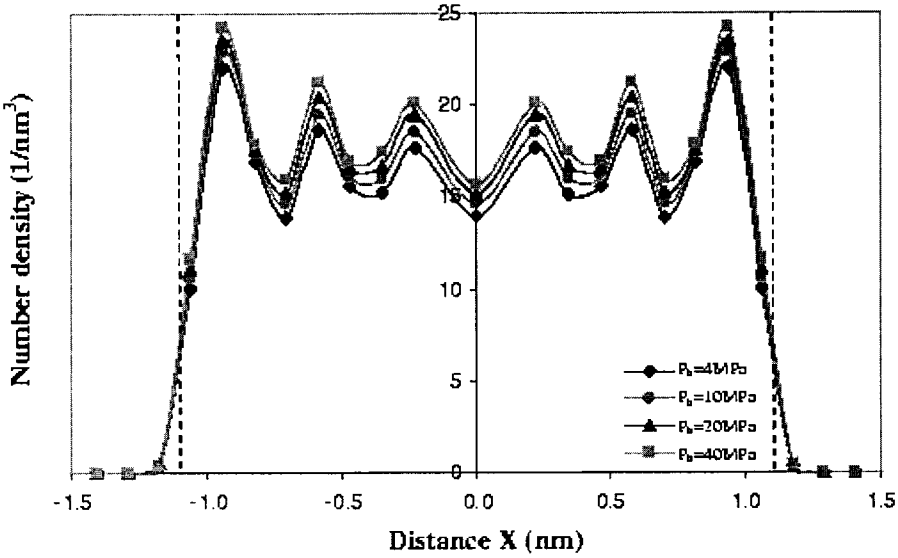

Figure 3.10: Effect of back pressure on number density distribution in nanopore. Dashed lines are the internal surface of nanopore.

profile of velocity distribution is independent on the pressure drop across the membrane.

Fig. 3.12 shows the number flow rate through a single nanopore in the membrane as a function of pressure drop across the membrane. In this picture, the horizontal axis represents the pressure difference between inlet and outlet of the nanopore with the unit MPa; the vertical axis shows the ability of liquid molecules passing through a single nanopore per nano second. From the slopes calculated using two adjacent data points (16.8, 21.6 and 33.4), one sees that the number flow rate with pressure drop deviates from the linear relationship, which would be expected for a macroscopic incompressible flow. Actually, the flow rate shown in Fig. 3.12 are contributed by four parts, convection part caused by pressure difference (under constant density and viscosity condition), diffusion part caused by density gradient (under constant pressure and viscosity), part

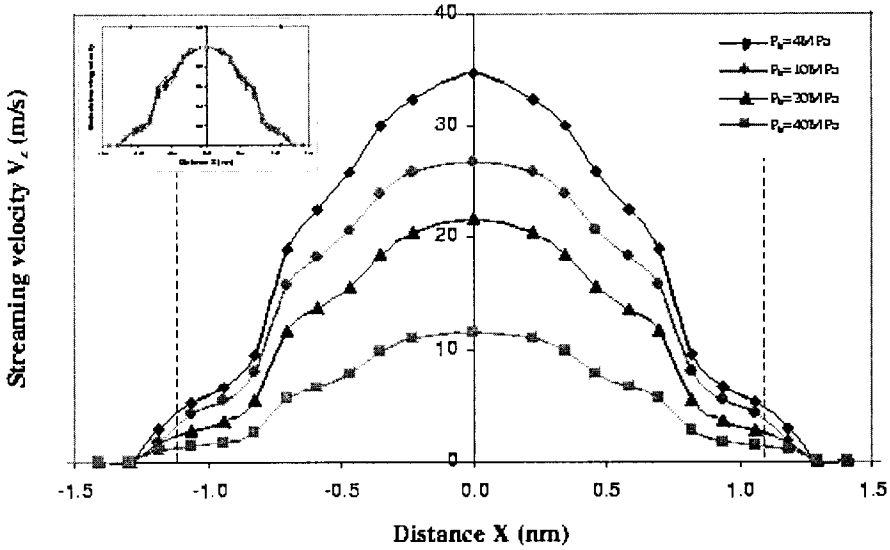

Figure 3.11: Effect of back pressure on streaming velocity in nanopore. The inset is the comparison of streaming velocity profiles normalized by using velocities at $x = 0$. Dashed lines are the internal surface of nanopore.

caused by viscosity change along the channel and part caused due to the phase change at the exit of the channel at low back pressures. Because of these complications, we cannot separate these parts and judge how much contribution of each part to the total flow rate. But the larger pressure and density gradients, and smaller viscosity and phase change obviously enhance the fluid transport through a channel. Hence, the flow rate with respect to pressure drop deviates from the linear relationship and the slop increases as the pressure drop increases.

In the above section, the liquid transport in the nanopore was discussed in detail. But in practice, sometimes researchers are only interested in the ability of a membrane to transport liquid, i.e., the relationship of liquid flux with driven force (pressure or density difference). In this case, Fick's Law and Darcy's Law can be used to predict the diffusivity and permeability according to the density

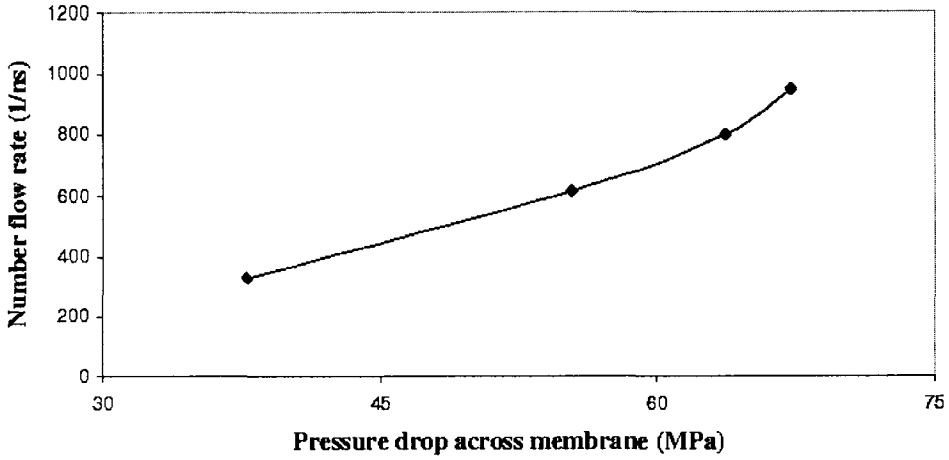

Figure 3.12: Variation of the number flow rate as a function of the pressure drop across the membrane.

or pressure difference between front and back reservoirs and flow rate shown in Fig. 3.12. In Chapter 6, results will be compared with those predicted by Navier-Stokes equations with the effect of wall on the flow.

A potential use of this method is to deal with water or solvent with ions transport through a membrane. In this case, the force acting on the self-adjusting plates can be handled in the same manner that was used in the present work if the self-adjusting plates are formed by non-polar molecules. For the effect of long-range Coulombic interactions in the bulk liquid (ions in front and back semi-infinite spaces) or in images in periodic directions, it can be calculated by using two integral functions approximately or a two-dimensional particle mesh Ewald summation [132].

3.4 Summary

Fluid transport through a nanopore in a membrane was studied by a novel molecular dynamics approach proposed in this study. The advantages of this method, relative to the DCV-GCMD method, are that it eliminates disruptions to the system dynamics that are normally created by inserting or deleting particles from control volumes, and that it functions well for dense systems due to the number of particles in the studied system fixed. NEMD results obtained by this method also show that pressure and density distributions are uniform in the front and back reservoirs, but wavelike in the direction normal to solid wall in nanopore. Streaming velocity in the nanopore has a quasi-parabolic profile with respect to radial distance and is independent of the pressure drop across the membrane.

Chapter 4

Study of Solid Wall-Liquid Interaction on Pressure-Driven Liquid Transport through a Finite Cylindrical Nanopore Using an Improved Non-Equilibrium Molecular Dynamics Method

4.1 MD Simulation and Methodology

The system of interest in this chapter is same as that described in Chapter 3, i.e., a cylindrical nanopore with a finite thickness whose two ends connect to two semi-infinite reservoirs in which the pressures were maintained at fixed, but different, levels to induce flow through the nanopore. In Chapter 3, the method proposed in this thesis was examined by using a variable back pressure. In this chapter, the effect of solid wall-liquid interaction on liquid transport through a finite length nanopore driven by a constant pressure drop over the channel was investigated. Three cases with different energy scales for the solid substrate, i.e., case 1 $\varepsilon_s = 0.1\varepsilon_l$ (weak or hydrophobic-like), case 2 $\varepsilon_s = \varepsilon_l$ (neutral) and case 3 $\varepsilon_s = 10\varepsilon_l$ (strong or hydrophilic-like), were studied. Here, ε_l is the

liquid energy scale. For all simulations performed, periodic boundary conditions were exerted in the x and y-directions, but not the z-direction. Therefore, the system can be thought of as the building unit of a membrane in which an array of nanopores are arranged regularly. Two reservoirs become semi-infinite, which allows the use far field boundary conditions, i.e., 1-D uniform velocity and pressure, at locations far away from the inlet and outlet of the nanopore. In Chapter 3, far field boundary conditions by using two self-adjusting plates were addressed in detail. In the older version, the self-adjusting plates were two rigid plates. In order to reduce the effect of rigid plates on the motion of the molecules near them, the two rigid self-adjusting plates were changed into two self-adjusting frames in which molecules can move freely in x and y directions but can not escape from the frames in the z direction. The molecules in each frame have the uniform velocity component in the z direction. This modification allows molecules in these self-adjusting frames to have quasi three dimensional properties. To follow the nomenclature of the previous chapter, the far field boundary conditions modeled by two self-adjusting frames in this chapter are still referred to self-adjusting plates. For details on this method and parameter selections, please refer to the previous chapter or reference [62].

To examine the effect of the solid wall-liquid interaction on liquid transport in the finite length nanopore, the parameters, except for the energy scale of solid substrate, were fixed in this chapter. The pressure difference between two reservoirs in the NEMD simulations in this chapter was fixed to be 40 MPa (80 MPa in the front reservoir and 40 MPa in the back reservoir). The governing equations and the procedures are same as those used in the previous chapter and omitted in this chapter.

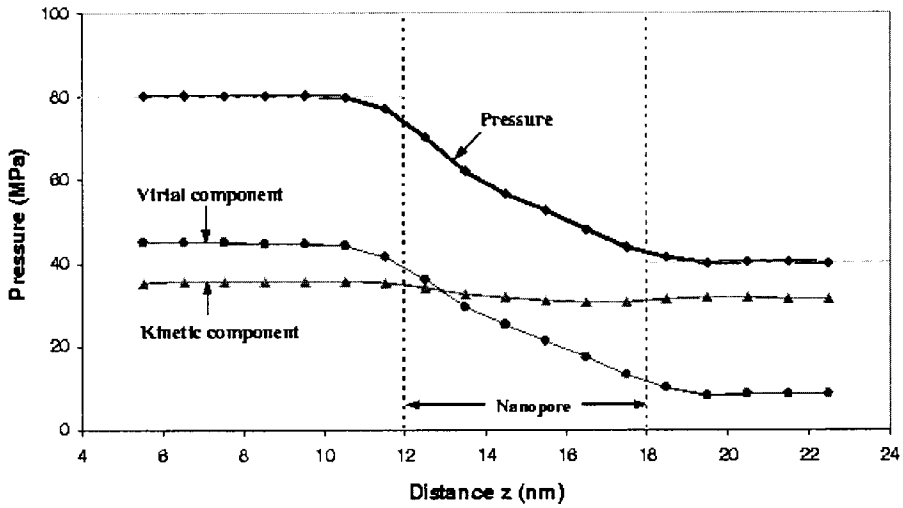

Figure 4.1: Pressure and its components (kinetic and virial parts) distributions of the case 1 ($\varepsilon_s = 0.1\varepsilon_l$) averaged over the whole cross-section as a function of axial distance z.

4.2 Results and Discussion

As mentioned, three different energy scales for the wall molecules were applied to examine the effect of the solid wall on liquid transport in the nanopore subjected to a constant pressure difference across the nanopore. In all simulations, temperature was controlled to be $Tk_b/\varepsilon_l = 1.1$. The temperature variation in the axial direction averaged over a period 50 ps was checked, and found that temperature remains nearly constant except for a small perturbation ($\pm 5K$) around the inlet and outlet of the nanopore. But this perturbation disappeared and a constant temperature in the whole system was observed when the data was averaged over a large period of the time (e.g. 500 ps).

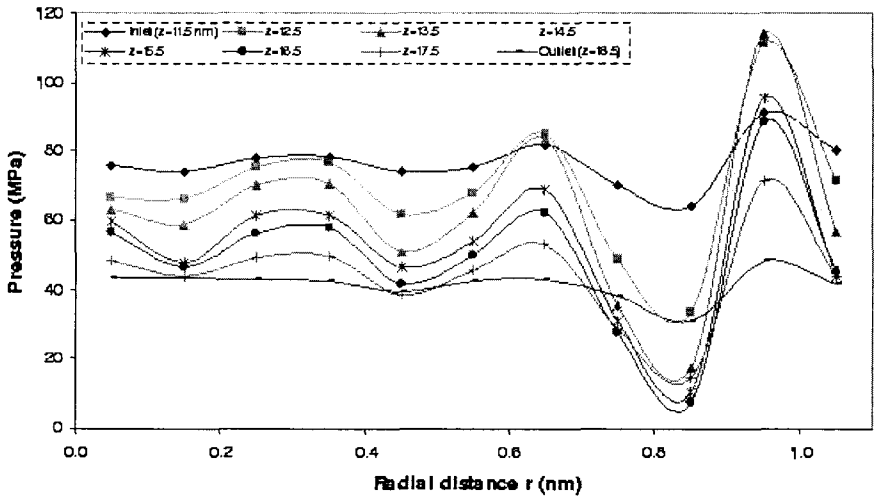

Figure 4.2: Pressure distribution of case 1 ($\varepsilon_s = 0.1\varepsilon_l$) with respect to the radial distance at the inlet, nanopore and outlet.

4.2.1 Pressure Distribution

The objective of the method used in this study is to produce constant pressure fields with different levels in the front and back reservoirs to induce liquid transport through the nanopore. Pressures in the nanopore and two reservoirs were calculated by the Irving-Kirkwood equation. The computational box for pressure calculation is a moving window that has a width of 2 nm in the z-direction, 7 nm in x and y-directions in reservoirs, 0.1 nm in radial direction in the nanopore. To show the pressure distributions in the axial and radial directions in detail, case 1 ($\varepsilon_s = 0.1\varepsilon_l$) was chosen as an example and the results are shown in Figs. 4.1 and 4.2. Fig. 4.1 shows the pressure distribution, averaged over the corresponding cross-sections, in the z direction. In this figure, the short vertical dashed lines signify the entrance and exit of the nanopore; the long horizontal dashed lines denote the pressures externally exerted on the

front and back self-adjusting plates. The lines with the symbols of ▲, • and ♦ represent the kinetic component, virial component and total pressure, respectively. The kinetic component varies slightly in the z direction due to the fact that temperature was constant throughout system and the density change in the z-direction is small. But the virial component in the nanopore changes significantly in the flow direction and dominates the variation of the total pressure. Two points are noteworthy. First, the calculated pressures in the front and back reservoirs are constant and equal to the pressures exerted on the front and back self-adjusting plates. Here, we demonstrate, for the first time, using the Irving-Kirkwood equation to capture this characteristic that is physically observed in macroscopic system (e.g., liquid pressure in a cylinder is equal to the pressure externally exerted on a piston if the effect of liquid density and the weight of piston are negligible). Secondly, the pressure averaged in the each cross-section in this small nanopore decreases monotonically, just like a pressure distribution of a pressure-driven flow in a macroscopic channel, for this case with weak solid wall-liquid interaction. Fig. 4.2 shows the pressure distributions in the radial direction at locations 0.5 nm away from the inlet and outlet and in the nanopore. Pressure distributions at both inlet and outlet have a small change when $r \leq 0.75$ nm, especially for the pressure at the outlet. But variation of pressure distributions intensifies strong when $r > 0.75$ nm. Pressure distribution in the nanopore shows a wavelike pattern, and the amplitude of the wave increases when the radial distance approaches the solid substrate. The reason for this distribution is mainly due to the layered distribution of the liquid molecules and the interaction between the solid and liquid.

The effect of solid wall-liquid interaction on liquid pressure distribution in the z direction is shown in Fig. 4.3. In the nanopore, pressure for cases 1

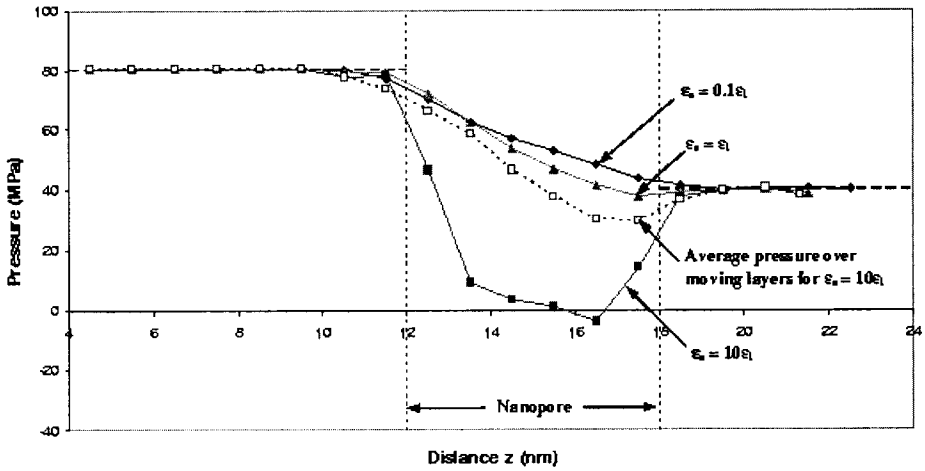

Figure 4.3: Comparison of pressure distributions, averaged over whole cross-section, under different solid wall-liquid interactions. The dashed line with symbol $\diamond$ is the pressure distribution of case 3 ($\varepsilon_s = 10\varepsilon_l$) averaged over moving layers (r $\leq$ 0.75 nm) in the nanopore and the vicinities around the inlet and outlet.

and 2 ($\varepsilon_s \leq \varepsilon_l$) decreases monotonically although pressures between them differ slightly. However, the pressure distribution for case 3 ($\varepsilon_s > \varepsilon_l$) shows a different pattern. In particular, pressure near the entrance and exit of the nanopore drops abruptly to almost zero pressure. To discern the molecular mechanism that is responsible for the observation, the pressure distribution against the radial distance was plotted in Fig. 4.4. Comparing it with Fig. 4.2, pressure distributions for both of them in the region of $r \leq 0.75$ nm exhibit a similar pattern, except for the amplitude of the fluctuation. But the portions of the curves in the region where $r > 0.75$ nm differ considerably. One sees that pressure in the region close to the solid wall changes from a positive peak in Fig. 4.2 (case 1 with $\varepsilon_s < \varepsilon_l$) to a negative valley in Fig. 4.4 (case 3 with $\varepsilon_s > \varepsilon_l$). This is because solid molecules with large energy scale produce large attractive

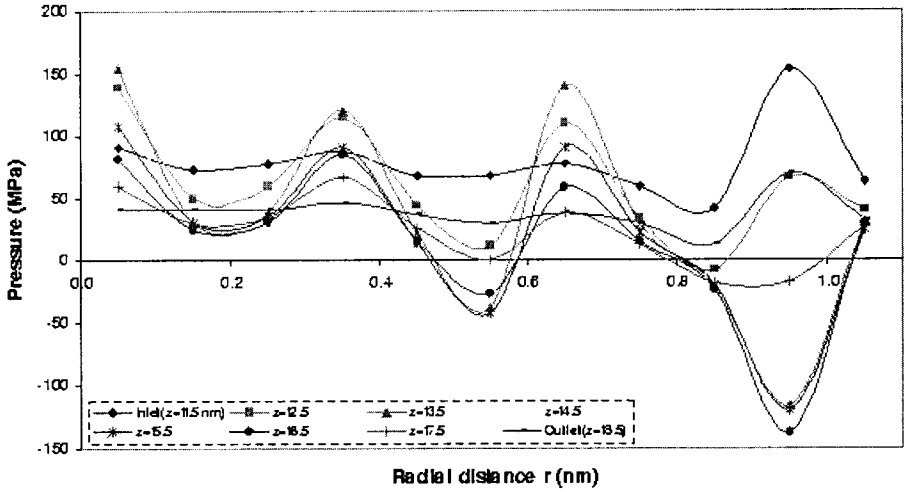

Figure 4.4: Pressure distribution of case 3 ($\varepsilon_s = 10\varepsilon_l$) with respect to the radial distance at the inlet, nanopore and outlet.

forces to the liquid molecules, resulting in a negative pressure. Actually, the first layer of the liquid molecules near the solid substrate does not move (see Fig. 4.7). As a result, the effective pass-through area for case 3 is smaller than that of the other two cases. The average pressure on this effective pass-through area was calculated and presented in Fig. 4.3 by a dashed line with the symbol $\diamond$. It can be seen that pressure associated with the region of moving molecules decreases monotonically in most part of the nanopore.

The pressure fields in the upstream and downstream reservoirs for three cases with different solid wall-liquid interactions, shown in Fig. 4.3, were identical and maintained constant, which means that the method used in this thesis works well and is robust. The potential use of this method is to study multi-component flows in such a system, e.g., diluted DNA or polymer molecules suspending in a solvent being transported through a nanopore in a membrane induced by a pressure gradient or by a combination of electric field and pressure field.

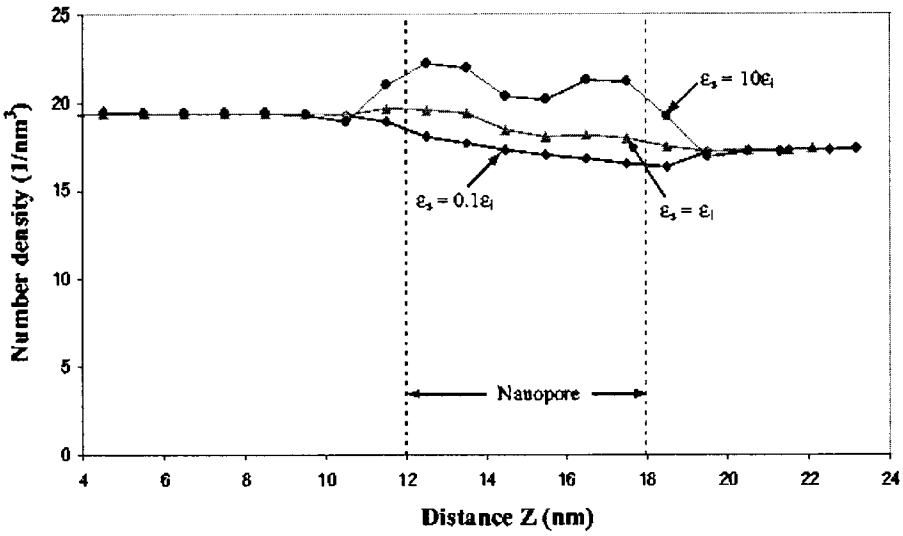

Figure 4.5: Comparison of number density distributions with radial distance under different solid-liquid interactions. Dashed lines are the internal surface of the nanopore.

4.2.2 Density Distribution

Effect of solid wall-liquid interaction on the density distribution is shown in Figs. 4.5 and 4.6. In these figures, the lines with symbols of ♦, ▲ and ■ express the density distributions for cases 1, 2 and 3, respectively. Fig. 4.5 shows the average number density versus the distance z. From this figure, one sees that densities in the reservoirs distribute uniformly in the z direction, but the values in two reservoirs were slightly different due to the pressures in two reservoirs different. Density for the solid wall-liquid with the neutral-like or hydrophobic-like interaction decreased monotonically in the channel. While density had two peaks located at the entrance and exit of the nanopore for the solid wall-liquid had a hydrophilic-like interaction. The behavior for proposed reason is because the molecules in the front and back surfaces of the membrane

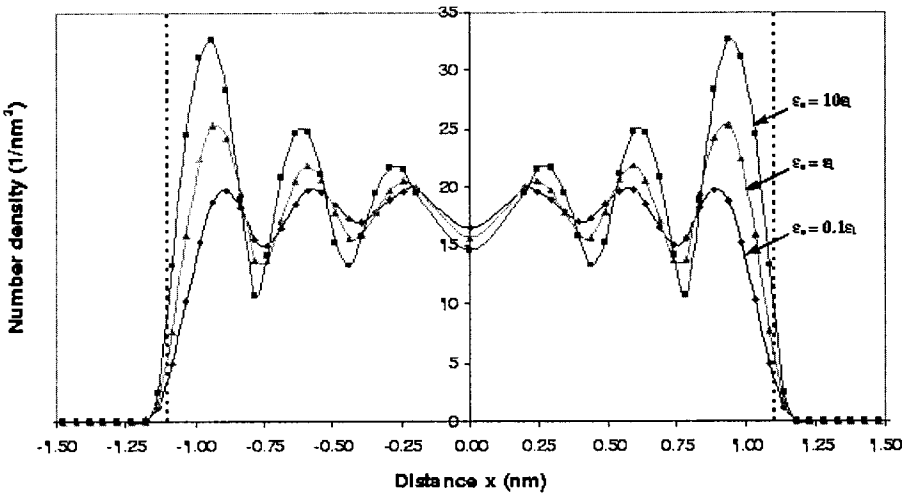

Figure 4.6: Comparison of number density distributions with radial distance under different solid-liquid interactions. Dashed lines are the internal surface of the nanopore.

have more attractive forces to the liquid molecules, which induce more liquid molecules accommodating at the around entrance and exit. Fig. 4.6 shows the variation of the number density distribution with respect to the radial distance r. It is observed from this figure that liquid density in a small confined channel distributes in an oscillatory pattern normal to the wall direction regardless the strength of solid-liquid interaction. This observation implies that the confined geometry is the major factor which impacts the fluid density distribution in a small confined channel. And the oscillatory amplitude depends on the strength of solid-liquid interaction. In particular, the stronger the interaction, the larger the amplitude. The density in each liquid layer is a function of its radial position. The liquid layer located closer to the solid substrate accommodates more liquid molecules if ε_s is larger than a certain value, for example, $\varepsilon_s \geq \varepsilon_l$ in this study.

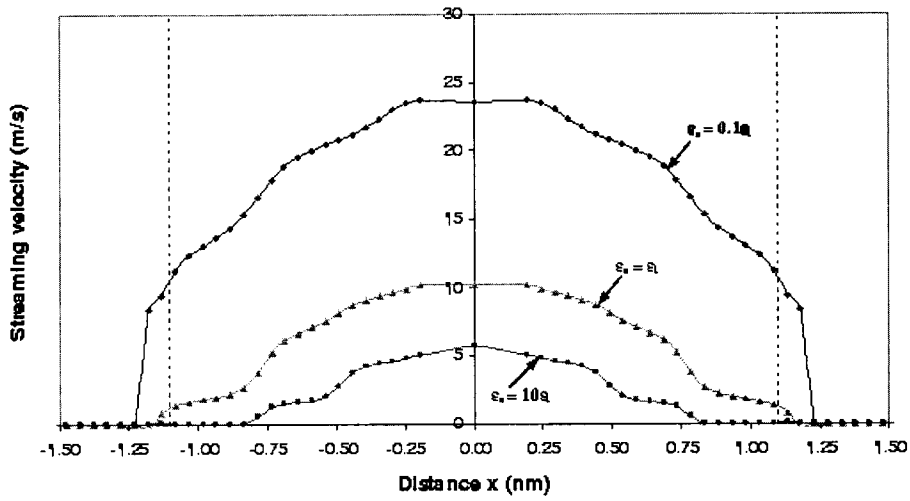

Figure 4.7: Comparison of streaming velocity distributions versus radial distance under different solid-liquid interactions. Dashed lines are the internal surface of the nanopore.

4.2.3 Streaming Velocity Distribution

Fig. 4.7 shows the effect of the solid-liquid interaction on the streaming velocity distribution in the nanopore (averaged over the whole length of the nanopore). It is obvious that the velocity profile strongly depends on the solid-liquid interaction. We see that the streaming velocity on the solid boundary changes from slip to stick as the solid-liquid interaction varies from weak to strong interaction. Fig. 4.8 presents the streaming velocity distribution (averaged over the whole cross-section) with respect to the axial distance z. One sees that the streaming velocity for each case has an uniform velocity in the front reservoir. When molecules approach and enter the nanopore, they accelerate and streaming velocity increases dramatically due to contraction of pass-through area. In the nanopore, the streaming velocity increases slightly because of small change of density in the system studied. When molecules leave the nanopore and enter

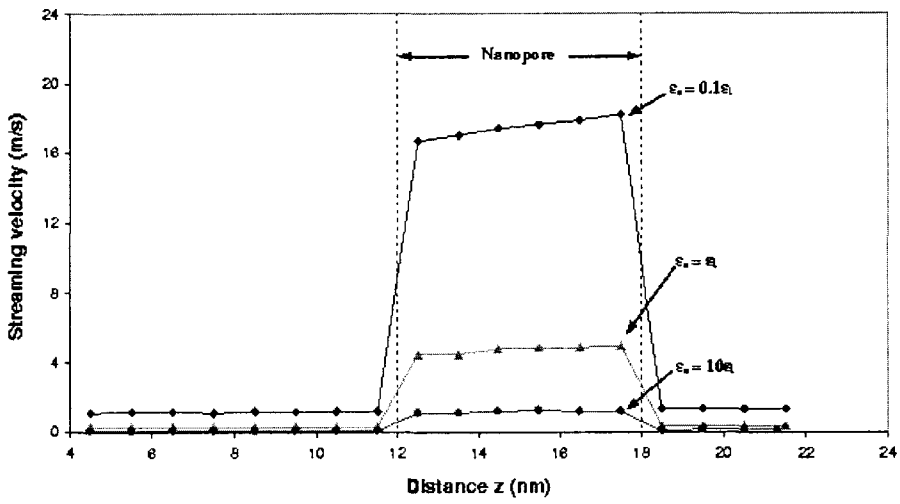

Figure 4.8: Comparison of streaming velocity distributions versus axial distance under different solid-liquid interactions. Dashed lines are the internal surface of the nanopore.

into the back reservoir, the streaming velocity drops to a low level due to the pass-through area change.

4.2.4 Flux Distribution and Flow Rate

For an incompressible flow in a macroscopic system, the flux profile is similar to the velocity profile due to the fact that density is constant. Therefore, the transport ability of a channel can be obtained by integrating the velocity distribution in a cross section and then multiplied the result by the fluid density. But in a confined small system, the density distribution in the radial direction is not uniform. As a result, the flux profile would differ from the velocity profile as the integration is performed on the product of the local density and velocity. Fig. 4.9 shows the radial distribuions of flux distributions for all three cases. This figure clearly demonstrates the mass flow ability in different layers. One sees that

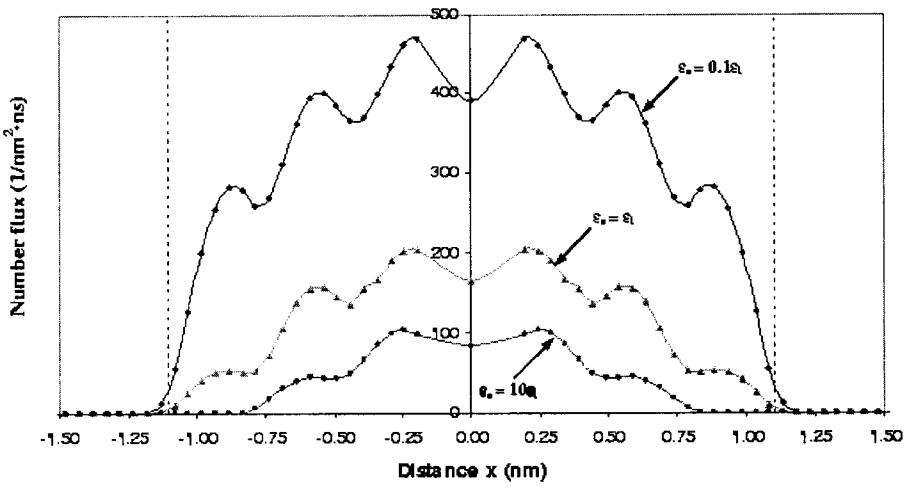

Figure 4.9: Comparison of flux distributions versus radial distance under different solid-liquid interactions. Dashed lines are the internal surface of the nanopore.

the flux is a function of the radial distance. The liquid layer closer to the center of the pore carries more liquid molecules per unit area through the nanopore, though the maximum flux does not occur at the center line. Moreover, the flux for moving liquid part in the channel has a quasi-parabolic distribution.

The flow rates for cases 1, 2 and 3 are 1081.2, 334.2 and 96.9 $1/ns$, respectively. Observing these values, one sees that the flow rate of the case 1 is about 3.24 times of the case 2; the flow rate of the case 3 is about 0.29 time of the case 2. Comparing these flow rate ratios to the corresponding $\varepsilon_l/\varepsilon_{sl}$ values (e.g., 3.16 for case 1 and 0.316 for case 3), it seems that the flow rate has an nearly inverse relationship with the solid-liquid interaction as clearly shown by Fig. 4.10. The fact that the flow rate depends on the solid-liquid interaction also implies that the classical continuum theory based on Navier-Stokes equations and no-slip boundary conditions breaks down in the current system. This breakdown is

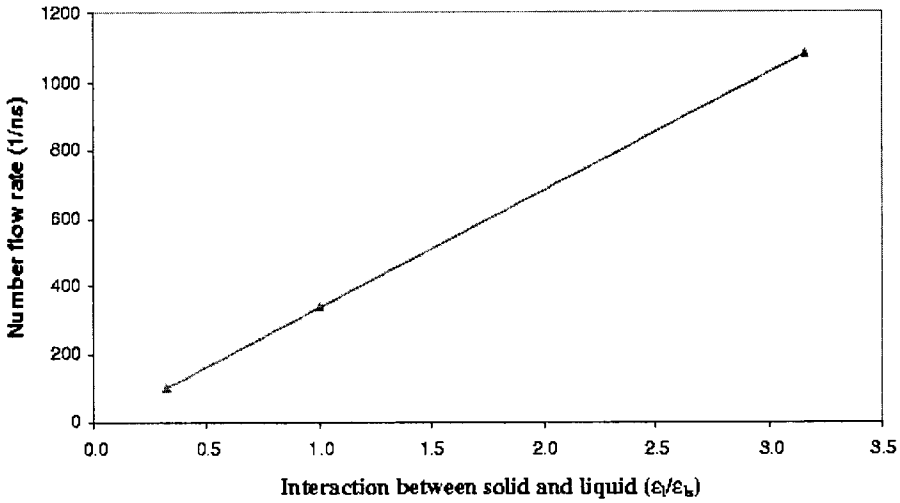

Figure 4.10: Effect of solid-liquid interaction on number flow rate.

because the flow rate predicted by the classical continuum theory should not change if the pressure drop across the channel is constant. The comparisons between NEMD simulations and classical continuum theory for this system will be addressed in Chapter 6.

4.3 Summary

The effect of solid wall-liquid interaction on the liquid transport in a finite cylindrical nanopore subjected to a constant pressure drop across the channel was investigated by an improved non-equilibrium molecular dynamics method. The NEMD results in this microscopic system demonstrate a characteristic that is physically observed in macroscopic systems as well, i.e., liquid pressure in a cylinder is equal to the pressure externally exerted on a piston if the effect of liquid density and the weight of piston are negligible. The solid wall-liquid

interaction shows a significant effect on the liquid transport in a nanopore. In particular, the weak solid-liquid interaction causes liquid slipping on the solid wall, while strong interaction promotes sticking at the wall. The flow rate calculated by NEMD simulations, subjected to a constant pressure drop across the channel, depends on the solid wall-liquid interaction and is proportional to the ratio of $\varepsilon_l/\varepsilon_{ls}$ for the system studied.

Chapter 5

Investigation of Effect of Entrance and Exit on Liquid Transport through a Cylindrical Nanopore

5.1 Molecular Dynamics Simulation and Methodology

To compare the difference between fluid transport through finite and infinite length channels, two different systems were studied in this chapter. The first one is a finite length cylindrical nanopore which was studied in Chapters 3 and 4. The second system is a cylinder with a periodic boundary condition in its axial direction. Fig. 5.1 is a snapshot of two different systems studied in this chapter. The (a), (b) and (c) in Fig. 5.1 show the geometries studied in the finite length system, infinite length system (implemented by periodical boundary condition in its axial direction) and the cross-section of the channel for both systems. The formation and geometry of the cylinder used in the second system is same as that used in the first system. Instead of the pressure gradient used in the first system, an external gravity-like force in the second system was applied to drive molecules moving in the channel. To make the results of two systems comparable, the molecules inside the channel in two systems and the

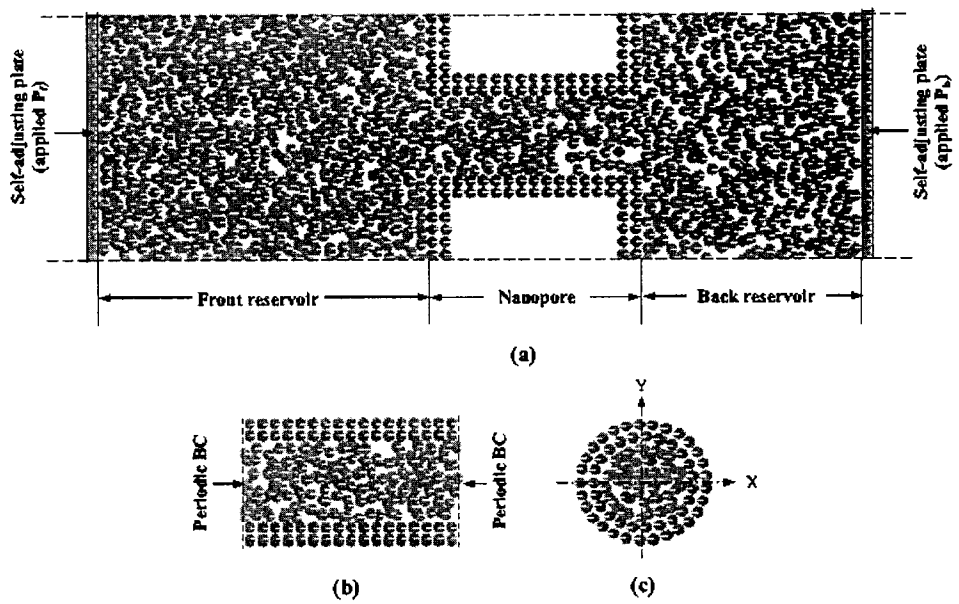

Figure 5.1: (a) Snapshot of a finite length nanopore in a membrane, (b) snapshot of nanopare with periodical boundary condition in its axial direction and (c) cross-section of the nanopore.

total external forces exerted on two systems should be set to be the same, i.e.,

$$N_{in}^1 = N_{in}^2 \tag{5.1}$$

$$\Delta P \cdot A = a_{ext} m N_{in}^2 \tag{5.2}$$

where N_{in}^1 and N_{in}^2 express the numbers of molecules inside the channel in the first and second systems, respectively; ΔP is the pressure drop over the channel in the first system; A is the inside cross-section area of the channel; a_{ext} is the external gravity exerted on each liquid molecule in the second system and m is the mass of liquid molecule.

The method for establishing initial conditions in the second system is that

the liquid molecules were packed in the channel. The initial velocities that had a Maxwellian distribution (corresponding to the liquid with an average temperature of $T = 133\ K$) were assigned on the molecules. Then molecules in the channel were released to move without the external force until the equilibrium state was reached. After that, a constant external force, $a_{ext}m$, was exerted on each liquid molecule until a steady state flow was met. During this period, two Berendsen thermostats were coupled to liquid molecules and wall molecules separately to maintain the system temperature constant.

The calculations of liquid transport in the second system is similar to those used in the previous chapters. The only difference between the two systems is that the motion of liquid molecules inside the channel in the first system is only governed by the intermolecular force, while the motion of liquid molecules in the second system is dominated by both intermolecular force and external force.

5.2 Comparison of Liquid Transports through a Finite and an Infinite Length Nanopore

In each system, two cases with different solid wall-liquid interactions, i.e., one with a weak or hydrophobic-like ($\varepsilon_s = 0.1\varepsilon_l$) and the other with a neutral-like ($\varepsilon_s = \varepsilon_l$) solid wall-liquid interaction, were carried out. For liquid transport through the finite length nanopore, fluid properties (e,g., pressure, density, velocity, etc.) vary not only in the radial direction, but also in the stream-wise direction due to the effect of the entrance and exit. While for fluid transport through an infinite length channel, fluid properties only change with respect to the radial distance. To make the calculation results of the two systems comparable, the liquid properties (e.g., pressure, density and velocity) averaged over the channel were taken as the characteristic values in the following section.

For liquid motion in an infinite length nanopore (i.e., a nanopore with periodic boundary condition in the stream-wise direction), an implementable approach at present is the external-field driven method. In this approach, a constant, gravitational-like force is exerted on all of liquid molecules to induce the liquid motion in the channel. As mentioned in the previous section, the number of molecules in the channel and the total external force exerted on those molecules in the two systems should be set to be same in order to make the results in two systems comparable. Under these conditions, the parameters (e.g., density, pressure and streaming velocity) calculated from the second system are equivalent to the values averaged over the channel in the first system approximately. The simulation results obtained from the first system showed that the numbers of molecules in the nanopore were 376 when $\varepsilon_s = 0.1\varepsilon_l$ and 423 when $\varepsilon_s = \varepsilon_l$. According to equation 5.2, the external force exerted on each liquid molecule in the second system should be $6.24 \times 10^{12}m$ (where m is the mass of liquid molecule) when $\varepsilon_s = 0.1\varepsilon_l$ and $5.42 \times 10^{12}m$ when $\varepsilon_s = \varepsilon_l$. In this chapter, three major parameters (i.e., pressure, density and streaming velocity) obtained from two different systems were compared to isolate the impact of the entrance and exit on liquid transport through a nanochannel.

Fig. 5.2 shows the comparison of pressure distributions versus the radial distance obtained under two different solid wall-liquid interactions in the two different systems. In the figure, two solid lines represent the pressure-driven NEMD results obtained in the finite length system; two dash lines with symbols show the results calculated in the infinite length channel and the error bars are the standard deviation. Comparing these distributions obtained in the two different systems, one sees that all results exhibit similar characteristics, i.e., the pressure distributes in the radial direction in an oscillatory pattern. For each

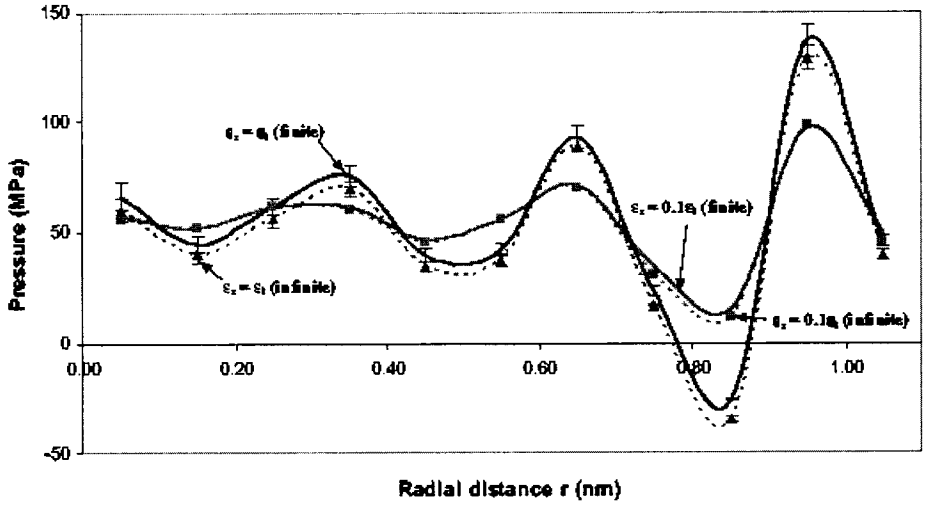

Figure 5.2: Comparison of pressure distributions (averaged over the channel) versus the radial distance under two different solid wall-liquid interactions in two different systems. Two solid lines are the results obtained in the finite length channel; the dash lines with symbols are results calculated in the infinite length channel and error bars are the standard deviation.

system, the amplitude of the fluctuation depends on the interaction between solid and liquid. The stronger the solid wall-liquid interaction, the larger amplitude of the pressure wave. To determine the consistence between two systems under the same solid-liquid interaction, the standard deviations were calculated. In the cases of hydrophobic-like interaction, the standard deviations for both systems are small and are in the size similar to that of the symbols. In the cases of neutral-like interaction, the largest standard deviations for two systems occurred at the first peak next to the solid wall, which were 7.33 MPa for the finite length system and 5.56 MPa for the infinite length system. One sees that the pressure difference between two systems were within the uncertainties.

To obtain the density and streaming velocity distributions along the radial

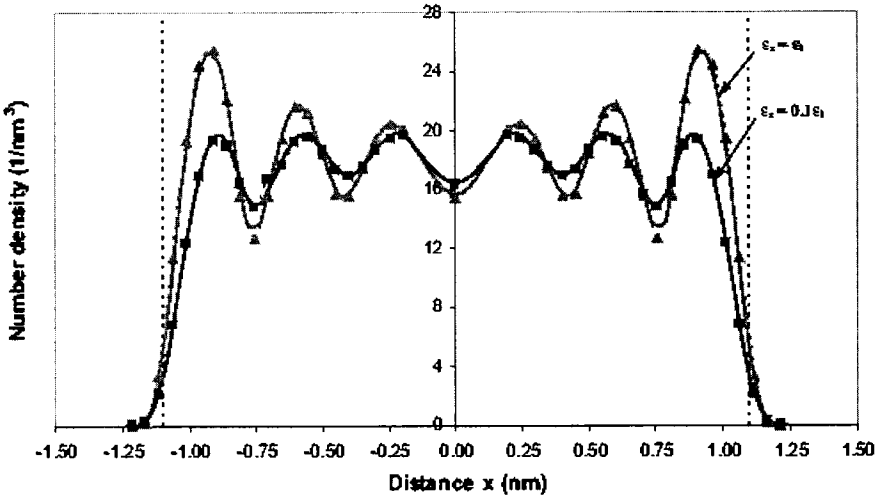

Figure 5.3: Comparison of number density distributions (averaged over the channel) with radial distance under different solid wall-liquid interactions in two different systems. Two solid lines are the results obtained in the finite length channel; the dash lines with symbols are results calculated in the infinite length channel. The vertical dash lines are the internal surface of the nanopore.

direction in the nanopore, the region ($r \leq 1.5\ nm$) was divided into 30 sections in the radial direction. To quickly obtain statistic values in a small system with limited molecules passing through the nanopore during a short period of time, equations 2.13 and 2.14 were applied. Fig. 5.3 exhibits the density distributions in the radial direction under two different solid wall-liquid interactions in two different systems. The meanings of the lines and symbols in this figure are same as those used in Fig. 5.2. It is noted that the density distributions in the radial direction in both systems are oscillatory in the nanopore, and the amplitude of the oscillation is dependent on the strength of solid wall-liquid interaction. Moreover, the six-peak structure of the density profile implies that there were three circular liquid layers formed in this small channel with a size

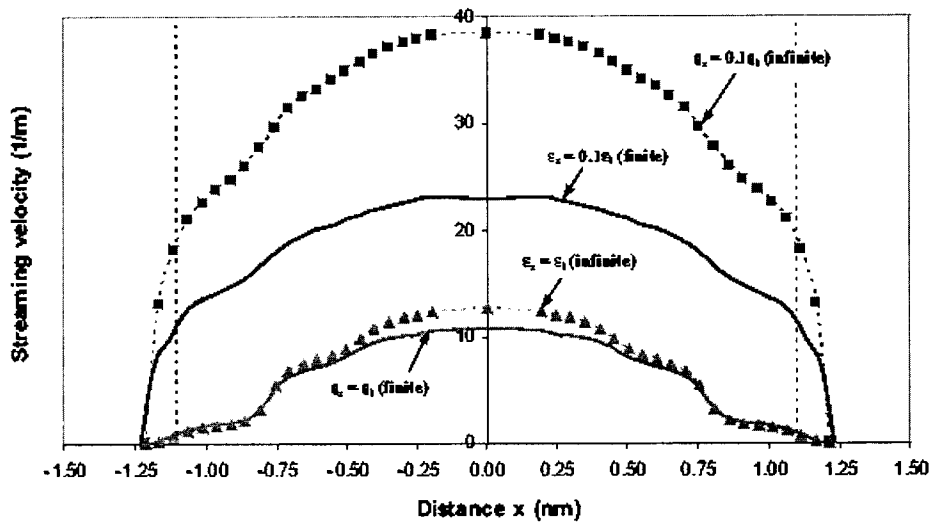

Figure 5.4: Comparison of streaming velocity distributions (averaged over the channel) versus radial distance under different solid wall-liquid interactions in two different systems. Two solid lines are the results obtained in the finite length channel; the dash lines with symbols are results calculated in the infinite length channel. The vertical dash lines are the internal surface of the nanopore.

of 6.5 molecules. Comparing the results obtained in two different systems, one sees that the density distributions in the channel for both systems agree well, except for the value at the first valley close to the solid wall when $\varepsilon_s = \varepsilon_l$.

Fig. 5.4 shows the comparison of the radial distributions of streaming velocity under two different solid wall-liquid interactions in two different systems. Similar to the expressions used the Fig. 5.2 and 5.3, two solid lines are the results obtained in the finite length system; two dash lines with symbols express the results calculated in the infinite system. All curves in the figure show that the velocity distributions in the nanopore are characterized by having a maximum velocity at the center of the nanopore. For solid wall-liquid with the hydrophobic-like interaction, the profile of the streaming velocity in two sys-

tems are similar, while the values are significantly different, i.e., the streaming velocity obtained in the infinite length channel is essentially larger than that obtained in the finite length channel. It means that the effect of the entrance and exit plays a major role in liquid transport through a nanopore if the solid wall-liquid has a hydrophobic-like interaction. However, for solid wall-liquid having a neutral-like interaction, the streaming velocities in two systems show the near same results, except for a slight difference in a central region of $r < 0.5$ nm.

The number flow rates per unit nanosecond in the finite channel are 1111 when $\varepsilon_s = 0.1\varepsilon_l$ and 345 when $\varepsilon_s = \varepsilon_l$, respectively. The number flow rates in the infinite channel are 1829 when $\varepsilon_s = 0.1\varepsilon_l$ and 367 when $\varepsilon_s = \varepsilon_l$. Comparing the number flow rates in two different systems, one sees that the effect of the entrance and exit results in the liquid transport ability of the channel decrease about 39% when $\varepsilon_s = 0.1\varepsilon_l$ and 6% when $\varepsilon_s = \varepsilon_l$. This result clearly shows that the entrance and exit plays the role in liquid transport through a nanochannel, and the impact of the entrance and exit on the transport ability of a nanochannel depends on the solid wall-liquid interaction.

5.3 Summary

The effect of the entrance and exit on liquid transport through a cylindrical nanopore was studied by comparing the NEMD results obtained from a finite length channel and an infinite length channel. The NEMD results indicate that the entrance and exit effect of a nanopore results in the liquid transport ability through the nanopore decrease. The strength of the impact of the entrance and exit on liquid motion through the nanopore depends on the solid wall-liquid interaction.

Chapter 6

Comparative Study between Continuum and Atomistic Approaches of Liquid Flow through a Finite Length Cylindrical Nanopore

[note: this chapter is closely related the published work in the Journal of Chemical Physics 126, 224702 (2007)]

6.1 Description of Prototypical Geometry and Boundary Conditions

The physical system of interest in this chapter is a finite thickness membrane that contained a regular array of nanopores, which is same as that described in Chapter 3 and 4. To make this problem prototypical, and computationally tractable, the nanopores in the membrane were modeled as aligned circular cylinders, the liquid was iso-thermal, and the flow through just one of channels was simulated. Fig. 6.1 shows a schematic of the computational system in which (a) and (b) show the geometries and boundary conditions used in the classical N-S calculations and the NEMD simulations, respectively.

The domain sizes for the pore in the N-S calculations included a 6 nm thick

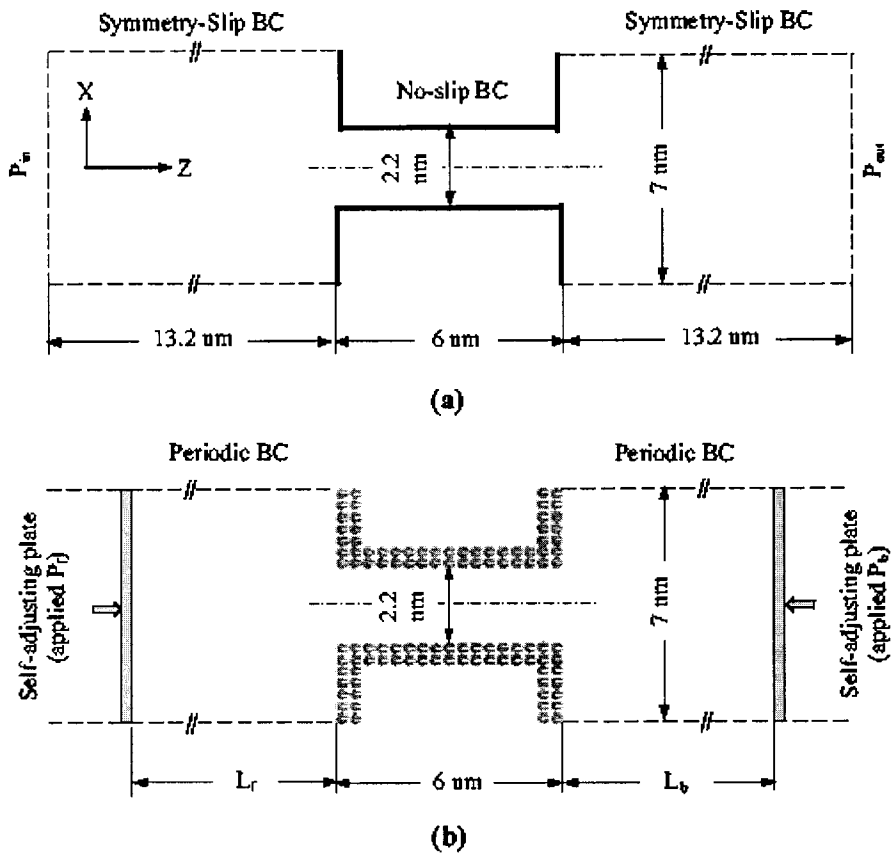

Figure 6.1: Schematic depiction of a single nanopore in a membrane, (a) for classical N-S calculations and (b) for NEMD simulations.

membrane with a 2.2 nm diameter nanopore. The size for the front and back reservoirs were 7 nm in the cross-stream direction (x and y), and 13.2 nm in the stream-wise (z) direction. The boundary conditions employed for N-S equations were no-slip boundary conditions on solid walls, and symmetry-slip boundary conditions on side surfaces of the reservoirs (expressed by dash lines), which mimic a system consisting of a regular array channels. These slip boundary conditions also imply that two reservoirs were semi-infinite, which allows the use of far field boundary conditions at locations far away from the inlet and outlet of the nanopore. Mansouri et al. [133] studied the effect of far field boundary conditions on fluid transport in a micro-channel and they indicated that this influence could be neglected if the ratio of length (from the front/back plate to inlet/outlet of the nanopore) to the diameter of the nanopore was five or greater. In the current simulation this ratio has been set to six.

The fluid properties, in particular density and viscosity, of the iso-thermal liquid used in the N-S calculations were based on liquid argon at 133 K. The choice of this relatively simple fluid was used in order to simplify the NEMD simulations. Furthermore, in order to allow quantitative comparison between the N-S and NEMD calculations these properties were algebraic models developed from the data based on a series equilibrium molecular dynamics simulations at 133 K that span the relevant pressure range.

The physical domain representing the solid walls of the pore for NEMD simulations was constructed to allow for quantitatively comparing between continuum models and NEMD simulations. These walls were assembled from two layers of molecules (totally 2,132 molecules) as shown in Figure 1b, where the minimum spacing between spherical molecules across the channel was 2.2 nm, and the maximum stream-wise distance was 6 nm. This geometry was same as

that used in Chapter 3. For more details, please refer to Chapter 3 or reference [62].

6.2 Numerical Methods and Models

For the continuum approach, the hydrodynamic problem was modeled in the framework of the classical Navier-Stokes (N-S) equations. For compressible flow, the governing equations are

$$\frac{\partial \rho}{\partial t} + \nabla \bullet (\rho \vec{\mathbf{V}}) = 0 \tag{6.1}$$

$$\rho \frac{D\vec{\mathbf{V}}}{Dt} = -\nabla \mathbf{P} + \nabla \bullet (\mu \nabla \vec{\mathbf{V}}) + \frac{1}{3} \nabla (\mu \nabla \bullet \vec{\mathbf{V}}) \tag{6.2}$$

where ρ is the liquid density; μ is the dynamic viscosity; $\vec{\mathbf{V}}$ is the velocity vector; $\mathbf{P}$ is pressure and t is time.

It is common when calculating isothermal liquid flows that the fluid is considered incompressible, and the fluid properties are then treated as constant. As a result, the properties are typically extracted from the spatial derivatives in the above equations, but due to extreme pressure changes that will be imposed on the flow here, the more general N-S formulation was used. Sub-models to capture the variations in density and viscosity as the liquid was transported through the nano-pore were required. These sub-models will be developed in the following Results section of this chapter.

Having developed a hydrodynamics model that allows for spatial variations in fluid properties, the opportunity presented itself to explore the relative importance of including these effects. The result presented here will therefore initially involve data from four numerical N-S approaches, which include cases

where density and viscosity as constants, viscosity as constant and density as a variable, density as constant and viscosity as a variable, and density and viscosity as variables. Interest in considering formulations with reduced physics was associated with the profound savings in their computational time, as well as helping to identify the source and magnitude of errors introduced by the reduced physics.

The MD method used to simulate fluid transport through a finite length nanopore was based on a technique proposed in this thesis. To save computational time, the NEMD results obtained in Chapters 3 and 4 were used to compare with those calculated by classical Navier-Stokes equations.

6.3 Results and Comparisons between Models

Given that the objective of this study was to quantitatively compare results between a conventionally applied continuum model to those based on a NEMD simulation for a prototypical problem, the characteristics of the fluid at the molecular and macro scales must be consistent. At the macro-scale these fluid characteristics were captured by the bulk fluid properties of density and viscosity, while at the molecular scale these characteristics were modeled by the Lennard-Jones parameters. To provide the required quantitative consistency, sub-models for fluid properties over the appropriate range of states were developed using equilibrium molecular dynamics (EMD) simulations in the following subsection. Once those sub-models were created, the two simulation approaches could be performed, and their results were compared in terms of flow rate, and pressure, density and velocity distributions.

6.3.1 Sub-Models for Density and Viscosity at a Fixed Temperature

Experimental studies have shown that the bulk dynamic viscosity of liquid argon is a function of temperature and pressure [134–137]. Lowry [134] also indicated that at constant density the dynamic viscosity is insensitive to changes in temperature, which implies that density is a main factor influencing dynamic viscosity. Since the current problem involves large variations in pressure, a model was first developed to relate pressure to number density, which was then extended to independently relate number density to viscosity. These models were built on data collected from EMD simulations with specified number densities in a canonical (NVT) ensemble (2,597 argon molecules placed in a cube subjected to periodical boundary conditions in all directions). In all EMD simulations, the cutoff distance was $r_c = 2.5\ \sigma$ and the time step used was $0.5\ fs$. Figure 6.2 shows the variation of pressure with respect to number density from these calculations. A linear relationship between the natural logarithm of pressure, ln(P), and number density was modeled with empirical coefficients, such that

$$P = 22.3exp[0.38874(\rho_n - 16.5)] \tag{6.3}$$

where P is the pressure in MPa; ρ_n is number density with units $1/nm^3$. Note the above equation can only be valid at temperature $T = 133\ K$. The root mean square (rms) and maximum differences between the EMD data and the above model are 0.32% and 0.5%, respectively.

According to the linear response theory of a fluid in equilibrium, the bulk dynamic viscosity of liquid argon can be expressed as a time integral of a mi-

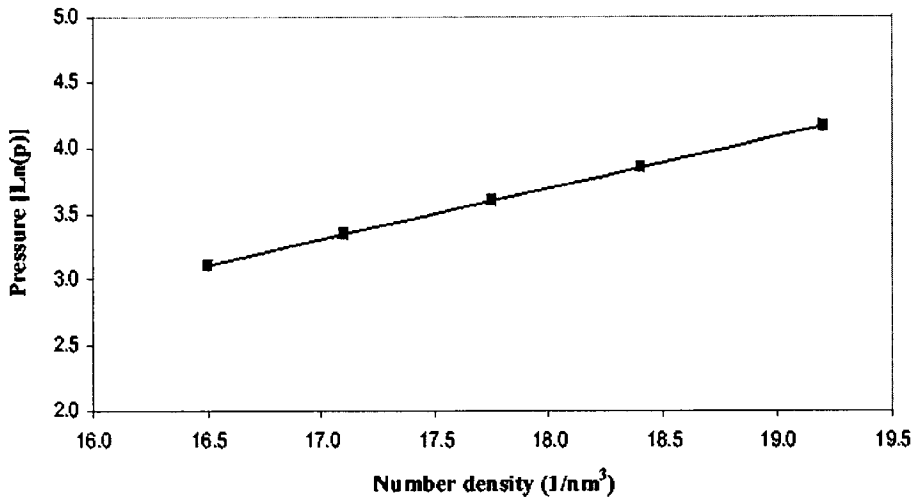

Figure 6.2: Pressure of liquid argon at $T = 133\ K$ as a function of number density. The units of pressure is MPa.

croscopic time-correlation function, which was calculated by

$$\mu = \frac{\forall}{3k_bT}\int_{t_0}^{(t-t_0)\to\infty} \langle \sigma_{xy}(t)\sigma_{xy}(t_0) + \sigma_{xz}(t)\sigma_{xz}(t_0) + \sigma_{yz}(t)\sigma_{yz}(t_0)\rangle dt \qquad (6.4)$$

To illustrate this method of estimating viscosity, the case of a number density of 17.75 $(1/nm^3)$ and temperature 133 K was used. Figure 6.3 depicts the variations of dynamic viscosity and the stress auto-correlation function (SACF) with respect to the integral time. The ten curves drawn with thin lines in this figure correspond to ten different periods. For each curve, 5000 different initial times (t_0) were chosen. From the inset in Figure 6.3, the SACF distribution for all curves decreases monotonically with integral time for small $t - t_0$, but decay in an oscillatory pattern when $t - t_0$ is larger than some value, 0.4 ps for this case. The bold line in Figure 6.3 represents the mean value of the ten curves. The amplitude of oscillation for this mean curve was very small at large $t - t_0$,

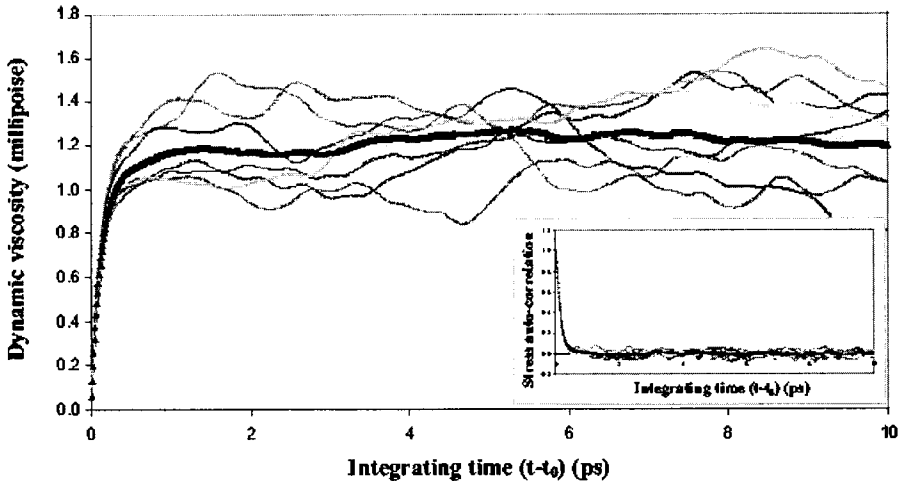

Figure 6.3: Dynamic viscosity of liquid argon at $T = 133\ K$ and number density $\rho_n = 17.75\ 1/nm^3$. Thin lines were obtained by 5000 different initial t_0 at different periods; line with symbol ▲ is the mean of them. The inset is the stress auto-correlation function corresponding to the dynamic viscosity shown in the figure.

and should tend to zero if the number of initial times used is large enough. The dynamic viscosity, expressed by the area under the curve of the SACF times the square of mean initial stress, is shown in Figure 6.3. For each of the thin lines, the dynamic viscosity varies as integral time increases, but the average value of them changes insignificantly as integral time increases. The dynamic viscosity was evaluated to be 1.23 millipoise (averaged value from $t - t_0 = 5$ to $10\ ps$) for this case.

The dynamic viscosities were calculated at number density of 16.5, 17.1, 17.75, 18.4 and 19.2 ($1/nm^3$) and at a constant temperature of 133 K, which span the pressure range of 22 to 64 MPa. The relationship between mean bulk dynamic viscosity and number density is shown in Figure 6.4. The error bar in this figure represents the standard deviation of the individual viscosity data

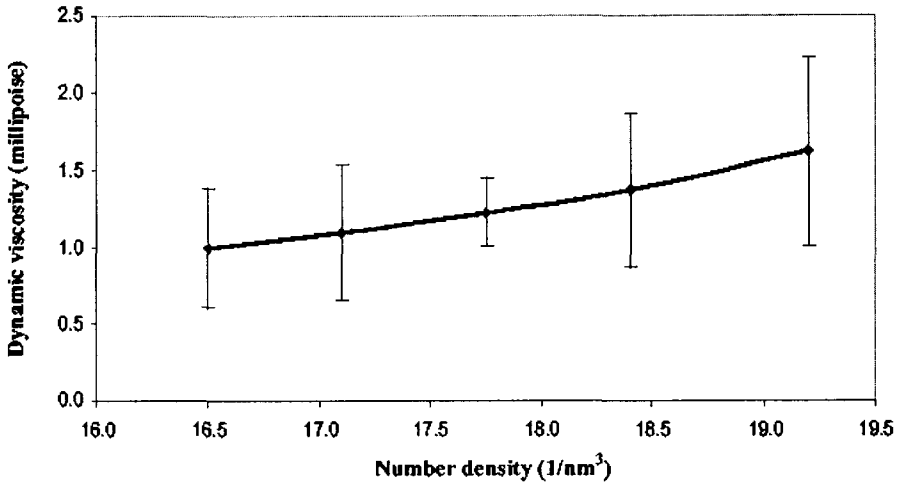

Figure 6.4: Dynamic viscosity of liquid argon as a function of number density at $T = 133\ K$. The error bars represent the standard deviation.

(10 data points) that made up the mean. Lowry et al. [134] provided two sets of experimental results (101.8 K and 128.2 K) of liquid argon under different pressures to validate the viscosity model developed from the EMD simulations. Figure 6.5 shows the comparison of EMD predictions with experimental measurements [134]. In the figure, the two solid lines are the experimental measured viscosity at two different temperatures. If it is assumed that the dynamic viscosity has a linear relationship with temperature, the dynamic viscosity at $T = 133$ K can be obtained approximately by extrapolation from the experimental data. This extrapolated result is shown by dash line in the same figure with respect to the EMD predictions (i.e., the mean values shown in Fig. 6.4), which are depicted by the symbols. The dynamic viscosity is proportional to the pressure,

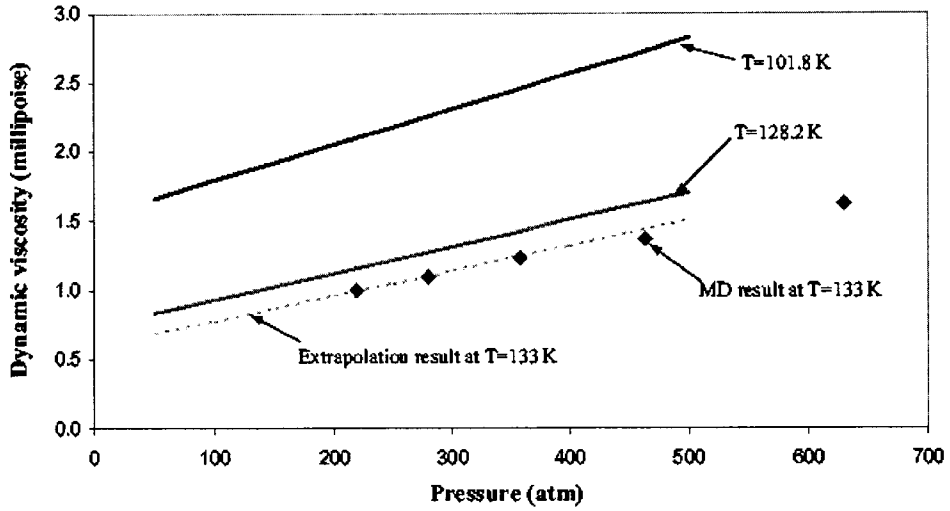

Figure 6.5: Comparison of dynamic viscosity of liquid argon predicted by EMD simulations with experimental results conducted by Lowry et al. Two solid lines are the experimental measurements; the dash line is a linear extrapolation of data based on the experimental measurements and assumption of linear relationship between dynamic viscosity and temperature; symbol ♦ is the EMD prediction.

and this relationship for $T = 133\ K$ can be modeled approximately as

$$\mu = 0.66 + 0.0151P \tag{6.5}$$

The dynamic viscosity μ is in millipoise and pressure is in MPa. The rms difference and maximum difference between the EMD data and this viscosity model were 1% and 1.8%, respectively. These models for number density and viscosity provide a consistent set of fluid characteristics in order to conduct N-S and NEMD simulations for quantitative comparisons.

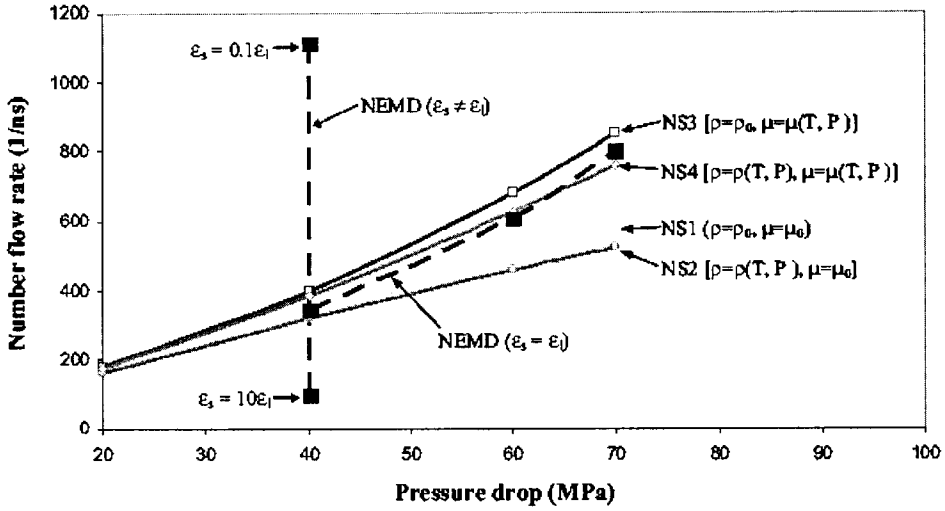

Figure 6.6: Comparison of number flow rates obtained by N-S models and NEMD simulations. The solid lines with open symbols are the results predicted by different N-S models under different pressure drops across the nanopore. The dash line in the horizontal direction are the NEMD results obtained under different pressure drops but with the neutral-like solid-liquid interaction; the vertical dash line are the NEMD results under a constant pressure drop while the solid wall molecules have different interactions with liquid.

6.3.2 Comparisons between Models

6.3.2.1 Comparison of Flow Rate

Being able to accurately calculate the flow rate, or particle flux, through a membrane is a parameter of basic importance for this flow situation. Figure 6.6 shows the number flow rate through one channel obtained by the two different modeling approaches. In this figure, there are two sets of results, one set was obtained from classical continuum theory based on the N-S equations (shown by solid lines with open symbols) and the other was obtained by NEMD simulations (shown by dash lines with closed symbols).

For the N-S results, four different models were run to investigate the effects

of density and viscosity variation on liquid transport through the nano-pore. Three of these models involved simplified property models, while one involved the complete property models described by Equations 6.3 and 6.5. In Figure 6.6 the labels for the various models are:

NS1: constant density and viscosity [$\rho = \rho_0$, $\mu = \mu_0$],

NS2: variable density but constant viscosity [$\rho = \rho(T, P)$, $\mu = \mu_0$],

NS3: constant density but variable viscosity [$\rho = \rho_0$, $\mu = \mu(T, P)$] and

NS4: variable density and viscosity [$\rho = \rho(T, P)$, $\mu = \mu(T, P)$],

where the subscript "0" represents conditions in the upstream reservoir. For each of these N-S models, four numerical simulations were carried out for a fixed upstream reservoir pressure (80 MPa), but different pressure drops across the nano-pore (ΔP = 20, 40, 60, 70 MPa). Among these models, NS1 is the simplest, and the one that is usually used in modeling incompressible macroscopic flow systems. The advantage of this model is that it consumes less computational resources and time. The NS4 is the most complicated model, and its results were expected to give greater accuracy by including more physics, but it consumes more computational resources and time. In a typical calculation, for example a pressure drop of 40 MPa, the ratios of computational time for NS4/NS1 was about 2.5.

Other than the obvious trends that larger pressure drops create larger flow rates, the flow rate results of the four N-S models converge at smaller pressure drops when variations in properties are small. When the density and viscosity were modeled as constants, the flow rate was linearly dependent on pressure different (NS1). The highest flow rate occurred when the density was fixed at the upstream reservoir conditions and the viscosity diminished with dropping pressure (NS3). The lowest flow rate was associated with the model that maintained

the viscosity at its highest value in the upstream reservoir and the density diminished with falling pressure (NS2). If we assume that the flow rate calculated by the model NS4 represents the best estimate for the fluid transport through the nano-pore, the model NS3 overestimates the flow rate by 1.9%, 4.4%, 9.1% and 12.1% for the pressure drops $\triangle P$ = 20, 40, 60 and 70 MPa, respectively; while the models NS1 and NS2 underestimate the flow rate (6.6%, 13.6%, 20.% and 24.0%) and (8.3%, 17%, 26.1% and 31.1%) for the same set of pressure drops. It is clear that as the pressure drop across the nano-pore becomes large, using simplified models (NS1 through NS3) yields significant error in predicting the flow rate, especially if the effect of viscosity variation along the channel is ignored.

Two groups of NEMD results are also plotted in Figure 6.6. The data points connected by the vertical dashed line show the NEMD results for a fixed pressure drop (40 MPa), but with different solid wall-liquid interactions ($\varepsilon_s \neq \varepsilon_l$). The data connected by the other dashed line shows the variation of number flow rate predicted by NEMD simulations under a neutral-like solid wall-liquid interaction ($\varepsilon_s = \varepsilon_l$), but varying pressure drop across the nano-pore. Results obtained by NEMD simulations under neutral-like solid wall-liquid interaction and those obtained by N-S calculations, show similar trends and similar absolute magnitudes of flow rate as the pressure drop across the nano-pore was increased. The flow rate obtained by model NS4 and the NEMD simulations with neutral-like interactions were relatively close to each other over this range of pressure drops. For the range of pressure drops between 40 to 70 MPa, the rms and maximum difference in NS4 modeled flow rate compared to the NEMD flow rate were 7% and 10.9%, respectively. The other N-S models did not fare as well with their rms and maximum differences compared to the NEMD. The rms

and maximum differences were 19.3%, 24.7%, 12.1%, and 27.6%, 34.4%, 15.8%, respectively for NS1, NS2 and NS3. A reasonable conclusion at this stages is that the N-S model agrees well with the NEMD simulation on the liquid transport ability through a nano-pore as long as the effects of density and viscosity are taken into account, and the solid wall-liquid interaction is neutral-like ($\varepsilon_s = \varepsilon_l$). Interest in having a continuum solution for these kinds of problems is seen in the savings of computational time. The ratio of computational times between the NEMD to NS4 simulations was a few hundreds.

In classical continuum theory, the effect of solid wall are not normally taken into account. To examine the effects of solid wall-liquid interaction on liquid transport through the nano-pore, two other NEMD simulations were performed at the constant pressure drop of 40 MPa, but with different solid wall-liquid interactions. One simulation had a weak or hydrophobic-like solid wall-liquid interaction ($\varepsilon_s = 0.1\varepsilon_l$), while the other had a strong or hydrophilic-like interaction ($\varepsilon_s = 10\varepsilon_l$) to compare with the previously discussed neural-like case. Once the surface interactions were included in the NEMD, the classical N-S model failed to predict the bulk fluid transport through a nano-pore. Figure 6.6 shows that when there are significant difference in the permittivity between liquid and solid, the predicted flow rate between NEMD and classical N-S modes can differ by a few hundred percent.

To investigate the reasons for the above results, the liquid transport through the nano-pore is considered in greater detail in the following two subsections.

6.3.2.2 Comparison of Pressure and Density Distributions

In this subsection, the pressure and density distributions of the N-S model (now only considering model NS4) and of the NEMD simulations were compared from

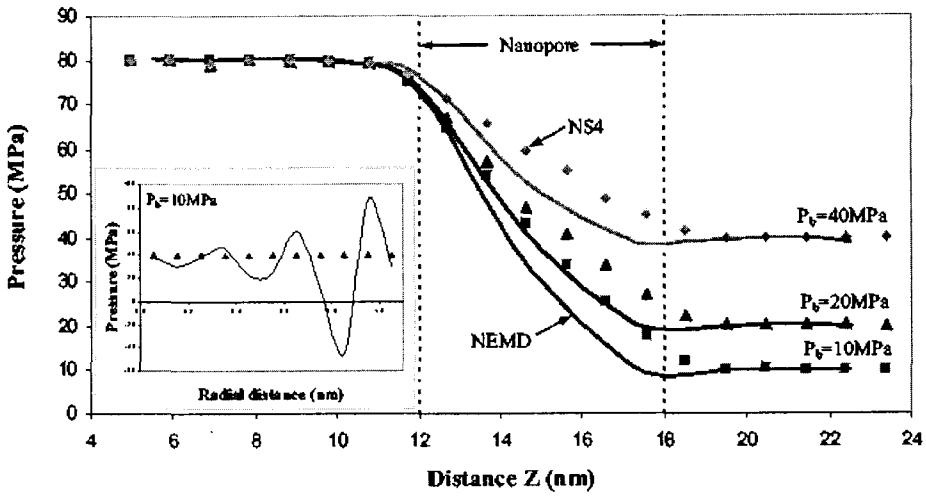

Figure 6.7: Comparison of pressure distributions versus axial distance Z obtained by model NS4 and NEMD simulations for $\varepsilon_s = \varepsilon_l$. The solid lines are the results obtained by NEMD simulations; the symbols represent the results of model NS4. The inset is the comparison of pressure distributions in radial direction between continuum model NS4 (symbols) with NEMD simulation (solid line) for the case with $P_f = 80$, $\triangle P = 70\ MPa$ at the middle section of the nanopore. The vertical dash lines are the front and back surfaces of the membrane.

two different perspectives. The first perspective involved a fixed solid wall-liquid interaction ($\varepsilon_s = \varepsilon_l$), but different pressure drops across the nano-pore, while the second involved a constant pressure drop, but different solid wall-liquid interactions ($\varepsilon_s \neq \varepsilon_l$). The conditions under which these comparisons were made were the same as those described in the previous section regarding flow rate (i.e., the same conditions as the five NEMD data points shown in Figure 6.6).

Figures 6.7 and 6.8 show the comparisons of pressure distributions in the stream-wise direction along the channel between the N-S and NEMD results for these two perspectives, respectively. In Figures 6.7 and 6.8, as with all

subsequent figures in this chapter, the solid lines without symbols are for the data points represent the NEMD simulations and the unconnected data points represent the N-S predictions. The NEMD results shown in these two figures were the averaged values across the entire cross-section, calculated in a 2 nm long computational box in the z-direction by the Irving-Kirkwood equation.

The pressure distributions in Figure 6.7, where $\varepsilon_s = \varepsilon_l$, all have similar patterns. The pressure changes monotonically between the reservoirs, with the N-S predictions being consistently higher in the nano-pore, and the NEMD simulation achieving the downstream reservoir pressure prior to the end of the channel, while the N-S calculation does not reach this pressure until after the end of the channel. The inset of Figure 6.7 shows a comparison of radial pressure between N-S model and NEMD for the case of $\triangle P = 70\ MPa$. The radial pressure distributions obtained by these two approaches were completely different from each other. The N-S model predicted a nearly constant pressure across the channel, while the NEMD simulation results showed the well-known wave-like distribution of pressure near a wall, which for a channel of this size extends across the entire diameter.

When the liquid wall-solid interactions were altered from $\varepsilon_s = \varepsilon_l$ to $\varepsilon_s \neq \varepsilon_l$, the stream-wise pressure distribution averaged over the channel diameter for the NEMD simulation was also affected. Imposing strong or hydrophilic-like interaction ($\varepsilon_s = 10\varepsilon_l$) cause the radial wave-like pressure distribution to be exaggerated from the neutral-like case, as depicted in the inset of Figure 6.8. Similarly, shown in the same inset, when weak or hydrophobic-like interactions were imposed ($\varepsilon_s = 0.1\varepsilon_l$) the NEMD radial wave-like pressure field was less pronounced. Consequently, Figure 6.8 shows that the stream-wise pressure distribution of the N-S calculation more closely matched the weaker interactive

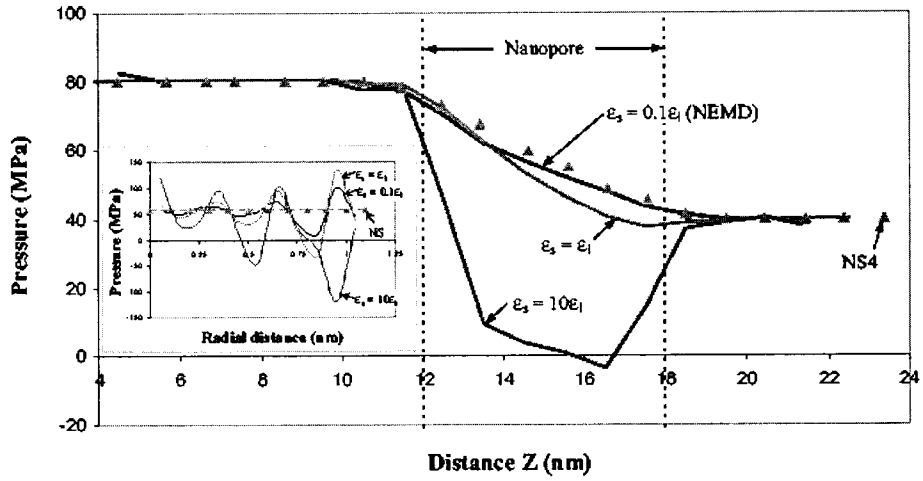

Figure 6.8: Comparison of pressure distributions versus axial distance Z obtained by model NS4 and NEMD simulations for $\varepsilon_s \neq \varepsilon_l$. The solid lines are the results obtained by NEMD simulations; the symbols are the prediction obtained by model NS4. The inset is the comparisons of pressure distributions in radial direction between continuum model NS4 (symbol or dash line with symbol) with NEMD simulations (solid lines). The vertical dash lines are the front and back surfaces of the membrane.

force case, and deviate dramatically from the strongly attractive force when $\varepsilon_s = 10\varepsilon_l$. This observed phenomenon means that the N-S model should only be used to predict the stream-wise pressure distribution in a nano-pore with conditions put on the applicable range of $\varepsilon_s/\varepsilon_l \leq 1$.

The insets in Figures 6.7 and 6.8 also show that if the solid wall has a weak interaction with liquid ($\varepsilon_s = 0.1\varepsilon_l$), the pressure had its strongest peak above the mean and close to the solid wall, while if the solid wall has a strong interaction with liquid ($\varepsilon_s = 10\varepsilon_l$), the opposite was observed. The negative peak for the $\varepsilon_s = 10\varepsilon_l$ case was large enough to drive the pressure averaged across the channel to be negative at some locations. This negative pressure is indicative of a net tensile force on the channel wall, which was sustained by the

strong solid wall-liquid interactive force and flow in the channel center.

Figures 6.9 and 6.10 are the equivalent sets of data to Figures 6.7 and 6.8, except they track the number density distributions in the flow. The boundary conditions for the N-S and NEMD simulations were imposed by pressure, and hence pressures in the reservoirs were predetermined to be essentially identical between these two approaches (c.f. Figures 6.7 and 6.8). Density, on the other hand, is a dependent variable in the two approaches, and need not necessarily have the same values. The relationship between pressure and density was derived from EMD with no mean flow velocity, while in the current flowing simulations there can be considerable local velocities (discussed in detail in the next subsection). Figure 6.9 shows that the density distributions obtained by the N-S and NEMD simulations were in good agreement in the upstream reservoir. Though, in the downstream reservoir, the densities observed by the two methods exhibited marked differences, and these differences increased as the back pressure was decreased. Possible reasons for this observation could be related to difference in the velocities field at the boundaries, and the potential for phase transition at the outlet of the nano-pore for the case with lower back pressure. The rigid nature of the self-adjusting plates used to control the pressure in the reservoirs of the NEMD simulations, explicitly set a uniform velocity profile at their locations. In the N-S calculation only the pressure was set at the boundary, any non-uniformities in velocities at the plane where the pressure was set appear as variations in density. The asymmetry between the densities differences in the upstream and downstream reservoirs is proposed to result from the asymmetry of flow entering and exiting a channel. Flow entering a channel draw essentially uniformly from reservoir within a couple of channel diameters, while flow exiting a channel persist in the form of jet for

many diameters. (Emphasizing the differences between sucking and blowing a fluid.) An alternate reason for the asymmetry in density difference is that the NEMD simulations can also take into account of potential phase change, while N-S equations can not.

As with the pressure distributions, the solid wall-liquid interactions can have a profound effect on the density distributions averaged across the channel. Figure 6.10 shows that the density distribution along the channel obtained by N-S equations was only consistent with that obtained by NEMD simulation for solid-liquid having a near neutral-like interaction. If the solid and liquid depart from a neutral-like interaction, the classical N-S model was unable to predict the averaged density distributions along the nano channel. Moreover, the NEMD simulation captured an effect that appears to be associated with the entrance and exit of the nano-pore on the density distribution along axial direction for strong solid-liquid interaction (though somewhat visible in the neutral-like interaction). These are the two peaks in density that extend outside the channel, while N-S equations provided no evidence of this feature and show only monotonic change along the channel's length.

The insets in Figures 6.9 and 6.10 provide a comparison of density distributions in the radial direction at middle location of the nano-pore. The inset in Figure 6.9 only shows the comparison for the case with $\triangle P = 70\ MPa$. Like the radial pressure distribution the NEMD showed wave-like distribution in density normal wall direction, while the density field produced by the N-S equations is essentially constant.

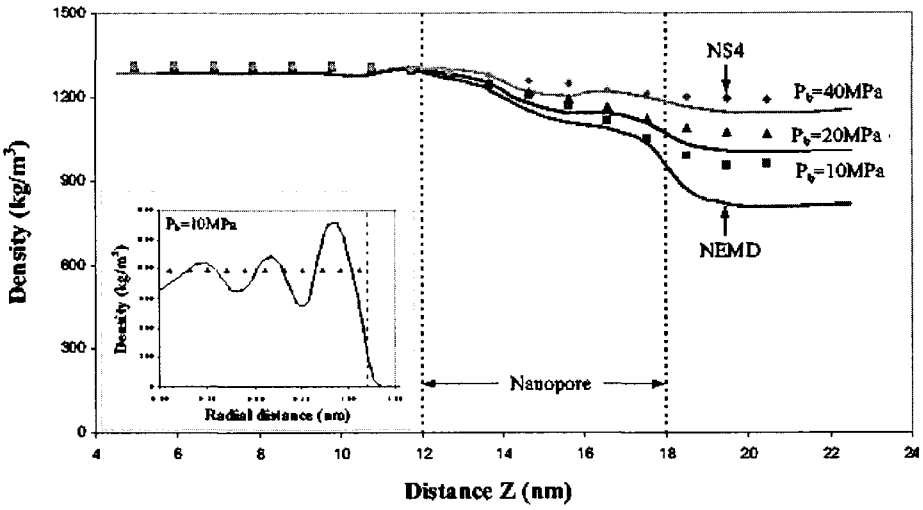

Figure 6.9: Comparison of density distributions versus axial distance Z obtained by model NS4 and NEMD simulations for $\varepsilon_s = \varepsilon_l$. The solid lines are the results obtained by NEMD simulations; the symbols are the results of model NS4. The inset is the comparison of density distributions in radial direction between model NS4 (symbols) with NEMD simulations (solid line) at the middle section of the nanopore for the case with $P_f = 80$, $\triangle P = 70\ MPa$. The vertical dash lines are the front and back surfaces of the membrane.

6.3.2.3 Comparison of Streaming Velocity Distributions

Figures 6.11 and 6.12 are the equivalent to the previous pairs of data (Figures 6.7 and 6.8, and Figures 6.9 and 6.10) in terms of conditions and presentation, except that they show the streaming velocity (i.e., velocity in the z direction). These streaming velocities represent this component of velocity averaged across the plane of either the entire channel, or reservoir. As a result, the velocity in the reservoirs was small partially due to the fact that the bulk of the fluid in the reservoirs has little or no z-wise velocity.

The comparisons of the averaged streaming velocity distributions in the stream-wise direction between the N-S and NEMD simulations are remarkably

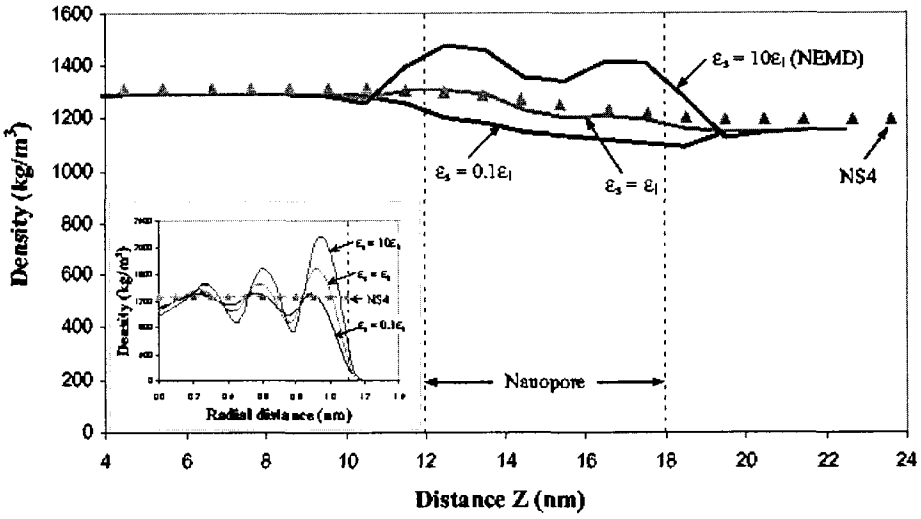

Figure 6.10: Comparison of density distributions versus axial distance Z obtained by model NS4 and NEMD simulations for $\varepsilon_s \neq \varepsilon_l$. The solid lines are the results obtained by NEMD simulations; the symbols are the prediction by model NS4. The inset is the comparison of density distributions in radial direction between model NS4 (symbols) and NEMD simulations (solid lines) at the middle section of the nanopore. The vertical dash lines are the front and back surfaces of the membrane.

consistent when there was neutral-like interactions between the solid and liquid. When the solid and liquid had a weak or hydrophobic-like interaction, the averaged streaming velocity obtained by NEMD simulation was much higher than that obtained by the N-S model. In contrast, NEMD simulation gave a much lower averaged streaming velocity than that obtained by the N-S model if the solid wall-liquid had a strong or hydrophilic-like interaction. The reason for this deviation in mean streaming velocity with differing solid wall-liquid interactions can easily be seen in the radial distributions.

The streaming velocity distributions in the radial direction at the mid-length of the nano-pore was taken as the location for comparison between the N-S and

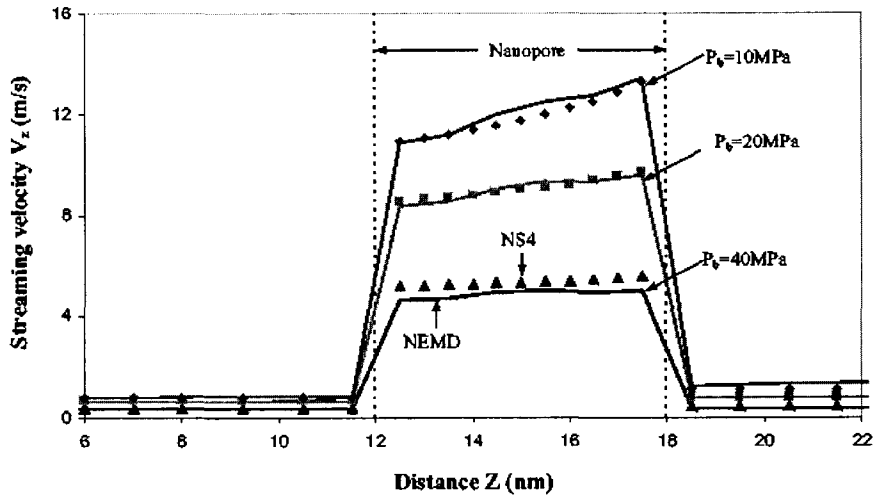

Figure 6.11: Comparison of streaming velocity distributions versus axial distance Z obtained by model NS4 and NEMD simulations for $\varepsilon_s = \varepsilon_l$. The solid lines are the results obtained by NEMD simulations; the symbols are the results of model NS4. The vertical dash lines are the front and back surfaces of the membrane.

NEMD approaches, and are shown in Figure 6.13 and 6.14. These two figures show the mean velocities from the NEMD simulation being non-zero at locations slightly beyond the physical extent of the channel. The velocity distribution obtained from the N-S model was a parabolic distribution; which is consistent with that of low Reynolds number flow. The velocity distribution obtained by the NEMD simulations with neutral-like interactions had a similar pattern, as shown in Figure 6.13, but there were some regularly appearing features that were different, especially in the regions close to the solid wall. The magnitude of the streaming velocity became increasingly different as the pressure difference increased. To examine the consistency in the shape of the velocity profiles obtained by two different methods, all the velocities were normalized using their own centerline velocity ($x = 0$), and plotted in the inset of Figure 6.13. The

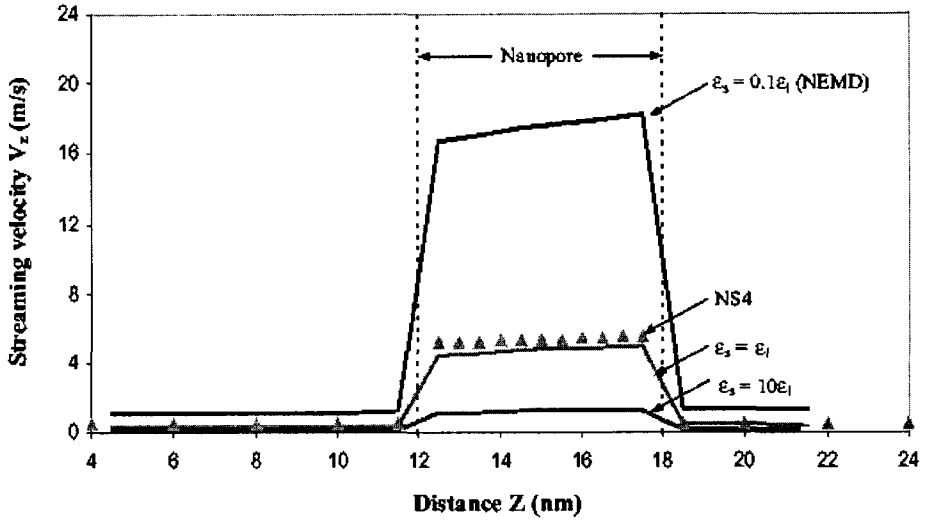

Figure 6.12: Comparison of streaming velocity distributions versus axial distance Z obtained by model NS4 and NEMD simulations for $\varepsilon_s \neq \varepsilon_l$. The solid lines are the results obtained by NEMD simulations; the symbols are the prediction of model NS4. The vertical dash lines are the front and back surfaces of the membrane.

inset in Figure 6.13 clearly shows that the velocity profiles for two methods for neutral-like interactions were remarkably consistent and similar, except for the persistent velocity feature near the wall of the NEMD approach.

Figure 6.14 once again shows that the most profound incapacity of classical N-S modeling in describing the changing solid wall-liquid interactions. This figure indicates that the streaming velocity in the nano-pore had an inverse relationship with the solid wall-liquid interaction, i.e., solids with a small energy scale produce large streaming velocities, while the solids with a large energy scale produce small streaming velocities. Moreover, the solid with a small energy scale results in the liquid slipping at the solid-liquid interface, while the solid with a large energy scale results in a layer of liquid molecules sticking to the

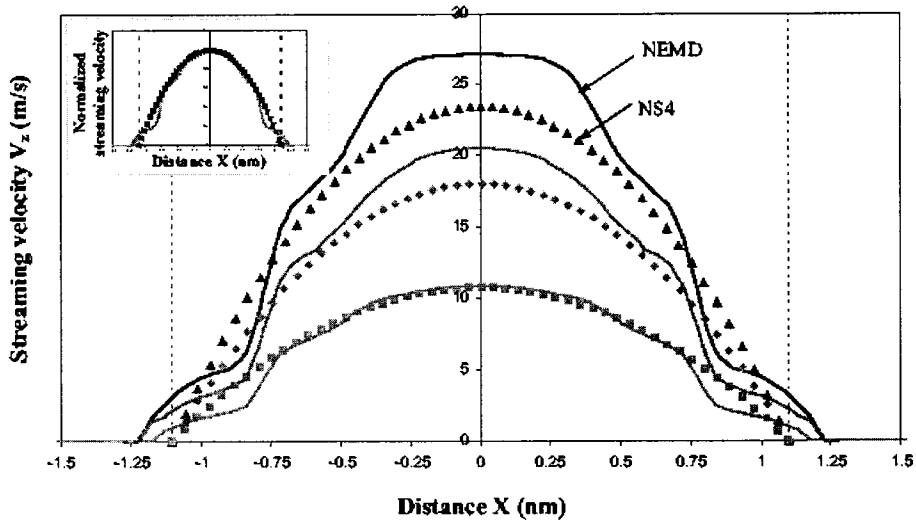

Figure 6.13: Comparison of streaming velocity distributions in radial direction obtained by model NS4 and NEMD simulations for $\varepsilon_s = \varepsilon_l$. The solid lines are the results predicted by NEMD simulations; the symbols are results obtained by model NS4. The inset is the comparison of normalized streaming velocity profiles between model NS4 and NEMD simulations. The vertical dash lines are the internal surface of the nanopore.

solid. Comparing results obtained by N-S and NEMD simulations, it is noted again that the N-S results were only consistent with those obtained by NEMD simulations when the solid has a near neutral-like interaction with liquid.

In summary, if the solid energy scale deviates significantly from that of the liquid then the results obtained from N-S and NEMD simulations will be appreciably different. The above data suggests that the classical N-S equations can only be used to predict the averaged fluid transport through nano-pores if the solid wall material has the similar properties as the liquid ($\sigma_s \approx \sigma_l$ and $\varepsilon_s \approx \varepsilon_l$) and the channel diameter is equal to or larger than 6.5 times of liquid molecule size. To properly predict the liquid transport by using N-S equations for cases in which the properties between the solid wall material and liquid are

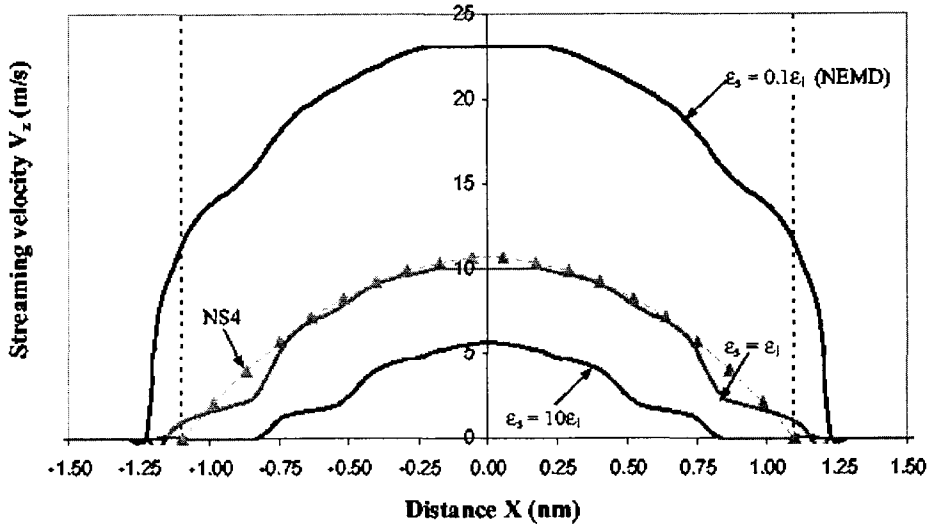

Figure 6.14: Comparison of streaming velocity distributions in radial direction obtained by model NS4 and NEMD simulations for $\varepsilon_s \neq \varepsilon_l$. The solid lines are the results obtained by NEMD simulations; the symbols are the prediction by model NS4. The vertical dash lines are the internal surface of the nanopore.

essentially different, the more detail sub-models that involve the interactions of solid wall material to liquid have to be developed. Another potential method that accounts for the variation of parameters (e.g., density, viscosity, etc.) in the direction normal to the solid wall into the N-S equations is the local average density model (LADM) proposed by Bitsanis et al. [40, 64]. To insert the LADM into the N-S equations, the solid-liquid boundaries have to be dealt properly if the solid wall-liquid deviates from a neutral-like interaction.

6.4 Summary

The prototypical problem of steady-state pressure driven liquid flow through a finite length cylindrical nano-pore that connected two semi-infinite reservoirs

was used to compare model results based on classical Navier-Stokes (N-S) hydrodynamics and non-equilibrium molecular dynamics (MD) simulations. The nano-pore was nominally 2.2 nm in diameter and 6 nm long, while the fluid, argon, was treated as a compressible Lennard-Jones liquid with variable dynamic viscosity. For the MD simulations the inter-molecular properties of the walls were specified independently from the liquid's. Comparisons between the models were made in terms of total flow rate through the nano-pore, as well as distributions of pressure, density and velocity.

The results showed that

1. The variation in both density and viscosity in the stream-wise direction play the role for liquid transport through the channel, in particle viscosity variation in the stream-wise direction. In order for the N-S equations to predict the same trends in total flow rate with increasing pressure difference as the MD simulation, sub-models for variations in density and viscosity with pressure needed to be included.

2. The classical N-S equations with no-slip boundary conditions at the walls quantitatively agreed with the flow rate predictions from NEMD simulations only under the condition of having a neutral-like solid-liquid interaction ($\varepsilon_s = \varepsilon_l$). Under these conditions, the N-S and MD models also agreed well in stream-wise distributions of pressure, density and velocity. As the solid wall-liquid interactions were varied away from neutral-like interactions, the classical N-S equations break down.

Chapter 7

Nanomedicine: Molecular Dynamics Simulation of Injection Flow for Lennard-Jones Fluid in a Nanosyringe

7.1 Description of Geometry and Method

Molecular dynamics simulations were performed to study the flow of liquid molecules in a nanosyringe consisting of a larger cylinder located at front and a smaller capillary tube located at back as shown in Fig. 7.1. The front cylinder, the larger one, serves as a reservoir and the smaller cylinder mimics a needle for liquid transport properties. The larger cylinder has an inside diameter of $8.6\sigma_l$ and a length of $6.6\sigma_l$. The inside diameter and length of the needle are $4.8\sigma_l$ and $13.2\sigma_l$, respectively. The solid substrate was made up of two molecular layers with a total of 1,840 molecules, corresponding to a number density $\rho_w\sigma_w^3 = 0.9$. With respect to the liquid, 560 molecules were packed in the front reservoir and most part of needle, having a number density $\rho_l\sigma_l^3 = 0.94$. The initial condition for the simulation was established by introducing an impenetrable plate formed by one molecular layer at $z = 0$ and a rigid plate with zero thickness at the exit of the needle (shown as a box and a solid line in Fig. 7.1, respectively).

To account for the effect of molecules located outside the needle to those inside the needle, the simulation domain was extended to vacuum, as shown by dash lines in the figure. For molecules leaving the extended domain into the vacuum, their influence on the motion of molecules inside the syringe was ignored due to the short range interaction between molecules and truncation algorithm used. The impenetrable plate was used to mimic the surface of a piston; the rigid plate was applied to enclose all molecules for establishing an initial stage. The molecules in this closed system were allowed to move without applying any external force until a thermodynamic equilibrium state was reached. During this period, Berendsen thermostats [65, 72, 89] were coupled to adjust the temperature of the system to be $Tk_b/\varepsilon_l = 1.1$ at the equilibrium state. The needle was then opened by removing the rigid plate located at the exit of the needle and the piston was allowed to move at a constant velocity V_0 simultaneously. After this, molecules began to transport and some moved out of the needle into the vacuum. In simulations, the following parameters were selected [50]: $\sigma_l = 0.312$ nm, $\sigma_w = 0.262$ nm, $\varepsilon_l = 1.08 \times 10^{-21}$ J and $\varepsilon_w = 1.25 \times 10^{-20}$ J. These parameters imply that the solid wall is more hydrophilic due to its energy scale much larger than liquid's.

7.2 Results and Discussion

7.2.1 Isothermal Flow with Low Injection Velocity

The injection velocity used in this section was $V_0 = 0.026\sigma_l/\tau_0$, where τ_0 was the characteristic time defined by $\tau_0 = (m\sigma_l^2/\varepsilon_l)^{1/2}$. To obtain the time-averaged number density and streaming velocity distributions, the channel was divided into 7×30 grid, 7 in the z-direction and 30 sections in the radial direction. The

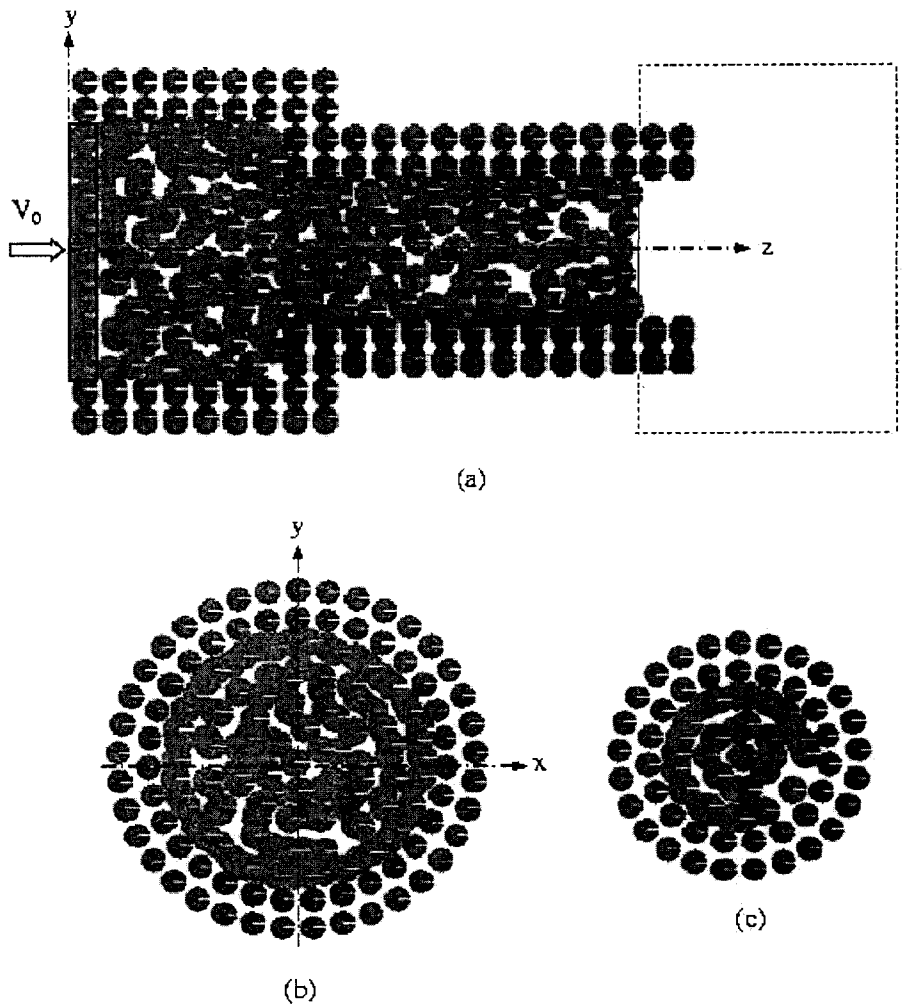

Figure 7.1: Snapshot of simulation setup and molecular packing in the nanosyringe. (a) vertical section through axis of nanosyringe; (b) cross-section at the middle of the front reservoir; (c) cross-section at the middle of nanoneedle. Solid box with molecules in it mimics a piston; solid line located at the end of nanoneedle expresses a rigid plate used to close the needle before injecting; the area formed by dashed lines is the extended computational region.

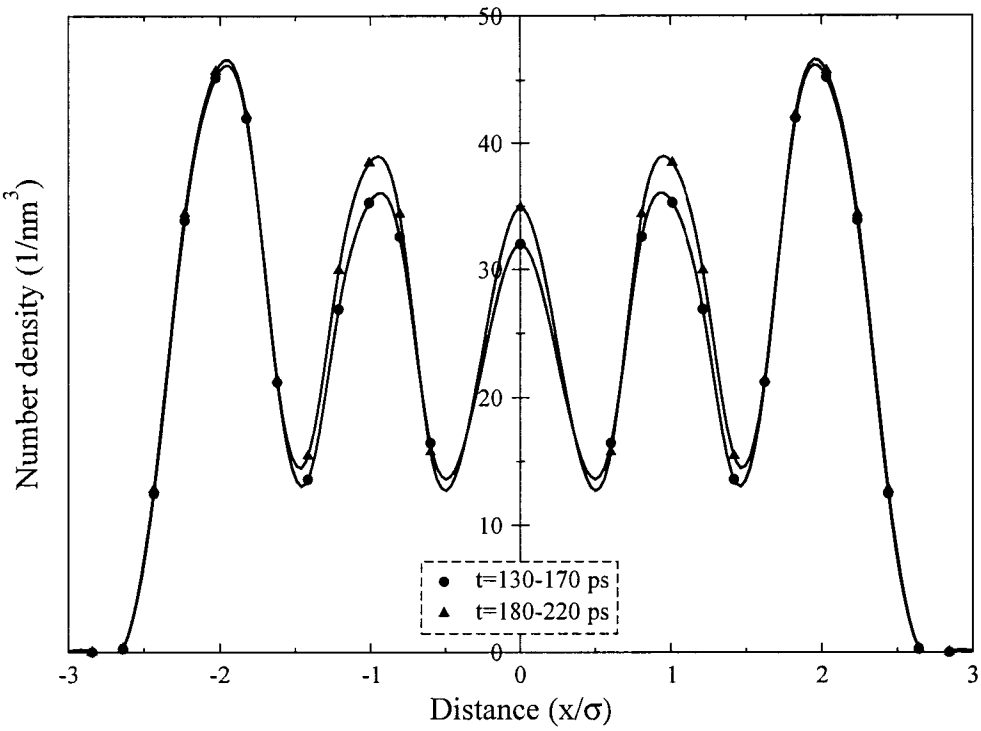

Figure 7.2: Comparison of time-averaged number density distributions at $z = 10.6\sigma_l$ versus radius for isothermal flow at two different times, $t = 130 - 170$ ps and $t = 180 - 220$ ps.

distance for each section in the z-direction is $a \times \triangle L$ (where $\triangle L = L/12$, L is the total length of the computational domain and a=1, 2, 1, 1, 3, 3 and 1 for each section). To quickly obtain statistical values for a small system with limited molecules, equations 2.13 and 2.14 described in Chapter 2 were applied to calculate the density and streaming velocity in the needle.

Figs. 7.2 and 7.3 show, respectively, the time-averaged number density and streaming velocity distributions in the needle at two different average times, $t = 130 - 170$ ps and $t = 180 - 220$ ps. One sees that profiles of density and velocity at two different times are essentially identical, implying that a steady flow with a constant flow rate and temperature can be produced by

using this small device. The density curves in Fig. 7.2 show that the density at the radial direction distributes in an oscillatory fashion and appears to be sensitive to the specific solid wall-liquid interaction. It should be noted that the highest liquid density is near the wall, implying the formation of a liquid layer; the existence of this layer, in turn, induces further formation of liquid layers towards the inside liquid region. This oscillatory density distribution in the direction normal to the wall is similar to those observed in Poiseuille and Couette flows [24, 25, 34–38, 43, 46, 50], but obtained here via a different flow condition. The streaming velocity profile shown in Fig. 7.3 indicates that the streaming velocity changes with respect to radial distance and deviates from the parabolic profile significantly. Comparing Figs. 7.2 with 7.3, one sees that the first liquid layer near the solid substrate does not move. Between the first and second liquid layers, there is a slip velocity, and the slip plate locates at the interface between first liquid layer and second liquid layer, but not at the interface between the liquid and solid. The behaviors shown in Figs. 7.2 and 7.3 suggest that the continuum flow theory is not valid for liquid flow in such a nanosyringe.

Figs. 7.4 and 7.5 show the time-averaged number density and streaming velocity distributions versus the channel axis at $t = 180 - 220$ ps. The density profile in Fig. 7.4 indicates that the density in the front reservoir is slightly higher than that in the needle; the density in most of the needle varies slightly, but decreases dramatically near the outlet. The streaming velocity curve in Fig. 7.5 shows that the streaming velocity in the front reservoir is small. The streaming velocity then increases quickly to a location where molecules enter the needle from the front reservoir. After that the streaming velocity goes up slightly though most of the needle. When molecules move to the exit of

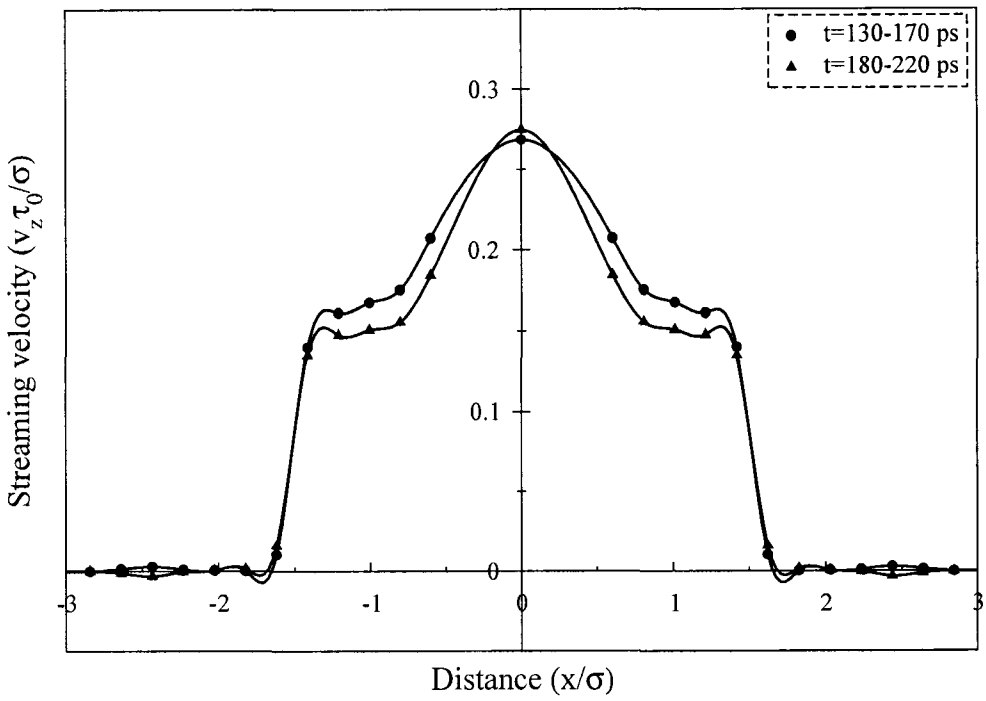

Figure 7.3: Comparison of streaming velocity distributions at $z = 10.6\sigma_l$ versus radius for isothermal flow at two different times, $t = 130 - 170$ ps and $t = 180 - 220$ ps.

the needle, the streaming velocity increases significantly. From Figs. 7.4 and 7.5, It is noted that the density and velocity in most part of the needle remain essentially constant. Thus, middle part of needle was selected to model a steady flow and study its transport properties.

It is noted that the average time in Figs. 7.2 - 7.5 is much larger than the characteristic time of Lennard-Jones potential. The values in these figures express the macroscopic properties of fluid. To see the flow transport microscopically, the averaged time was decreased to 2 fs, and the resulting instantaneous velocities are shown in Figs. 7.6 and 7.7. Fig. 7.6 displays the molecular velocity distributions for the z-component (v_z at $z = 10.6\sigma_l$) versus the radial distance

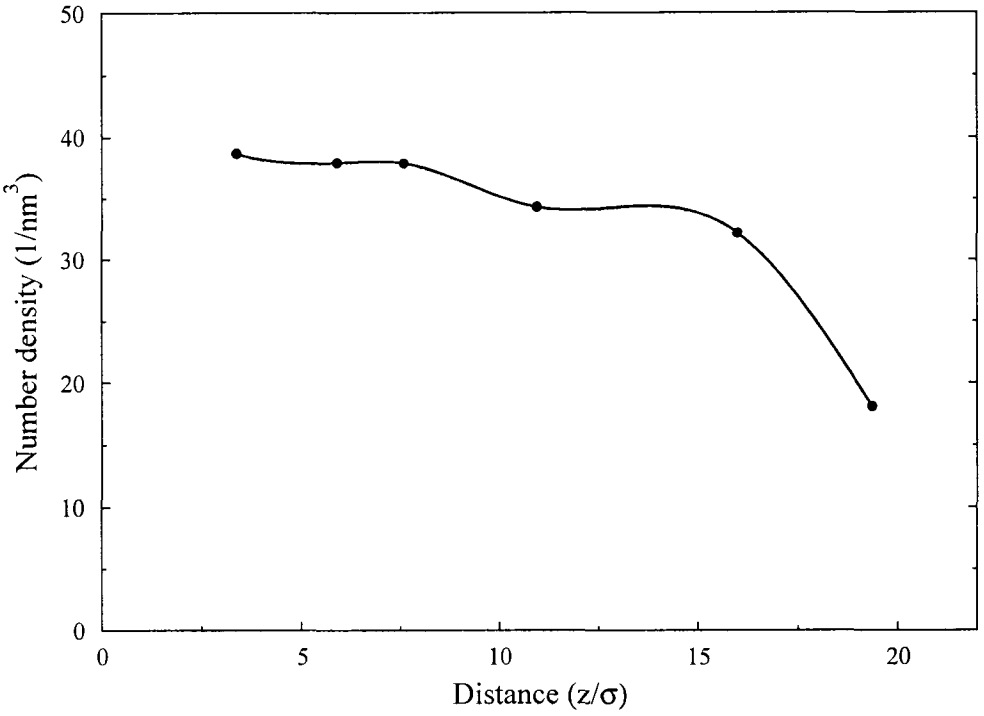

Figure 7.4: Time-averaged number density distribution versus channel axis for isothermal flow at $t = 180 - 220$ ps (line is drawn to guide the eyes for trend of the data).

at three different times, $t = 150.5$, 152 and 153 ps. In this figure, the symbols •, ■ and ▲ correspond to $t = 150.5$, 152 and 153 ps, respectively. At $t = 150.5$ ps, the v_z profile has a peak at the central part of the cylinder and two hollows beside it. At $t = 152$ ps, the velocity at the central part decreases, while that at two hollows increases. After that, i.e., at $t = 153$ ps, the peak changes into a hollow and two hollows change to peaks. These results suggest that, under a constant injection condition, liquid molecules in a nanoneedle transport in a wavelike motion microscopically. Fig. 7.7 displays the molecular velocity distributions for z - component at a different cross-section $z = 15.5\sigma_l$, with the same wavelike pattern.

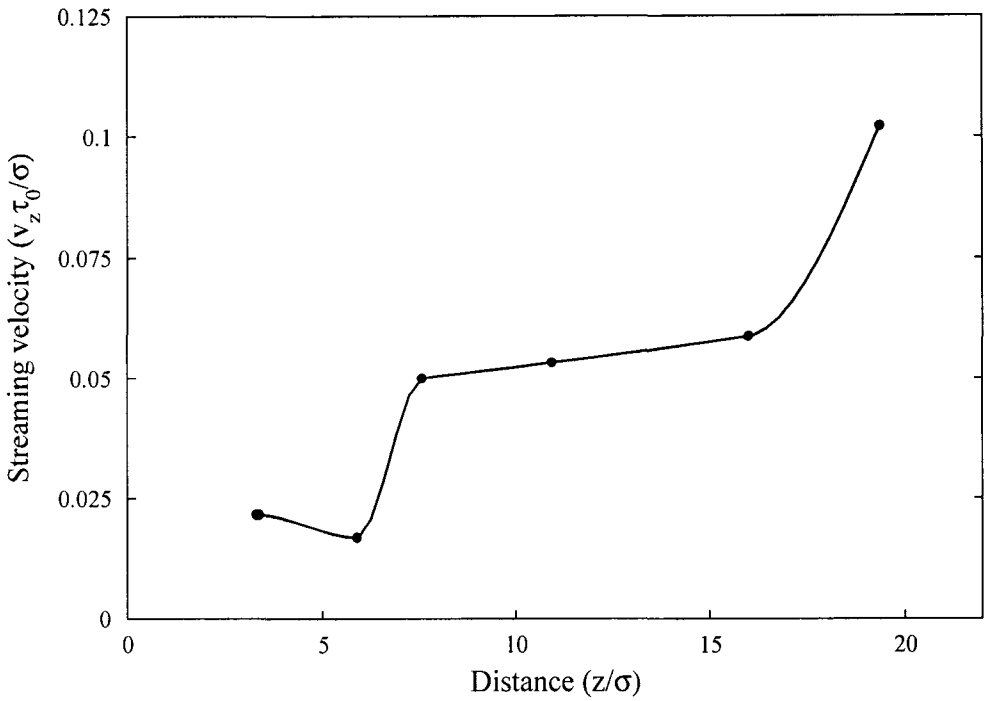

Figure 7.5: Streaming velocity distribution versus channel axis for isothermal flow at $t = 180 - 220$ ps (line is drawn to guide the eyes for trend of the data).

7.2.2 Adiabatic Flow with Constant Injection Velocity

As discussed above, application of a thermostat in a system with periodic boundary conditions is important. However, the use of thermostats imposes additional constraints on the equations of molecular motion. In this section, an injection flow without using a thermostat will be studied. As the time of liquid molecules passing through the nanoneedle is extremely short and heat transfer between the liquid and its surroundings is minute, the heat transfer is neglected and the flow is simplified as an adiabatic process. The advantage of this simplification is that the molecules in the channel are only governed by fundamental equations, Newton's second law and Lennard-Jones potential, no additional constraints are imposed on the molecules.

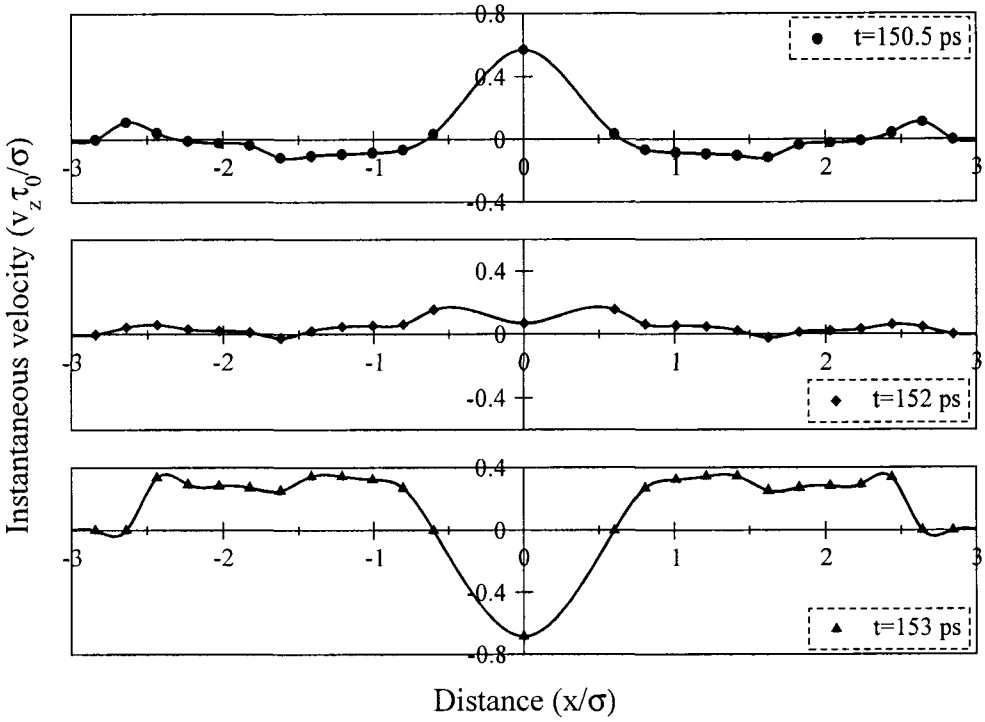

Figure 7.6: Instantaneous velocity distributions versus radius at three different times for isothermal flow at $z = 10.6\sigma_l$.

In this section, the study focuses on the wavelike property and the reason of this phenomenon by using a high injection rate, $V_0 = 0.154\sigma_l/\tau_0$. For the time-averaged density and streaming velocity distributions, they were not shown here as their patterns are similar to those in the previous section.

Fig. 7.8 shows the molecular velocity distributions for the z-component versus radius at three different times. At $t = 19.2$ ps, the v_z profile has a peak at about half the cylinder radius, with two hollows next to the solid wall. After about 0.2 ps ($t = 19.4$ ps), the v_z profile has changed significantly where the two hollows disappear and the profile changes into a quasi-parabolic curve. At $t = 19.65$ ps, the velocity profile appears to have reverted to that at $t = 19.2$ ps. These results also show that, under a constant injection condition, liquid

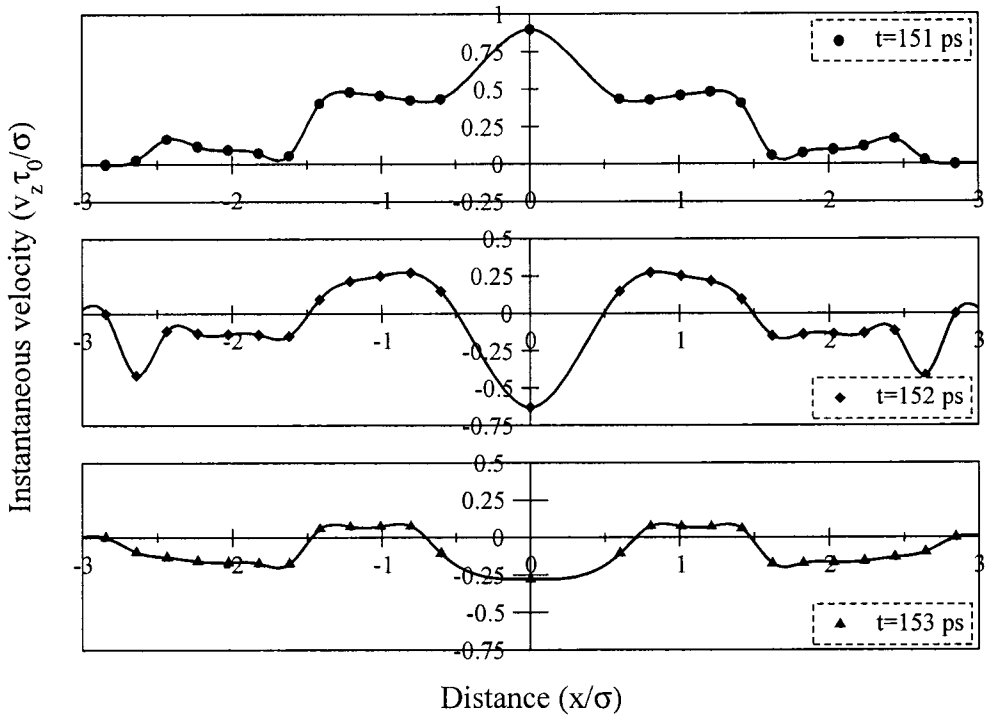

Figure 7.7: Instantaneous velocity distributions versus radius at three different times for isothermal flow at $z = 15.5\sigma_l$.

molecules in a nanoneedle transport in a wavelike motion.

Fig. 7.9 shows the space-averaged velocity distribution with respect to the channel axis at $t = 20$ ps. These results were obtained by dividing the channel uniformly along its z direction into 24 bins. The velocity presented in this picture is the space-averaged velocity in each bin. From the results, one sees that there are two distinct regions: (1) at $z/\sigma < 6.6$ (in the front reservoir), small oscillation appears; (2) when molecules enter the nanoneedle, the magnitude of oscillation increases. The results in this picture clearly illustrate the wavy characteristics of molecules in space dimension. Similar results were also found at different times ($t = 25$, 30, and 40 ps). Thus, a question then arises as to whether or not this wavy characteristics is a result of the non-uniform channel

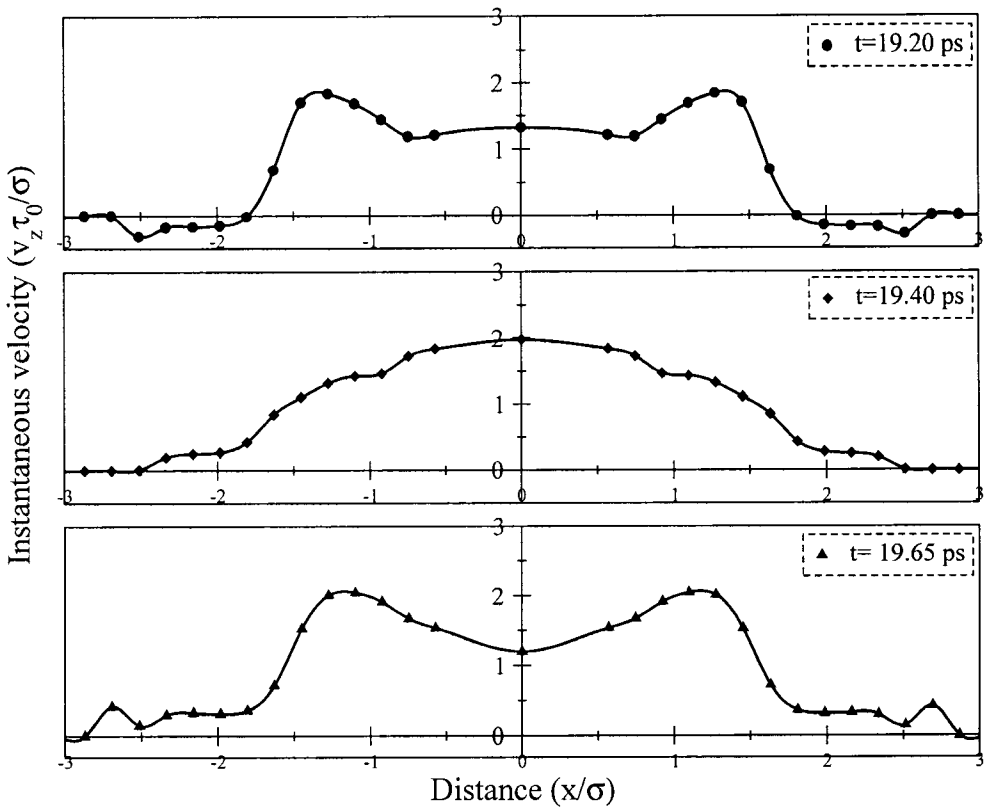

Figure 7.8: Instantaneous velocity distributions at $z = 10.6\sigma_l$ versus radius at three different times for adiabatic flow with high injection rate.

geometry in Fig. 7.1. To verify this, an additional simulation in a straight channel with $d/\sigma_l = 4.8$ and maintained all other parameters to be the same was performed. Results suggest that a similar wavelike motion of molecules also occurs for a straight nanochannel, independent of the channel geometry considered.

Apart from the geometry, such wavy motion of molecules is a consequence of the moving boundary was examined. As a result, the force per unit area of the moving boundary acting on the molecules at different times were studied. Fig. 7.10 shows the force per unit area distributions with respect to the radius at $t =$

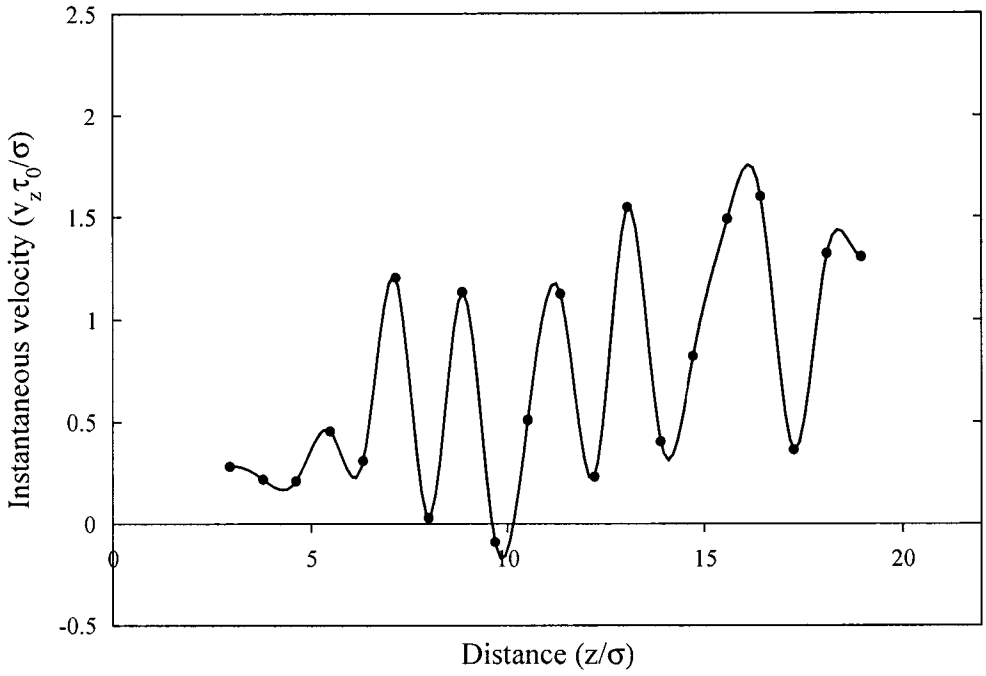

Figure 7.9: Space-averaged velocity distribution of adiabatic flow with high injection rate versus z at t=20 ps.

15, 20 and 30 ps. It can be seen that the three curves show the similar oscillatory pattern. When the front boundary moves at a constant velocity, the work that is input continuously into the system along the radial direction is, however, not uniform, but behaves in a wavelike pattern. This wavelike work input is one of reasons that result in an interesting phenomenon which transports liquid in a wavy manner within a nanometer syringe.

7.3 Summary

A pure molecular interaction flow with constant injection velocity at two different conditions, isothermal or adiabatic flow condition, was studied in a nanosyringe. The molecular dynamics simulation results show that the interaction

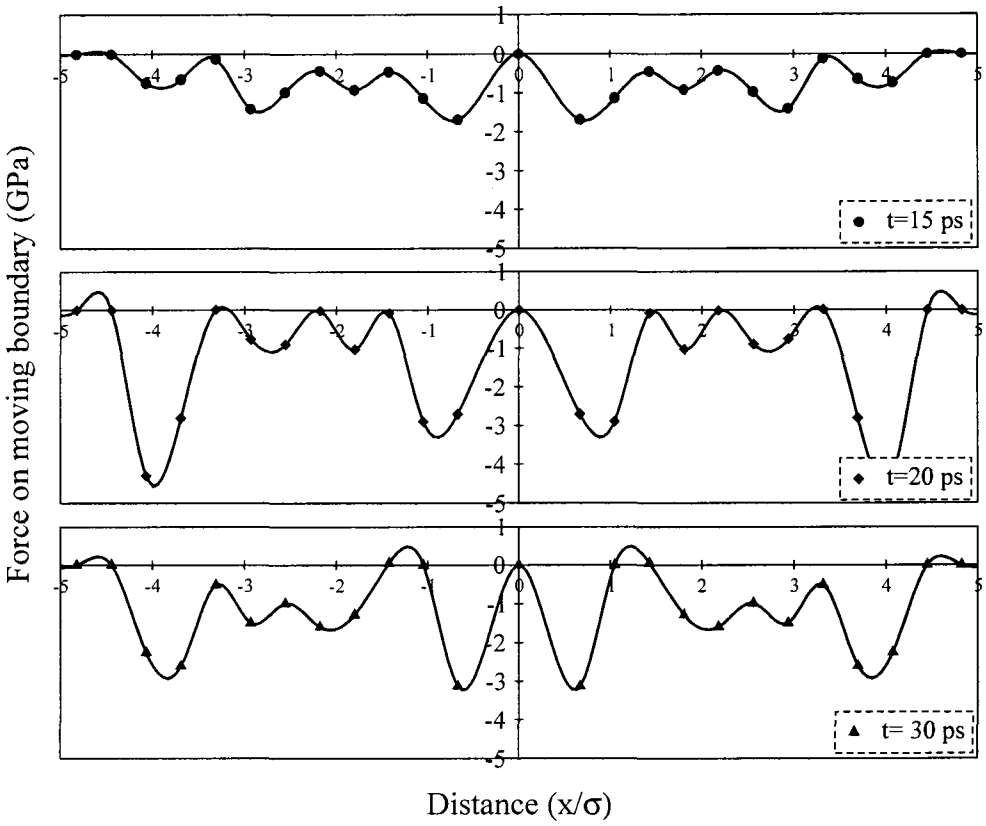

Figure 7.10: Force per unit area distribution on moving boundary with respect to radius at different stages.

between solid and liquid causes an oscillatory liquid density distribution in the normal wall direction for both isothermal condition and adiabatic condition. Their magnitudes of oscillations are different, especially for liquid molecules located at the central part of the channel. The streaming velocities for both isothermal and adiabatic conditions show that the first liquid layer stagnates with the solid substrate; the slip plate occurs at the interface between the first and second liquid layers, not at the solid-liquid interface. The radial distribution of steaming velocity deviates significantly from the parabolic profile predicted by continuum theory in macroscopic flow. Under a constant injection velocity

condition, it was found that liquid molecular transport in a nanoneedle has a wavelike motion which differs from that of bulk flow in macro-channels.

Chapter 8

Injection Flow in a NanoSyringe by Consideration of Extra-pair Positive/Negative Ions

8.1 Molecular Dynamics Simulation and Methodology

The geometry of interest in this chapter is similar to that shown in the previous chapter, but the size and formation of the nanosyringe are different (see Fig. 8.1). For the reservoir, the internal diameter and length are 5 nm and 3.4 nm, respectively. For the needle, the internal diameter and length are 2.9 nm and 7.4 nm, respectively. The solid substrate is made up of a total of 2,358 molecules in two layers, corresponding to the number density ρ_w of $0.915\sigma_w^{-3}$. For liquid, 3,665 molecules were packed in the reservoir and channel, corresponding to the number density ρ_l of $0.968\sigma_l^{-3}$. The molecular sizes for wall substrate and liquid are 0.37 nm and 0.316 nm, respectively. The injection velocity was $V_0 = 0.26\sigma_l/\tau_0$. The heat transfer between liquid in nanosyringe with environment was ignored due to transport time is limited, and the flow was simplified into an adiabatic flow.

The interactions between ion-ion, ion-liquid, ion-solid, liquid-liquid and liquid-

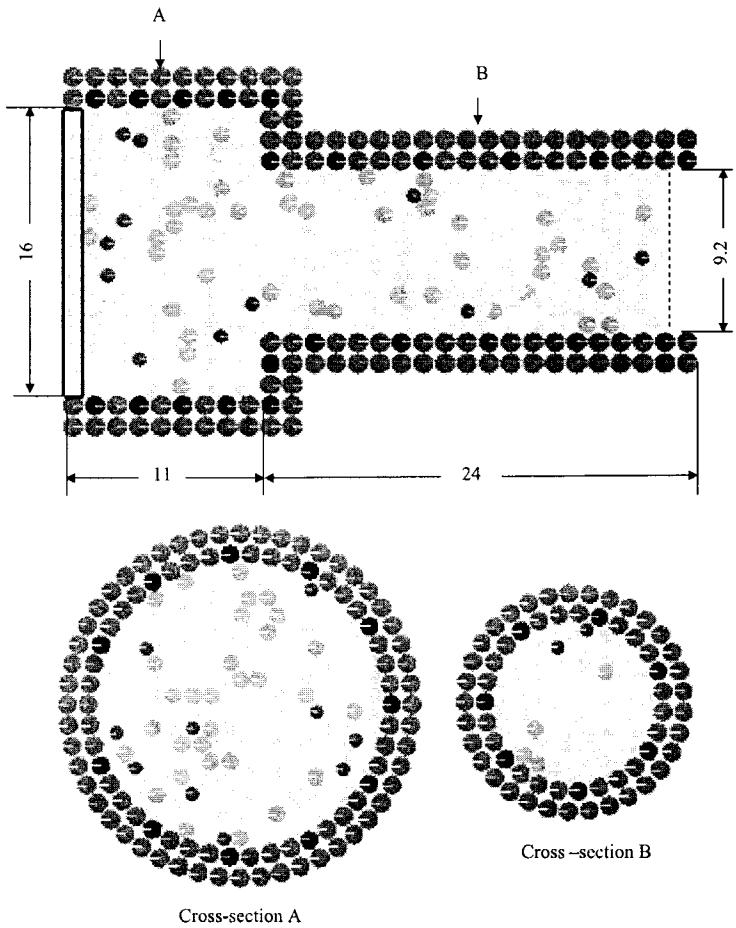

Figure 8.1: Geometry with molecular size and initial stage of liquid packed. (a) vertical-section passing through z axis, (b) cross-section of front reservoir and (c) cross- section of middle tube

solid molecules are governed by the Coulomb's law and Lennard-Jones potential. For Lennard-Jones potential, a truncation algorithm is used and the truncation distance is $2.2\sigma_{max}$, where σ_{max} is selected to be the largest value among the length scales of solid, liquid, liquid-solid and ion. For the Coulomb interaction, there is no truncation due to the small size of the device and no periodical boundary conditions used. The dielectric permittivity of vacuum used in the Coulomb equation was set to $8.854 \times 10^{-12} C^2/Nm^2$. Regarding the relative permittivity, it will be addressed later. The values of energy and length scales of liquid are $\epsilon_{ll} = 1.08 \times 10^{-21}$ J and $\sigma_{ll} = 0.316$ nm [50], respectively. For the length scales of positive and negative ions (e.g., H_3O^+ and HO^-), they are chosen as 0.32 nm and 0.281 nm approximately. The other parameters for positive/negative ions are the same to liquid's. For the charges on the solid substrate, Qian et al [84] chose the charge density on the channel wall either to be 0.12 C/m^2 or 0.32 C/m^2 in their simulations. In this study, 268 molecules with charge, -1.6×10^{-19} C, are distributed on the first solid substrate layer uniformly, which corresponds to the wall charge density of 0.245 C/m^2.

When ion distribution in liquid is dilute, the possibility of two ions meeting each other is small. The distance between them, comparing with liquid molecular size, is large, and the gap between them can be filled by liquid molecules. The relative permittivity of liquid chosen as 78 in this case is reasonable. But for high density of ions in liquid, the possibility of collision between two ions will be large. If two ions are separated by a gap less than a liquid molecule, obviously, interaction between two ions is same as the interaction of two ions in a vacuum because the gap between them can not be filled by any liquid molecules. To distinguish these two situations, a two-region model was proposed in this study, i.e. the relative permittivity is 1 if the gap between two ions is less than a liquid

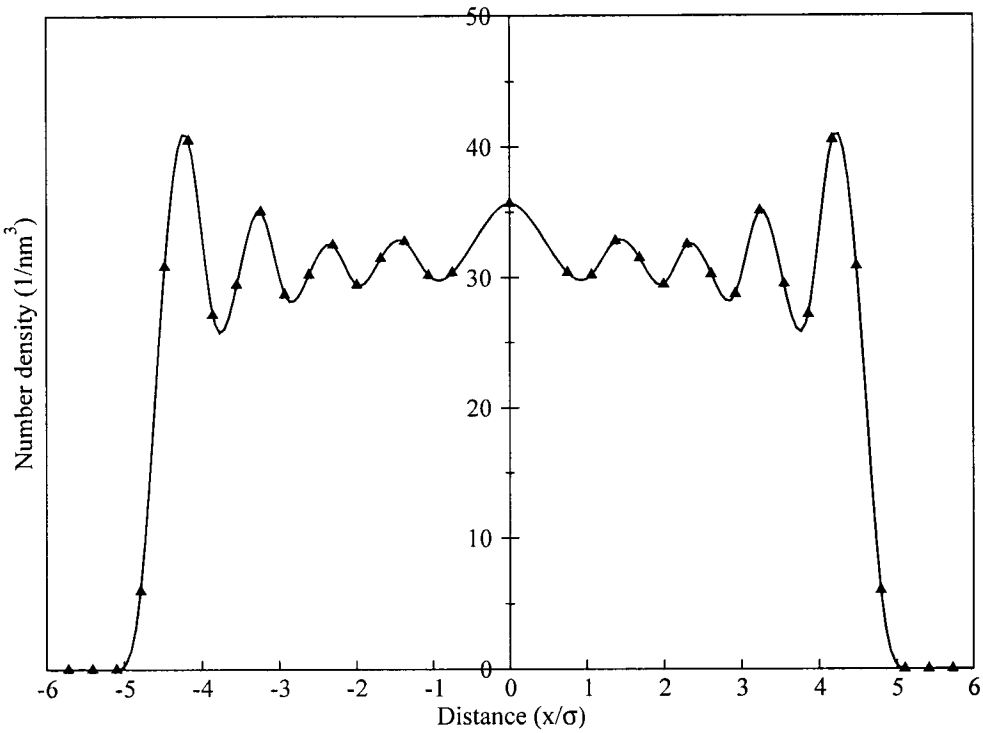

Figure 8.2: Liquid density distribution without ions in channel

molecular size, otherwise, it is 78.

8.2 Results and Discussion

In the study of the previous chapter, solid surfaces were not charged and liquid molecules were neutral. However, most solid substances are charged when they are brought into contact with an aqueous medium. In this chapter, four different cases for an injection flow in no-polar nanofluidics were considered, they were (1) fluid without ions, (2) only with counter ions, and counter-ions combined with (3) low concentration and (4) high concentration of extra-pair of positive/negative ions.

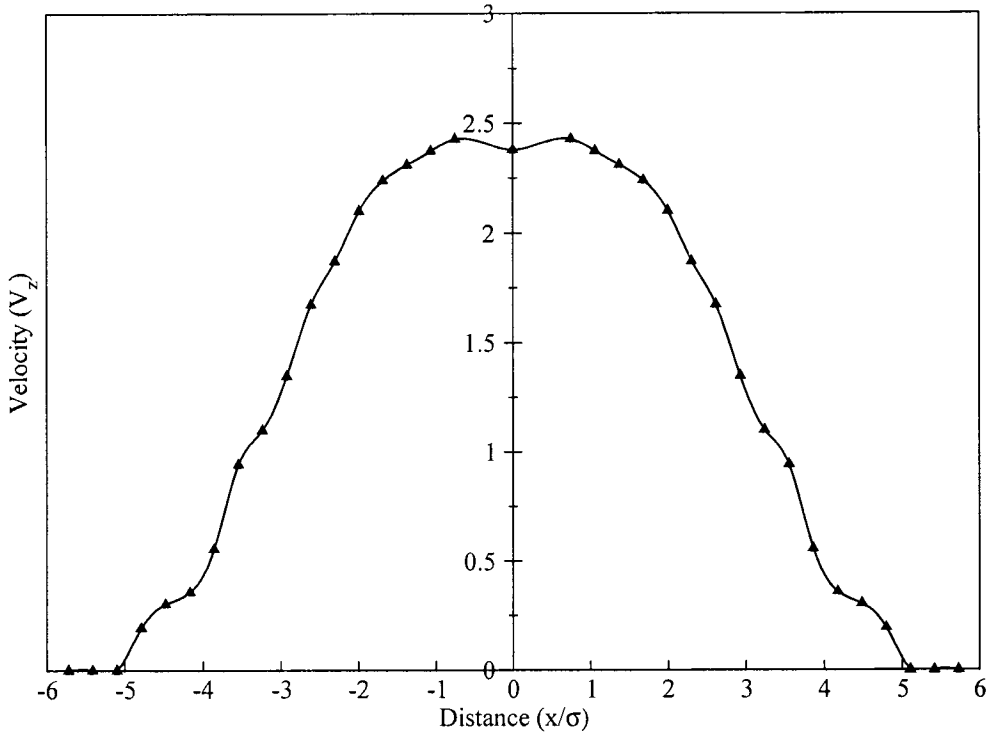

Figure 8.3: Time-averaged velocity and number density distributions at z=3.35 nm

8.2.1 Flow without Ions in Channel

Figs. 8.2 and 8.3 show the liquid density distribution and velocity profile in the radial direction. In Fig. 8.2, the density distributes in an oscillatory fashion, same pattern as that obtained in previous chapters. For the velocity distribution in Fig. 8.3, the main profile is a quasi-parabolic distribution in this channel with about 9.3 molecule diameters. If one observes it carefully and compares it with density distribution, he can find that the first liquid layer close to the solid wall moves or slips with a small velocity.

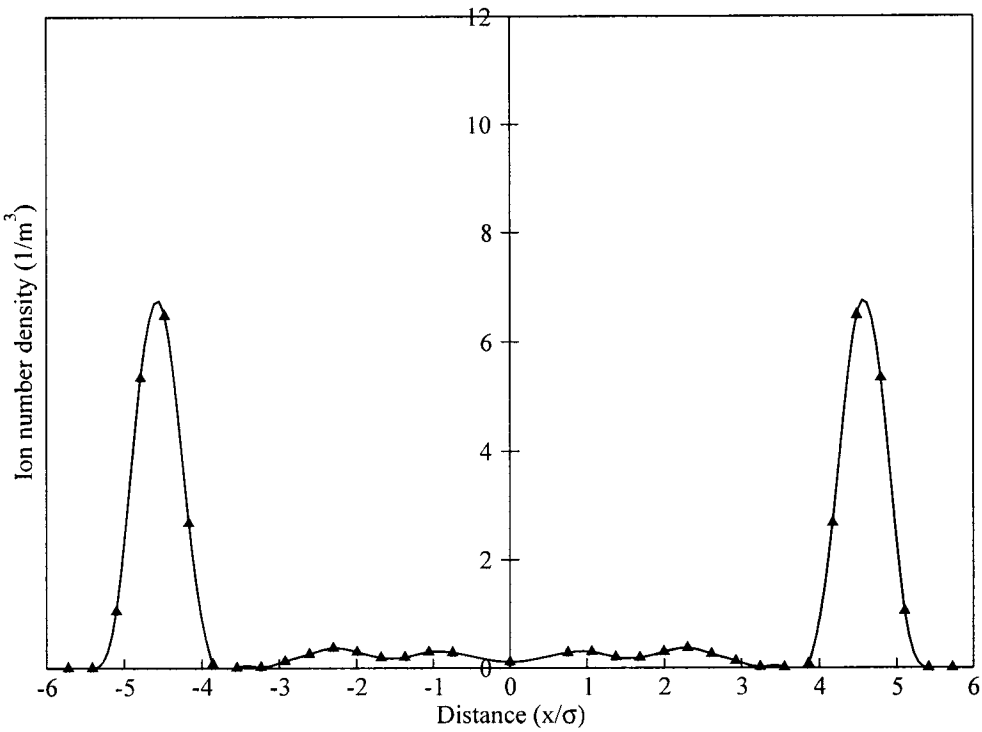

Figure 8.4: Ion distribution with only net charges in channel

8.2.2 Flow with Counter Ions in Channel

Ion distribution is very important in electrokinetic phenomena. To study ion distribution and its effect on liquid transport in this small nano device, only counter-ions are present in the channel, and the number of counter-ions in the liquid matches the number of charges presented on the solid wall. Fig. 8.4 shows the distribution of counter-ions in the middle section of the needle. The first characteristic in this picture is that there is a high ion density close to the solid substrate, implying that counter-ions are attracted by the charges on the wall and formed a Stern layer. In the central part of the channel, there are two small peaks, but their magnitudes are much small.

In Qian and Aluru's results [84], the ion distribution obtained by MD sim-

ulations does not monotonically decreases from the wall to the channel center. Actually, there is a very weak peak of ions which locates next to the highest peak of ions. After this weak peak, the ion distribution decreases smoothly in the direction from the wall to the channel center. Comparing the result shown in Fig. 8.4 with that of Qian and Aluru, the patterns between two results are similar, except that the second peak of ions (close to the highest peak) in this study is weaker than theirs and the distance between two peaks in Fig. 8.4 is larger than theirs. Analyzing these small differences between the results obtained by Qian and Aluru and those obtained in this study, the proposed reason is because the channel geometry, flow condition and relative permittivity in the two systems were different. Qian and Aluru also showed the ion distribution based on the Poisson-Boltzmann equation. They found that major difference between MD simulations and Poisson-Boltzmann equation occurs in the area close to wall. In other words, the Poisson-Boltzmann equation is not able to predict the ion distribution accurately in nanochannels. Fig. 8.5 gives the time-averaged velocity profile in this case. Comparing it with Fig. 8.3, the difference between them occurs at about $|x/\sigma_l| = 1.5 - 3$. This is the location where the second peak of ions is. In this system, each ion in liquid plays a role of retarding cell because of asymmetric in flow direction. So more ions will give the more resistance to liquid, which results in this phenomenon.

8.2.3 Flow with Counter-Ions and Low Concentration of Extra-Pair Positive/Negative Ions in Channel

In practice, the extra-pair positive/negative ions exist in a nanochannel with electrolyte solution if the solid wall is charged. This effect of extra-pair positive/negative ions has been neglected in the literature. Here, 132 pairs of

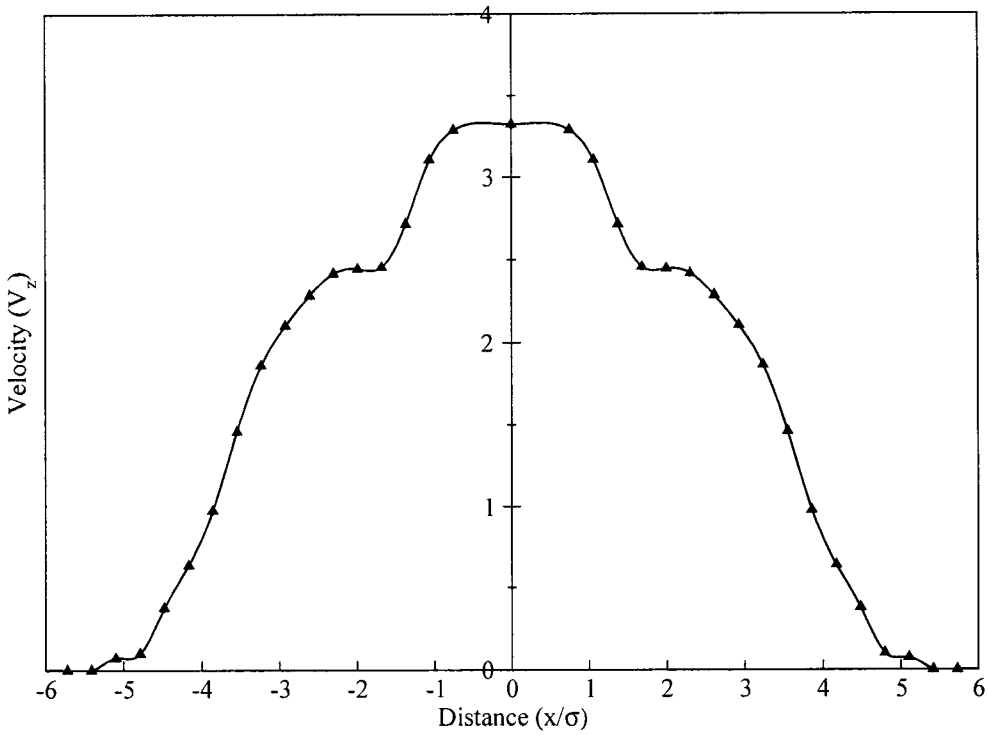

Figure 8.5: Time-averaged velocity distribution with only net charges in channel

positive/negative ions were added into the channel where the negative charges on solid wall still remain as what was used in case 2, i.e., 268 negative ions. Thus, the total positive and negative ions in the liquid phase is 400 and 132, respectively. The entire system remains electrically neutral. Fig. 8.6 shows the ion distributions of positive, negative and net charges. For the positive ions, the distribution in radial direction is same as the distribution from case 2. With respect to the negative ions, however, the distribution has a peak located at about 0.5σ away from the peak of positive ions. In the central part, the distribution is nearly flat. This distribution is different from what the Poisson-Boltzmann equation would predict, i.e., the density of negative ions smoothly increases in normal wall direction. For the net charges, the highest peak still locates at near

the wall. But after it, there is a deep valley which depends on the concentration of extra-pair positive/negative ions (see Figs. 8.6 and 8.8). Comparing it with the results in Fig 8.4, their profiles are significantly different. For these kinds of distributions, i.e., the peak of negative ions close to the highest peak of positive ions or the deep valley of net charges, the major reason comes from the extra interaction between positive and negative ions. When positive ions meet with negative ions, the Columbic force, i.e. attraction force, allows formation of groups which have only polarity or polarity plus net charges. For example, a group consisting of one positive ion and one negative ion has net zero charge with polarities at two ends. If a group is formed by more than two ions, the net charge and polarities depend on the numbers of positive and negative ions, and the structure of the group. When these groups are close to the wall, the negative charges on the wall force them to change their directions, i.e., the end with positive ions close to wall and the end with negative ions away from wall. That is why this phenomenon happens. From this result, it can be extracted that the extra-pair positive/negative ions in the liquid have a significant impact on ion distribution. If the concentration of ions in the liquid is high and extra-pair positive/negative ions exist, ignoring the effect of extra-pair positive and negative ions can cause significant errors.

Fig 8.7 shows the time-averaged velocity distribution in this case. the variation of the profile with respect to the radius at region $|x/\sigma_l| > 2$ is approximately a linear relation. As mentioned in case 2 of this subsection, each ion in this asymmetric system acts like a retarded cell. The area have more ions will have more resistance, if the number of positive and negative ions are summed in this region, the total number of positive and negative ions has an inverse relation with respect to the time-averaged velocity.

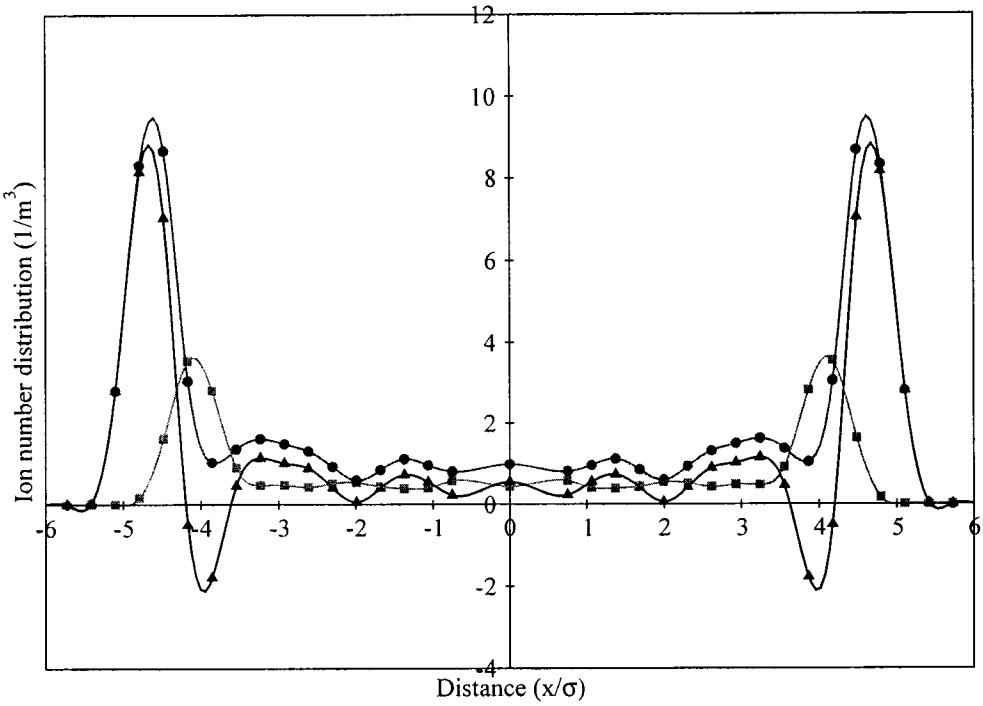

Figure 8.6: Ion distribution with net charges combining with low concentration of extra-pair positive/negative ions in channel. • positive ion, ■ negative ion and ▲ net charge

8.2.4 Flow with Counter-Ions and High Concentration of Extra-Pair Positive/Negative Ions in Channel

From case 3, one sees that the extra-pair positive/negative ions have a significant influence on ion distribution. To investigate the impact of concentration of extra-pair positive/negative ions on ion and velocity distributions theoretically (not physically), the number of extra-pair positive/negative ions were increased to 834. In this case, the charge on the solid wall are the same as cases 2 and 3, i.e., 268 negative charges on the wall and 268 positive ions in liquid. The entire system remains electrically neutral. Fig 8.8 gives the ion distributions of positive, negative and net charge. From this picture, one sees that the net

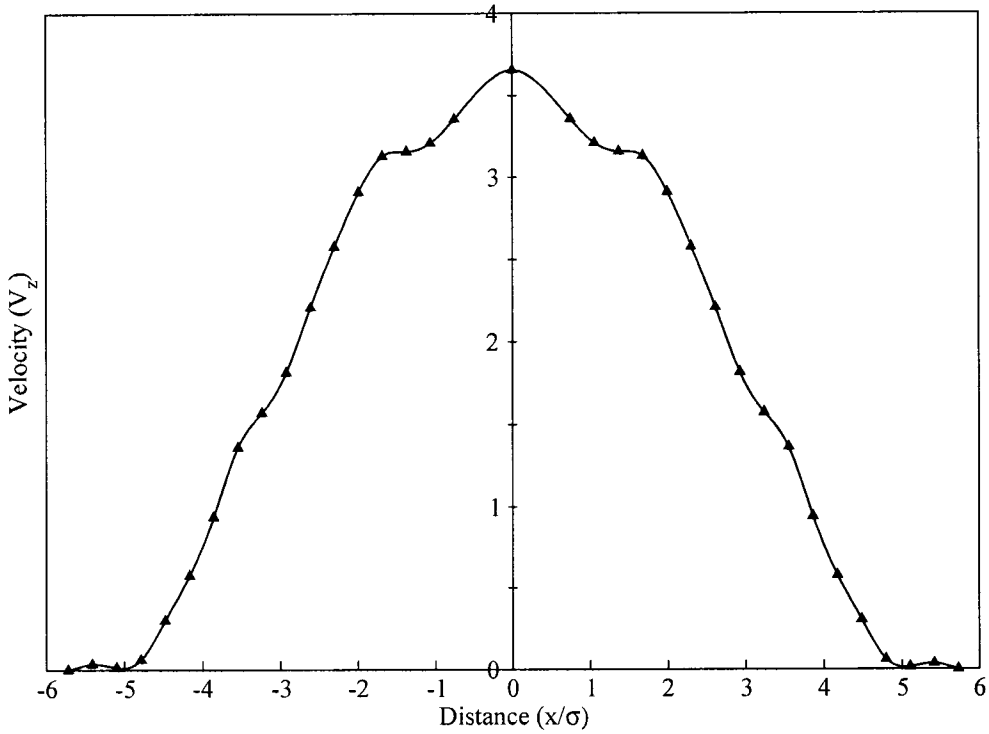

Figure 8.7: Time-averaged velocity distribution with net charges combining with low concentration of extra-pair positive/negative ions in channel

charge distribution is identical to the results shown in Fig 8.6. However, the values of the highest peak and deep valley have a small change, i.e., the value of the highest peak increases to 9.1 from 8.2 in case 3; the value of deep valley decreases to -3.6 from -1.9 in case 3. Another small difference for net charge distribution is the intensity of wave in central part where the effect becomes stronger than that from case 3. The distribution of positive and negative ions from outside to inside increase, except the first peak close to the wall and small central part. The time-averaged velocity distribution is shown in Fig 8.9. one sees that the flow is a plug-like flow. If the number of extra-pair positive/negative ions is small, the groups of positive and negative, formed by

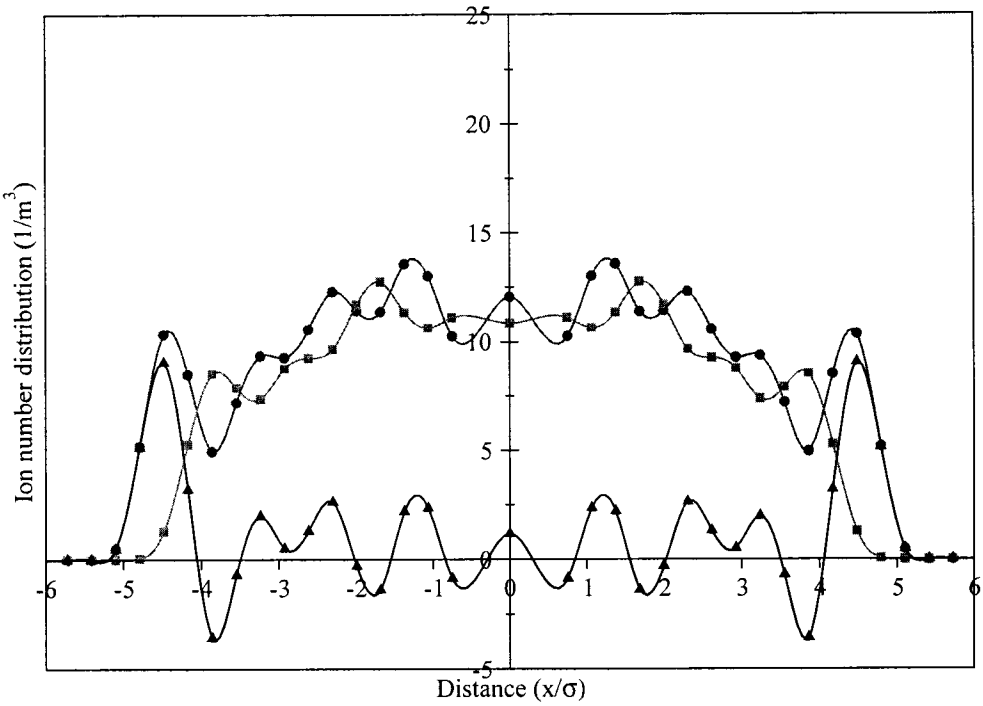

Figure 8.8: Ion distribution with net charges combining with high concentration of extra-pair positive/negative ions in channel. • positive ion, ■ negative ion and ▲ net charge

interactions between positive and negative, is limited as these groups distribute separately. When the number of extra-pair positive/negative ions increases to a critical value, these group of ions can influence each other. When one group moves, it affect all neighboring groups. From the results here, one sees high concentration of extra-pair positive/negative ions has small influence on net charge profile, but has a significant impact on the velocity distribution.

8.3 Summary

From this study, the following conclusions were obtained: (1) a quasi-parabolic velocity profile can be obtained in a 9.3σ needle of syringe when a constant

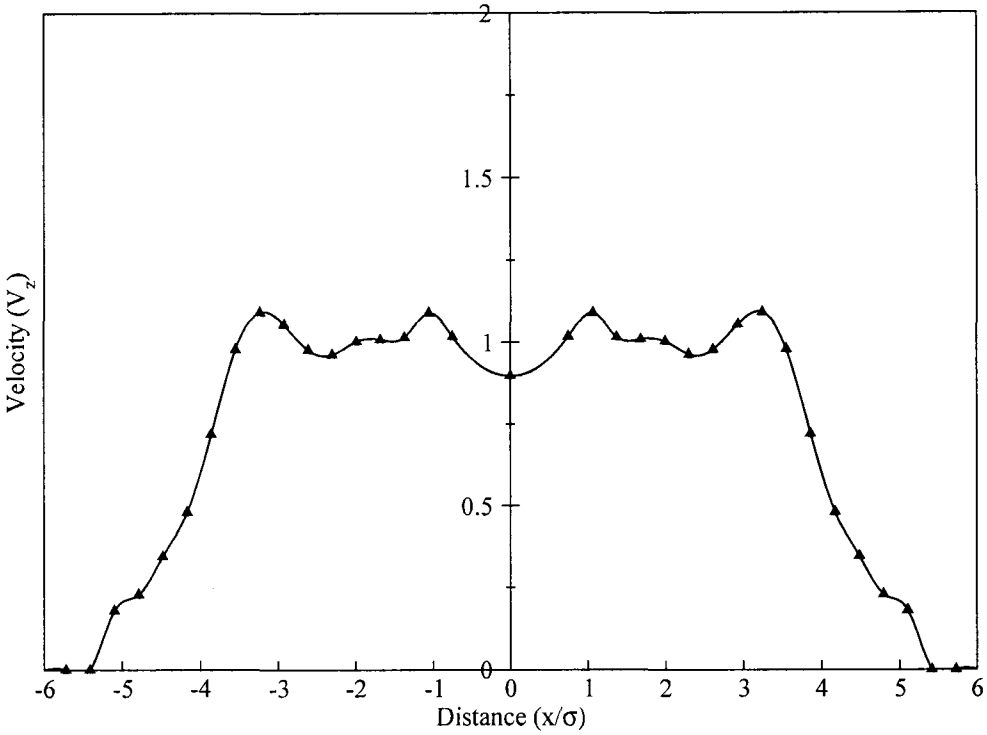

Figure 8.9: Time-averaged velocity distribution with net charges combining with high concentration of extra-pair positive/negative ions in channel

injection boundary condition is applied and no charges are presented in the channel; (2) the counter-ion distribution has a similar pattern with what obtained in nanochannel with periodic boundary condition if the extra-pair positive/negative ions are zero; (3) the extra-pair positive/negative ions have a significant influence on net charge distribution if they exit; (4) concentration of extra-pair positive/negative ions has a small effect on the pattern of net charge distribution, but has a stronger impact on velocity profile if the concentration of the extra-pair positive/negative ions is larger than a critical value.

CHAPTER 9

A NEW METHOD FOR MOLECULAR DYNAMICS SIMULATIONS IN THE ISOTHERMAL-ISOBARIC ENSEMBLE

9.1 Description of Methodology

At the microscopic scale, fluctuations of properties (e.g., instantaneous energy, pressure, etc.) are an intrinsic characteristic of a molecular system. At constant pressure, the volume of a system of N particles fluctuates. In this chapter, an alternative method to perform MD simulations in NPT ensembles is developed, which is much simpler than those used currently. The method was inspired by a physical phenomenon observed in macroscopic systems where a very thin, small and light weight plate becomes suspended in a fluid, and adopts almost the same motion as the fluid. If the size and weight of the plate are small enough, the motion of the plate can be used to approximate the local motion of the fluid. If one imagines this plate separating the fluid into two parts, then the fluid on one side can be removed and replaced by a pressure that is equal to the local liquid pressure. The motions of the plate and remaining fluid have little impact beyond the immediate vicinity of the plate. In the chapter, this idea was used to

create a N particle ensemble in which a constant pressure can be produced. As a result, fluctuations of instantaneous properties (e.g., volume and pressure) can be achieved automatically. Fig. 9.1 is a snapshot of the system studied in this work. In this figure, there are two physical boundaries (called auto-adjusting boundaries) in the z direction and periodic boundary conditions in the x and y directions. The formulism for the physical boundaries is same as that used in Chapter 4. To prevent the molecules in the domain from penetrating through the auto-adjusting boundaries to the outside, a large number density ($9/nm^2$) in each auto-adjusting boundary was used. The action of molecules outside the domain on the molecules in each auto-adjusting boundary was replaced by a uniformly distributed force, which was equivalent to the pressure produced by the local liquid. In the simulations, the motion of the molecules in each frame in the z direction depends on the the forces from both inside and outside of the domain. The force component in the z direction acting on each molecule in a frame is calculated by equation 3.1. This averaged force makes molecules in each auto-adjusting boundary have the same velocity in the z direction and prevents the frame from distorting if the molecules in each frame were set to the same initial location z_0 and velocity v_{z0}. Removing liquid molecules from one side of the auto-adjusting boundary has some influence on the liquid molecules which locate at the vicinity of the auto-adjusting boundary. To minimize this influence and the effect of the auto-adjusting boundaries on the results calculated, the volume used to collect data was chosen far away from the auto-adjusting boundaries and located in the middle in the z direction, as depicted by dash lines in Fig. 9.1.

The procedure for creating an NPT ensemble in this chapter was that two external pressures with the same value, P_{ext}, are exerted on the left and right

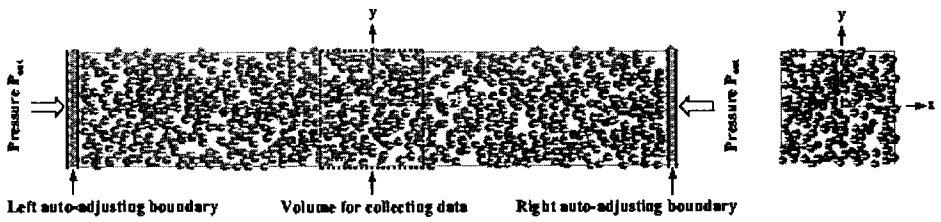

Figure 9.1: Snapshot of computational system with total 5150 molecules. (a) vertical section, (b) cross-section at the middle of the system.

auto-adjusting boundaries; then molecules in the whole system are allowed to move until thermodynamic equilibrium was reached. During this period, three thermostats were coupled to the left auto-adjusting boundary, the liquid in the domain and the right auto-adjusting boundary to adjust the temperature to reach the required value. Before data collection, the averaged momenta of the system in the three different directions were minimized. If the averaged momentum in the z direction was not zero, the whole system could shift with a constant velocity in the z direction. In this case, the molecular positions and velocities used in the Irving-Kirkwood equation (stress tensor) or in the Einstein equation (self-diffusion coefficient) could be peculiar values, i.e., the relative values in the coordinates moving with a constant velocity.

To examine the approach used in this chapter, liquid argon was chosen as a working medium. The Berendsen thermostats [89] were applied to control the temperature of the system to be $Tk_b/\varepsilon_l = 1.1$ ($T = 133\ K$). The pressure externally exerted on the auto-adjusting boundaries was set to 20 MPa. Under the above temperature and pressure, argon is in its liquid state. Two systems, one small (5,150 molecules) and the other large (10,406 molecules), were tested. The dimensions in the x and y directions for both systems were 4 nm. The

averaged distances between two auto-adjusting boundaries were about 19 nm for the small system and 39.2 nm for the large system. The objective of performing two different systems was to test the impact of the distances from the auto-adjusting boundaries to the volume used for data collection (4 nm in the z direction) on the results obtained from the data collection volume.

9.2 Results and Discussion

The objective of this study was to create an NPT ensemble. Two systems with different numbers of molecules were used to mainly examine whether the method proposed in this study is size dependent. In particular, we examined the spatial distributions of macroscopical properties (e.g., mean temperature, pressure and density), as well as the instantaneous features that exist in NPT ensembles, such as the relationship between volume fluctuations and number of liquid molecules and the probability distribution of the fluctuation of each property. Another purpose of performing two systems with different number of molecules is to test the impact of the distance from the auto-adjusting boundary to the data collection volume on MD simulation results. We compared the results obtained from two systems and found that the distance from the auto-adjusting boundary to the data collection volume used in this work had insignificant influence on the results obtained from the data collection volume. To illustrate how this method works, the small system with 5,150 molecules is chosen as an example.

Fig. 9.2 shows the three major statistical properties, density, temperature and pressure, obtained from the small system at different z positions. The volume used for collecting these data was a moving window that had a width of 2 nm in the z direction and 4 nm in the x and y directions. The sampling time for these data was 1 ns which was much larger than the characteristic time of

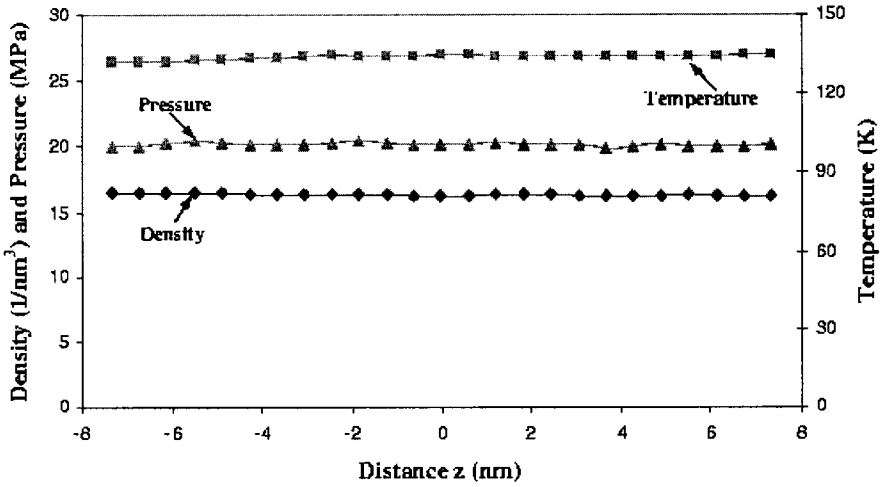

Figure 9.2: Distributions of temperature, density and pressure averaged over 1 ns versus the distance in the z direction.

the molecules, $O(1\text{ps})$. Therefore, these results represent the liquid macroscopic features. From this figure, one sees that the density, temperature and pressure distributions in the z direction were essentially uniform. One noteworthy feature in the figure is that the average pressure in the system, calculated by the Irving-Kirkwook equation, was almost equal to the external pressure exerted on the auto-adjusting boundaries. This characteristic is equivalent to what is usually observed in macroscopic systems, i.e., liquid pressure in a cylinder is equal to the pressure externally exerted on a piston if the effect of liquid density and the weight of the piston is negligible. This figure generally shows that an NPT ensemble can be created by the method proposed in this study. In the next part, we will demonstrate that this novel approach can automatically produce the fluctuations for instantaneous properties.

In NPT ensembles, the system volume fluctuates. The range of volume fluctuations is a function of the number of liquid molecules and is in the order of

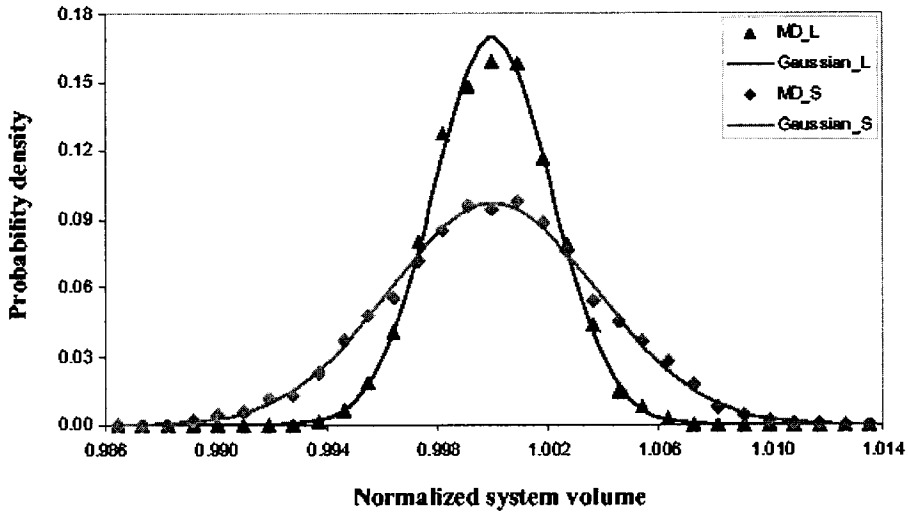

Figure 9.3: Comparison of the fluctuations of system volumes under two different size systems. Symbols and solid lines in the figure represent the fluctuations calculated using MD simulations and the Gaussian distributions with standard deviations obtained from fluctuations calculated by MD simulations.

$O(1/\sqrt{N})$, where N is the number of molecules in the system studied (in this work, N should be the number of liquid molecules between two auto-adjusting boundaries). Braga and Travis [100] studied the volume variation in NPT ensembles. Their results showed that the normalized volume fluctuated in a range of $0.95 \sim 1.05$ for a system with 100 particles, i.e., the range of volume fluctuations was about $\Delta V/V \approx 1/\sqrt{N}$, where V and ΔV are the volume and its fluctuation range. Fig. 9.3 shows the probability density distributions of two systems with respect to the normalized system volume in this study. In this figure, symbols (♦ – small system, ▲ – large system) and solid lines express the MD simulation results and the Gaussian distributions with standard deviations, respectively. Comparing the fluctuation range of normalized volume, one sees that the larger the system, the smaller the normalized volume fluctuates. To

examine the volume fluctuations created by the method proposed in this study satisfying the same relationship ($\Delta V/V \approx 1/\sqrt{N}$), the value of two standard deviations, calculated from the MD simulation data, was used as the volume fluctuation 'amplitude'. In this way, the total fluctuation range of the normalized system volume can be expressed by two times of 'amplitude' of fluctuations approximately. The MD simulation results show that $\Delta V/V \approx 1.52\%$ for small system and $\Delta V/V \approx 0.88\%$ for large system, respectively. For small and large systems, the values of $1/\sqrt{N}$ are 1.43% and 0.99%. Comparing the results predicted by MD simulations and those by the equation of $1/\sqrt{N}$, one sees that both of them are fairly consistent. This evidence means that the range of volume fluctuations produced by the method proposed in this paper is reasonable.

Fig. 9.4 displays the time evolutions of the momentum component in the z direction (a), kinetic energy (b), pressure (c), temperature (d), density (e) and system volume (f), respectively. The data shown in $(a) \sim (e)$ were collected from the data collection volume (shown by dash lines in Fig. 9.1) over a short period of 1 *ps*. The data in (f) was the volume defined by two auto-adjusting boundaries, and the time interval between two data points was 1 *ps*. A basic characteristic shown in Fig. 9.4 is that all instantaneous properties fluctuate around their means. However, the frequencies shown in this figure are different, i.e., the first three [(a), (b) and (c)] elucidate the similar pattern of fluctuations which have the highest frequency among the properties collected, after that, the frequency shown in (d), (e) and (f) in the figure decreases. The reason for this phenomenon is that each property collected from the data collection volume has different averaging processes. For the first three, i.e., momentum in z direction (a), kinetic energy (b) and pressure (c), they were calculated by the equation of $\bar{y} = [\sum_i^M \sum_j^{N(i)} y_j]/M$, in which $\bar{y}$ is an average property collected

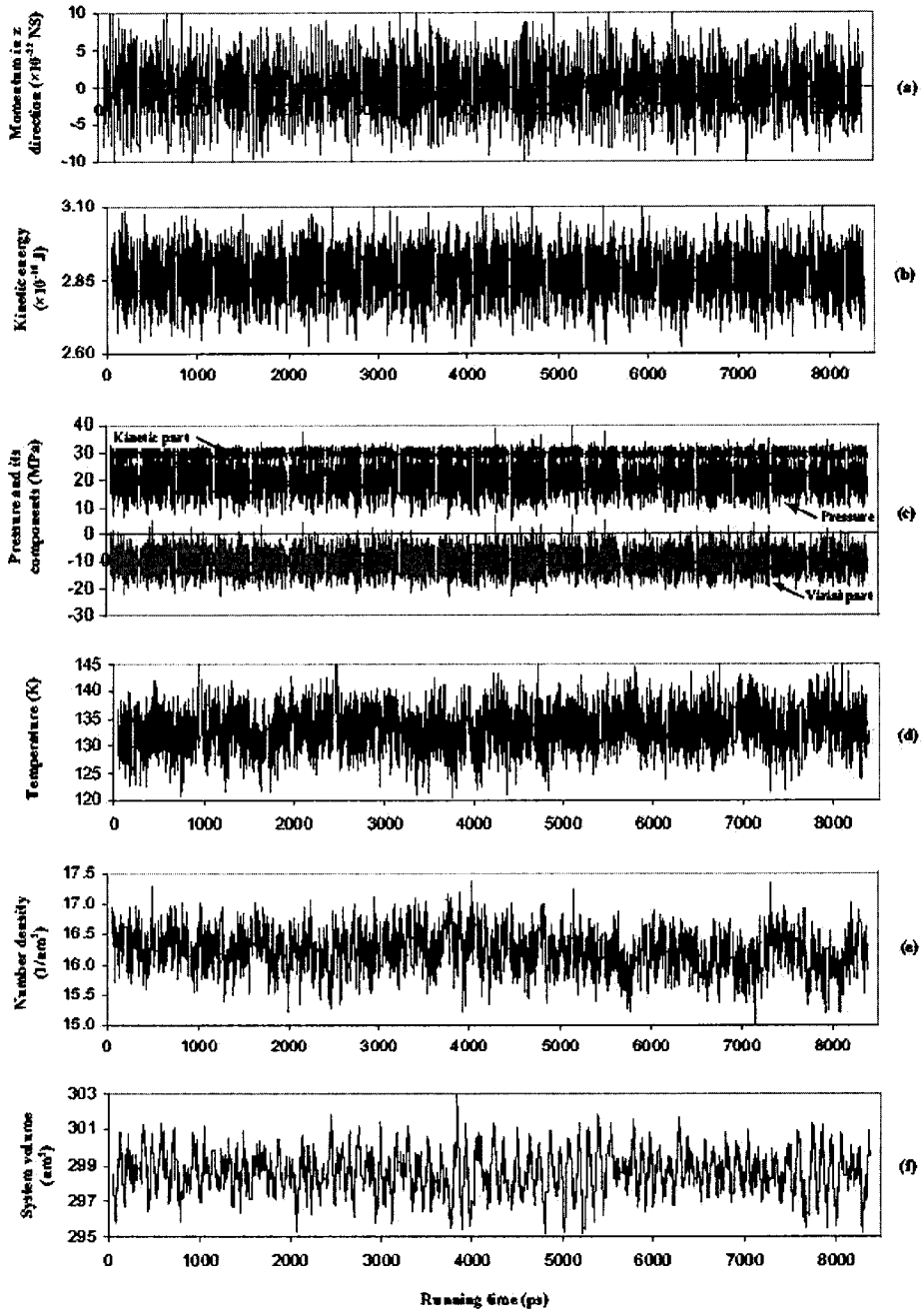

Figure 9.4: Time evolutions of momentum in the z direction (a), kinetic energy (b), pressure with its two contributions (c) and system volume formed by two auto-adjusting boundaries (d).

from the data collection volume over a short period; i is the i^{th} iteration and M is total iterations over the period in which data is collected; $N(i)$ is the number of molecules in the data collection volume at the i^{th} iteration; y_j is the instantaneous property of the j^{th} molecule collected from the data collection volume, for example, $y_j = m_j v_{jz}$ for calculating momentum in z direction, where m_j and v_{jz} are the mass and velocity component in z direction of the j^{th} molecule. This equation indicates that the property $\bar{y}$ depends not only on variable y_j but also on the molecule number $N(i)$ collected from the data collection volume at each iteration. Meanwhile, the iteration number M (or time interval) impacts the frequency of $\bar{y}$. For time traced temperature (d), it was calculated from the equation of $\bar{T} = \{\sum_i^M [\frac{1}{3k_b N(i)} \sum_j^{N(i)} m_j v_j^2]\}/M$. Comparing it with the equation used to calculate the momentum etc., the term in the brackets in this equation actually expresses an average value, which reduces the freedoms of this equation. The time evolution of density displayed in (e) was obtained by the relationship of $\bar{\rho} = [\sum_i^M \rho(i)]/M$. This relationship shows that the average density mainly depends on the instantaneous density $\rho(i)$ at the i^{th} iteration, while the iteration number M also influences the density distribution. For time traced system volume (f), it had the lowest frequency because the system volume in simulations only depends on the iteration or running time, i.e., $V = A \cdot L(i)$, where A is the cross-section area and $L(i)$ is the distance defined by two auto-adjusting boundaries at the i^{th} iteration. In addition, the size and weight of the auto-adjusting boundaries may influence the frequency of system volume fluctuations. Besides the frequency of fluctuations depends on the freedoms of the calculation equation, there are other points which should be noted. One sees that the mean momentum in the z direction, presented by a dash line in (a) of the figure, was $-2.15 \times 10^{-24}\ N \cdot s$. This value, which is practically equal

to zero, guaranteed that the whole system in calculation did not shift in the z direction, which was proved by checking the time traces of positions of two auto-adjusting boundaries. Fig. 9.4 (c) displays three instantaneous values, i.e., total pressure and its two components (the kinetic part and virial part). Both components fluctuate, but the amplitudes of them are different, i.e., the amplitude of virial part was much larger than that of the kinetic part. It is noted that the fluctuations of the total pressure are actually dominated by the variation of virial part. To examine the system volume fluctuation created by the method proposed in this work, the time trace of the system volume is displayed in (f) of Fig. 9.4. From this figure, it should be note that the characteristic of the system volume fluctuations in the NPT ensemble has been successfully reproduced by this novel method.

DeVane et al. [138] studied the volume fluctuations in NPT ensembles. They indicated that the fluctuations of observable quantities from their means, obtained from MD simulations, are typically Gaussian. To examine the fluctuations shown in Fig. 9.4 meeting the Gaussian distributions, the histograms of the z-component of the momentum, kinetic energy, pressure, temperature, number density and system volume are plotted in (a), (b), (c), (d), (e) and (f) in Fig. 9.5, respectively. The probability distribution functions for all of instantaneous properties exhibit a similar pattern. To check the difference between the nature of these distributions, a Gaussian distribution (with a standard deviation calculated from the fluctuations shown in Fig. 9.4) is superimposed in (a), (b), (c) (d), (e) and (f) in Fig. 9.5, respectively. One sees that the probability densities obtained statistically from fluctuations shown in Fig. 9.4 are consistent with the Gaussian distribution, which implies that the fluctuations created by the method proposed in this study are reasonable and reliable. To compare

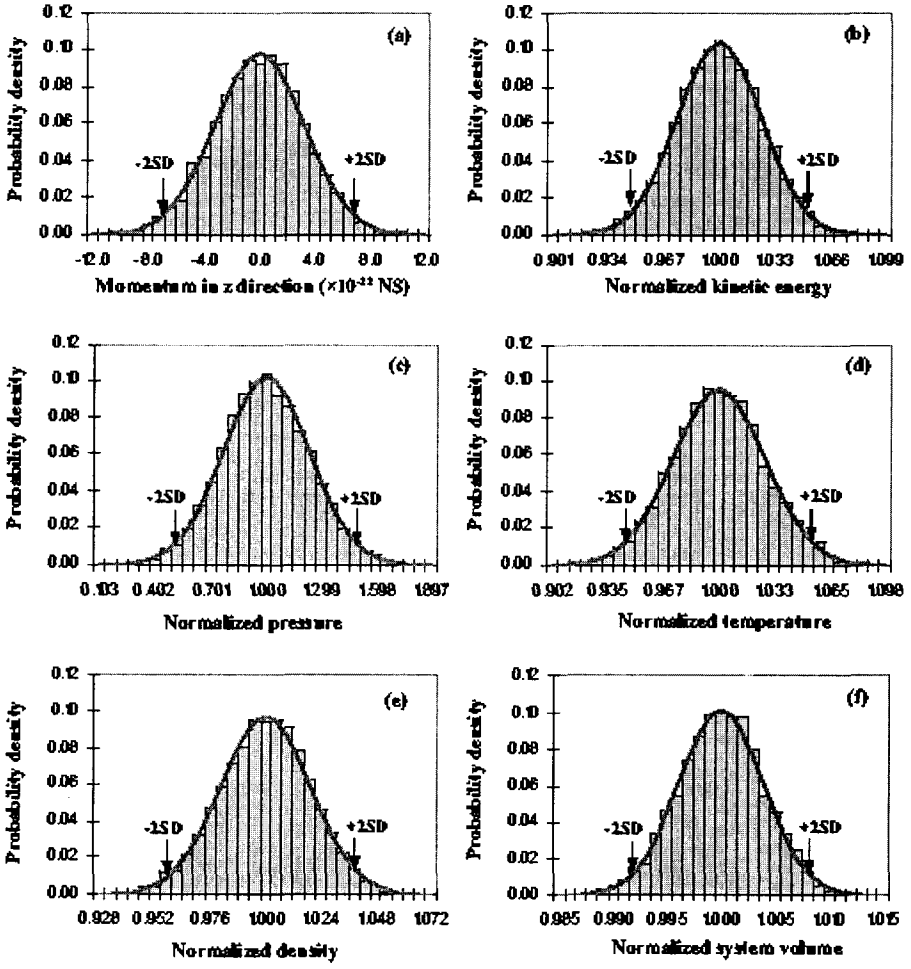

Figure 9.5: Histograms of fluctuations of the z-component momentum (a), kinetic energy (b), pressure (c) and system volume (d) and superimposed Gaussian distributions with standard deviations calculated from fluctuations shown in Fig. 9.4.

the amplitudes of fluctuations for different properties (except for momentum), two times of standard deviation ($2SD$) was used as the fluctuation 'amplitude'. From (b), (c), (d), (e) and (f) in Fig. 9.5, we see that the normalized amplitudes of fluctuations, $|(x_{2SD} - \overline{x})/\overline{x}|$ (where $\overline{x}$ and x_{2SD} are the mean value and the value at $2SD$), are about 5% for kinetic energy, 5.4% for temperature, 46% for pressure, 3.9% for density and 0.76% for system volume, respectively. Comparing these 'amplitudes', one sees that a small fluctuation of the system volume can cause a large change of pressure. This result is reasonable for a liquid with small compressibility. To further examine the reliability of the method proposed here, the compressibility of liquid argon, calculated by the following equation

$$\kappa = \frac{-1}{V}(\frac{\partial V}{\partial P})_T = \frac{1}{\rho}(\frac{\partial \rho}{\partial P})_T \approx \frac{1}{\bar{\rho}}(\frac{\Delta \rho_{SD}}{\Delta P_{SD}})_T \tag{9.1}$$

where ρ and $\bar{\rho}$ are the density and its mean; $\Delta\rho_{SD}$ and ΔP_{SD} are the standard deviations of the density and pressure. The MD results calculated by the above equation along with the use of the data obtained from the data collection volume are $4.20 \times 10^{-9}\ m^2/N$ for the small system and $4.12 \times 10^{-9}\ m^2/N$ for the large system. The experimental result [139] is $4.53 \times 10^{-9}\ m^2/N$ (under the condition of $T = 136\ K$ and $P = 23.7\ MPa$). Comparing MD simulation results with experimental value, One sees that they are agreeable, which further proves that the method proposed in this study works well and is reliable.

In the present study, the Berendsen thermostats were applied to demonstrate how this method works. In practice, different thermostats can be used to control the temperature in an NPT ensemble because the pressure controlled by this approach is independent of the thermostats applied.

In summary, the method proposed in this paper was examined in terms of

creating the spatial distributions of macroscopical properties (e.g., mean density, temperature and pressure), instantaneous features (i.e., fluctuations of each property, the variation range of volume fluctuations and the probability density distributions of all fluctuations) and comparison of compressibility between MD simulation results and experimental value. MD simulations results elucidate that this novel method not only produced spatially uniform distributions of temperature, density and pressure, but also created the reasonable fluctuations for each property. The fluctuations of all properties satisfied the Gaussian distributions. The fluctuation range of the normalized system volume had an order of $O(1/\sqrt{N})$. The compressibility predicted by MD simulations was consistent with the experimental value. All of above evidences indicate that the method proposed in this study works well, and it can be used to perform MD simulations in NPT ensembles.

9.3 Summary

A novel method was proposed to perform MD simulations in the NPT ensemble. The key feature of this approach was that a constant pressure and the fluctuations of the system volume in the NPT ensemble were produced automatically by two auto-adjusting boundaries. The method, compared with others used currently, is simpler and robust due to the fact that no extra freedoms are introduced into the system.

Chapter 10

Role of Attractive Force in Molecular Dynamics Simulation

10.1 Description of Methodology

The equation of state of a fluid in a macroscopic scale gives the relationship among the temperature, pressure and density. If two of them are fixed, the other will be determined uniquely. To examine the effect of the attractive force (expressed by cutoff distance) in MD simulations on the equation of state, a Lennard-Jones fluid (i.e., liquid argon) at a state of temperature $T = 133\ K$ and pressure $P = 20\ MPa$ was chosen. Experimental measurement [140] shows that the density of liquid argon at this state is $1.19\ g/cm^3$, which corresponds to the number density $\rho_n = 17.93/nm^3$ or the reduced density $\rho_n\sigma^3 = 0.708$, where σ is the length scale of liquid. Two ensembles (NVT and NPT) were applied in this study.

For the NVT ensemble, $7,733$ argon molecules were placed in a cube subjected to periodical boundary conditions in all directions. The average number density of molecules in the cube was set to be the experimental value. The procedure for creating an NVT ensemble was that the molecules were packed

in a cube randomly. The initial velocities with a Maxwellian distribution were signed to them, which corresponded to the system having average temperature $T = 133\ K$. Then the thermostat was coupled and the molecules in the system were allowed to move until the thermodynamic equilibrium was reached. After that, the average properties of the fluid were obtained by collecting data over a period of 0.5 ns.

For the NPT ensemble, MD simulations were calculated based on a technique used in the previous chapter. The major feature of this method is that the pressure in the NPT ensemble is maintained by two auto-adjusting boundaries on which two external forces/pressures with the same value are exerted. This method has been validated to work well in terms of creating spatially uniform mean temperature, pressure and density while still allowing appropriate levels of temporal fluctuations in these quantities, as well as fluctuations in system volume. The procedure for creating an NPT ensemble in the present study is that two external pressures ($P_{ext} = 20\ MPa$) were exerted on two auto-adjusting boundaries. These boundaries adjusted their positions automatically according to the force acting on them. If the force coming from the molecules in the system is smaller than the external force, the fluid in the system are pressed, otherwise expanded. Three thermostats were coupled to the left auto-adjusting boundary, the liquid in the domain and the right auto-adjusting boundary to adjust the temperature to reach the required value. Before data collection, an initial field for each case was well prepared so that the mass center of the system only vibrated around its initial position but not shift. For all MD simulations in the NPT ensemble, 10,406 molecules were used. The dimensions in the cross direction were $4 \times 4\ nm^2$. The averaged distances between two auto-adjusting boundaries varied as the attractive force changed. The average properties ob-

tained in this ensemble were collected over a period of 1 ns.

Temperature control was achieved by coupling thermostat(s) in the system. Two different thermostats, Berendsen [89] and Nose-Hoover thermostats, were coupled in a test system to examine their effects on the results, respectively. The averaged results obtained by these two different thermostats showed quantify on thermodynamic properties of the liquid. Therefore, the less computationally demanding Berendsen thermostat was chosen to control temperature in this work.

10.2 Molecular Dynamics Simulation

The interaction between two molecules is modeled by a truncated and shifted Lennard-Jones 12-6 potential expressed by equation 3.2. In this study, different cutoff distances were used to capture the effect of the attractive force on the equilibrium structure and thermodynamic properties of the liquid. If the potential is truncated at $r_c = 2^{1/6}\sigma = 1.1225\sigma$, only the repulsive force is considered. In this case, the equation 3.2 expresses the WCA potential. If $r_c \geq 2^{1/6}\sigma$, the increasing proportions of attractive force is taken into account. In the literature published, the cutoff distance that is most commonly used in MD simulations is $r_c = 2.5\ \sigma$ [25, 34, 40, 113, 141]. While other cutoff distances, for example, $r_c = 2.2\sigma$ [33, 35], 3σ [54] and 5σ [55], were used by different authors. In this chapter, ten different cutoff distances ($r_c = 2^{1/6}$ to 5.8σ) were used to systematically study the impact of the attractive force on fluid thermodynamic properties in two different ensembles. The length and energy scales of argon used in the simulations were $\sigma = 0.3405\ nm$ and $\varepsilon = 1.67 \times 10^{-21}$ J, respectively.

The equations of motion were integrated using a Velocity Verlet algorithm. The time step in simulations was 0.5 fs. The stress tensor was calculated by the

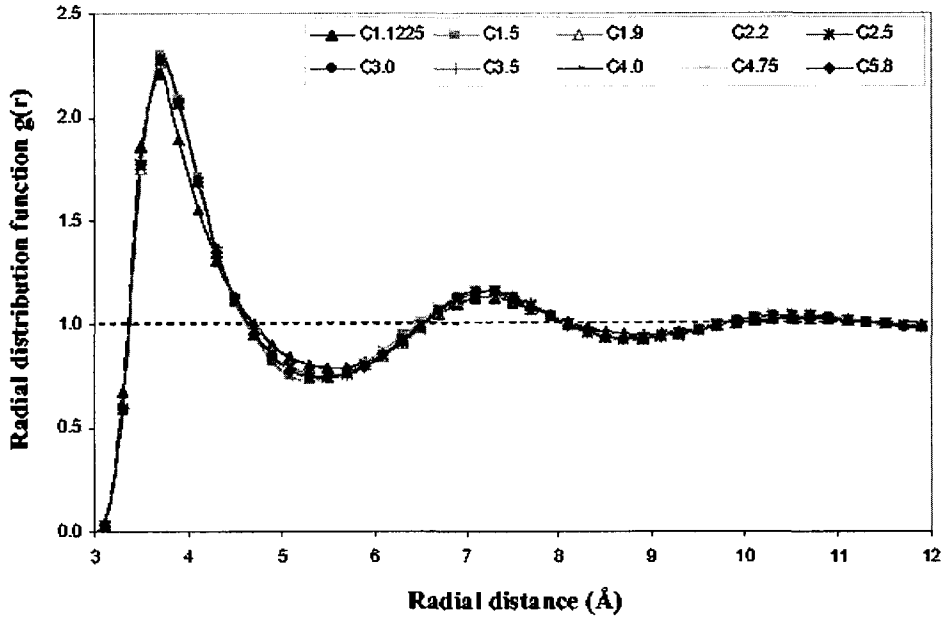

Figure 10.1: Comparison of radial distribution functions obtained using different cutoff distances in a NVT ensemble at temperature $T = 133\ K$ and reduced density $\rho_n\sigma^3 = 0.708$.

Irving-Kirkwood equation, and the constitutive pressure was defined as minus one third of the trace of the stress tensor. The self-diffusion constant were calculated by using both Green-Kubo relationship and Einstein equation.

10.3 Results and Discussion

10.3.1 Canonical (NVT) Ensemble

For an NVT ensemble at high density, the WCA theory has shown that the attractive force has little impact on the equilibrium structure of Lennard-Jones liquids. In this thesis, ten MD simulations using the same NVT conditions, while the different cutoff distances ($r_c = 2^{1/6} = 1.1225$, 1.5, 1.9, 2.2, 2.5, 3, 3.5,

4, 4.75 and 5.8 σ), were performed to examine the effect of the attractive force on liquid structure and thermodynamic properties. Fig. 10.1 shows the radial distribution function $g(r)$ of liquid argon obtained using different truncation distances. In this figure, the curve with symbols ▲ is $g_0(r)$ obtained by the pure repulsive force (or WCA potential), while others are the results calculated by the combination of repulsive and partial attractive forces. Comparing the curves plotted in this figure, one sees that $g(r)$ are essentially the same if the attractive force, even partially, was taken into account in MD simulations. $g_0(r)$ produced by the pure repulsive force exhibit identical pattern to other $g(r)$, while a slight difference exists. Weeks et al. [106] studied the effect of density on $g(r)$. They found that the agreement between $g_0(r)$ and $g(r)$ (obtained at a cutoff distance $r_c = 2.5\sigma$) was excellent at high density ($\rho_n\sigma^3 = 0.85$), while the poor agreement between $g_0(r)$ and $g(r)$ was observed at moderate density ($\rho_n\sigma^3 = 0.5$). These two results imply that the agreement between $g_0(r)$ and $g(r)$ decreases as the density decreases. In this work, the reduced density is $\rho_n\sigma^3 = 0.708$, a slight difference between $g_0(r)$ and $g(r)$ is consistent with the results shown by Weeks et al. in reference [106].

The Einstein equation and the Green-Kubo relationship were applied to calculate the self-diffusion coefficient of liquid argon at the fixed state, respectively. Fig. 10.2 and its insets show the MD simulation results. The insets (a) and (b) in Fig. 10.2 exhibit the variations of the mean square displacements and the self-diffusion coefficients calculated by Green-Kubo relationship versus the integrating time by using different cutoff distances. In these two insets, one sees that the MD results are almost same, except for that obtained by applying the pure repulsive force or WCA potential. The self-diffusion coefficients, corresponding to the data shown in two insets, are exhibited in Fig. 10.2 by symbols

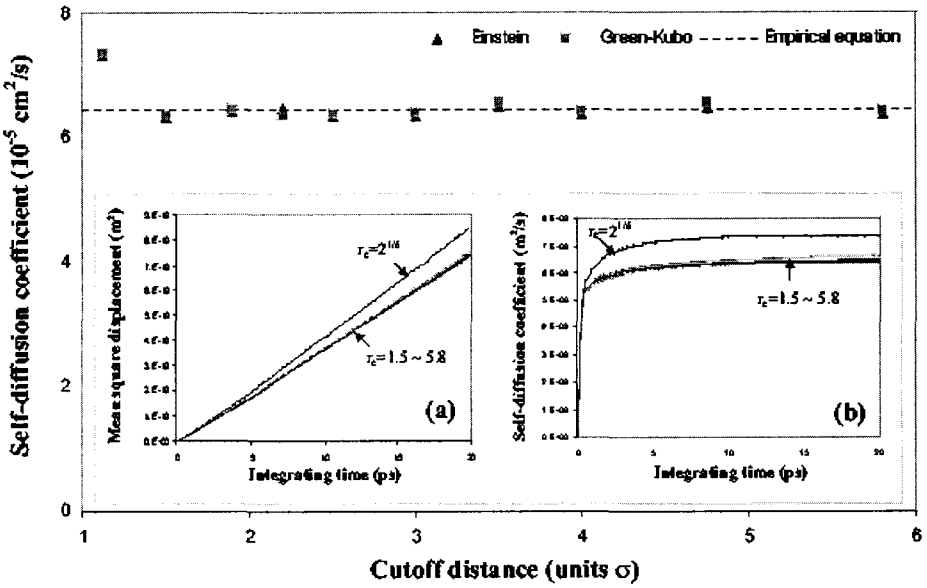

Figure 10.2: Comparison of self-diffusion coefficients calculated by Einstein equation, Green-Kubo relationship and the empirical equation proposed by Naghizadeh and Rice in a NVT ensemble at temperature $T = 133\ K$ and reduced density $\rho_n\sigma^3 = 0.708$.

▲ (Einstein equation) and ■ (Green-Kubo relationship). The results shown by symbol ▲ were obtained by using the slope of the mean square displacement between integrating time 8 and 18 *ps*; the results shown by symbol ■ were the average values over integrating time 10 to 20 *ps*. The dash line in the figure expresses the values obtained by the empirical equation which was extracted from the experimental data by Naghizadeh and Rice [142]. One sees that the self-diffusion constants calculated by the Einstein equation and Green-Kubo relationship agree well in the whole range of cutoff distance used. Comparing the self-diffusion coefficients calculated by MD simulations with that obtained by the empirical equation, the agreement between them is fairly good except for the value calculated by only considering repulsive force. The self-diffusion con-

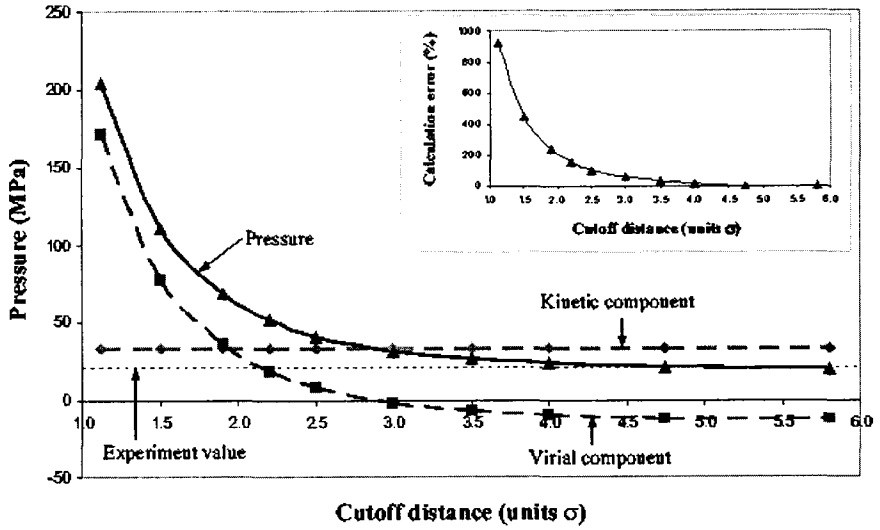

Figure 10.3: Comparison of pressures between experimental value (conducted by Jain and Nanda) and MD simulation results obtained at different cutoff distances in a NVT ensemble at temperature $T = 133\ K$ and reduced density $\rho_n\sigma^3 = 0.708$. The dash lines with symbols ♦ and ■ in the figure are two components (kinetic and virial parts) of pressure, respectively. The inset of the figure shows the simulation error of pressure versus the cutoff distance.

stant obtained by only accounting for the repulsive force is slightly higher than the value calculated by using the empirical equation. The difference between them is about 13.6%.

Figs. 10.1 and 10.2 shows that ignoring the attractive force in the NVT ensemble at a density $\rho_n\sigma^3 = 0.708$ has essentially no significant impact on the equilibrium structure and self-diffusion constant of liquid argon at the chosen state. So ignoring effects of the attractive force in an NVT ensemble at a high density, for example $\rho_n\sigma^3 \geq 0.708$, is a wise choice for calculating the radial distribution function and self-diffusion constant. However, ignoring the attractive force will impact other properties. To demonstrate this point, pressures in the NVT ensemble at the above described conditions were calculated by ac-

counting for the effect of attractive force. Fig. 10.3 shows the variations of pressure and its two components, kinetic and virial parts, with respect to the cutoff distance. In this figure, the long dash lines with the symbols ♦ and ■, the solid line with symbols ▲ and the short dash line without symbols represent the kinetic component, virial component, total pressure and experimental value [140], respectively. The kinetic component is near constant due to the fact that temperature and density in NVT ensemble are fixed. But the virial component varies significantly with the cutoff distance used and it dominates the variation of the total pressure. One sees that pressure calculated by only considering the pure repulsive force or WCA potential ($r_c = 2^{1/6}\sigma$) substantially deviates from the real pressure. While as the cutoff distance increases, the difference between the simulation result and the experimental value decreases. The inset of Fig. 10.3 shows the MD simulation error, $|P_{MD} - P_{real}|/P_{real}$, using different cutoff distances. Ignoring the effect of attractive force on pressure results in a simulation error of slightly over 900% (note: the contribution of the attractive force on the pressure calculation in the WCA theory [106] has actually been accounted for by integrating the radial distribution function from zero to infinite). Another value that should be noted is the simulation error at the cutoff distance $r_c = 2.5\sigma$ that is commonly adopted in MD simulations by many researchers. The error calculated at this truncation is about 104%, which means that the cutoff distance commonly used in MD simulations in NVT ensembles can predict the liquid equilibrium structure and self-diffusion constant properly, while can not predict the liquid pressure correctly. To obtain more accurate pressure in MD simulations, a larger cutoff distance should be used. According to Fig. 10.3, to obtain a simulation error for pressure less than 2%, a cutoff distance $r_c \geq 4.75\sigma$ should be used.

10.3.2 Isothermal-Isobaric (NPT) Ensemble

In the previous subsection, the effect of the attractive force on fluid properties in an NVT ensemble at high density were discussed. The MD simulation results show that the attractive force has no significant influence on the liquid structure and self-diffusion coefficient, but substantially impacts the corresponding pressure. Actually, a fluid structure and self-diffusion constant mainly depend on the fluid density, temperature and local free volume, while these parameters in an NVT ensemble at high density are nearly constant. In the following section, a different ensemble (NPT) at the same liquid state, i.e., $T = 133\ K$, $P = 20\ MPa$ and $\rho\sigma^3 = 0.708$, was applied to study the role of the attractive force in MD simulations.

Fig. 10.4 and its inset show the variations of density and pressure with respect to the cutoff distance used in the NPT ensemble at the aforementioned condition. The inset of Fig. 10.4 shows the total pressure and its two components at different truncation distances. One sees that the two components of pressure vary with opposite trends, i.e., kinetic part increases while virial part decreases, as the cutoff distance increases. However, the sum of them (total pressure) stags a constant (20 MPa). The effect of the attractive force on the density is shown by the solid line with symbols ▲ in Fig. 10.4. The dash line in this figure is the experimental value [140]. From this figure, it is noted that the attractive force significantly impact the density of the system. When only accounting for the repulsive force ($r_c = 2^{1/6}\sigma$), the density calculated by MD simulation is much lower than the real value at this state, which means that MD simulations in an NPT ensemble can not model a real liquid state if the attractive force is ignored. As the cutoff distance increases, density increases quickly before a specific cutoff value, e.g., $r_c < 3\sigma$. After that, density increases

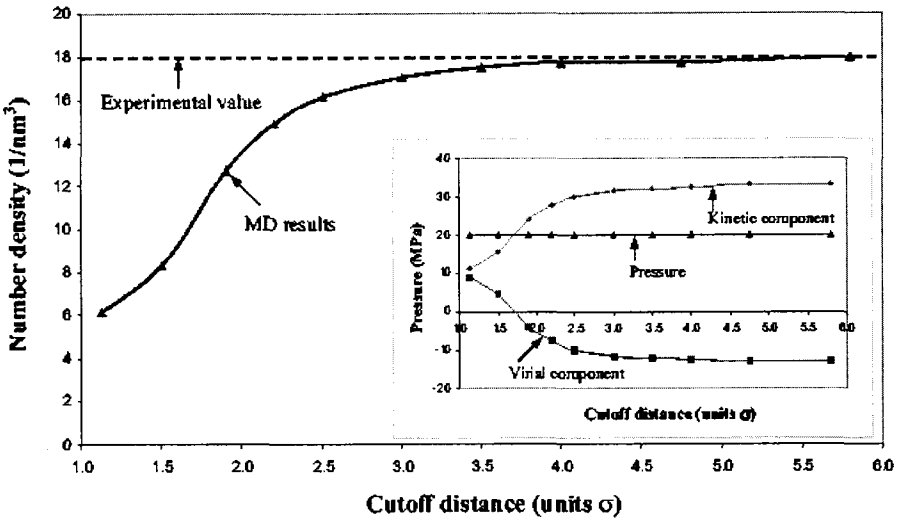

Figure 10.4: Comparison of densities between experimental value (conducted by Jain and Nanda) and MD simulation results obtained at different cutoff distances in a NPT ensemble at temperature $T = 133\ K$ and pressure $P = 20\ MPa$. The inset of the figure is the distributions of pressure and its two components versus the cutoff distance obtained in the NPT ensemble at the same temperature and pressure.

slightly and approaches to a constant value. Comparing with the experimental value, density calculated by MD simulation at $r_c = 2.5\sigma$ is lower than real value about 10%. If one wants to get more accurate density result, a larger cutoff distance should be applied, e.g., $r_c \geq 4\sigma$ resulting in the density error $\leq 2\%$.

Fig. 10.5 displays the equilibrium structure of liquid argon simulated using NPT ensemble along with different cutoff distances. In contract to the radial distribution function obtained in the NVT ensemble, the radial distribution function in the NPT ensemble strongly depends on the cutoff distance. It should be noted that the curves in this figure show three distinguished features. When $r_c = 2^{1/6}\sigma$ or the attractive force is ignored, the radial distribution function displays gas-like characteristics. When $r_c \geq 1.9\sigma$, all of curves show the same

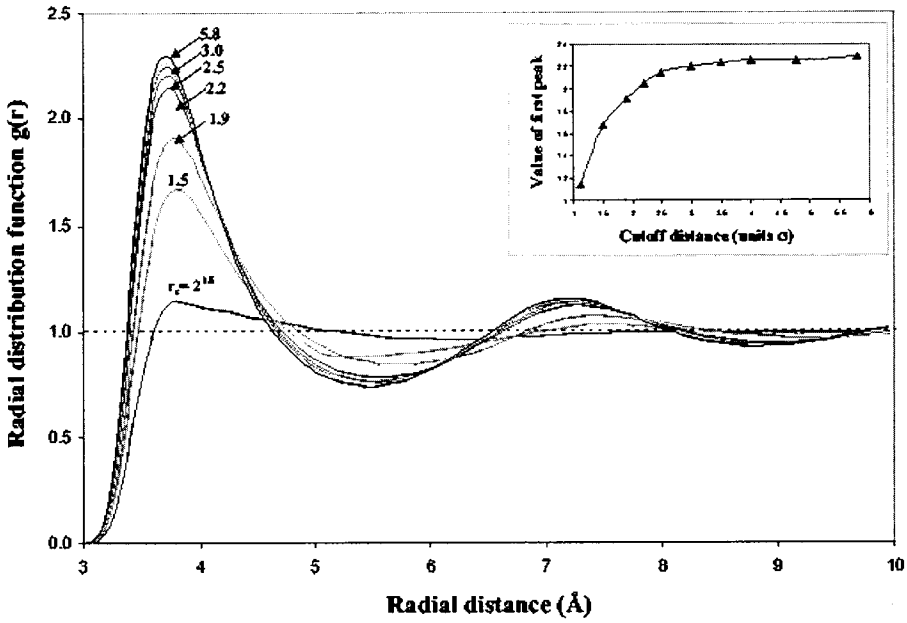

Figure 10.5: Comparison of radial distribution functions obtained under different cutoff distances in an NPT ensemble at temperature $T = 133\ K$ and pressure $P = 20\ MPa$. The inset of the figure exhibits the relationship between first peak value of radial distribution function and cutoff distance.

pattern as that is observed in the x-ray experimental measurement of the liquid argon [129, 130]. The radial distribution function at $r_c = 1.5\sigma$ shows a slightly different pattern, i.e., the radial distribution function gradually declines from the first peak until the radial distance about 5 $\mathring{A}$. After that it increases near linearly over the range of radial distance $5 - 6.5\ \mathring{A}$. If the value of the first peak of the radial distribution function is taken as a characteristic to measure the effect of cutoff distance on the equilibrium structure, as shown in the inset of the figure, one sees that the radial distribution function increases quickly when $r_c \leq 2.5\sigma$. After that, it increases slightly and tends to a constant as the cutoff distance increases.

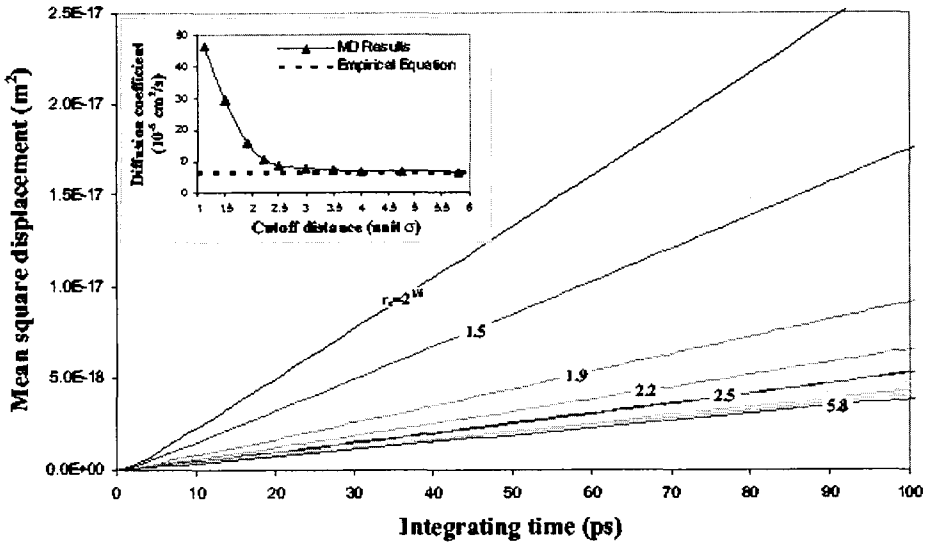

Figure 10.6: Comparison of mean square displacements obtained under different cutoff distances in an NPT ensemble at temperature $T = 133\ K$ and pressure $P = 20\ MPa$. The inset of the figure is the comparison of self-diffusion coefficients between the MD simulation results and the value calculated by using empirical equation proposed by Naghizadeh and Rice.

The Fig. 10.6 shows the mean square displacements with respect to the integrating time. One sees that a shorter cutoff distance corresponds on a larger mean square displacement. The variation of the mean square displacement deceases as the cutoff distance increases. The self-diffusion coefficient calculated from the data shown in this figure was plotted in the inset of Fig. 10.6. In this inset, the solid line with symbols ▲ is the MD simulation result; the dashed line is the value calculated by using the empirical equation [142]. One sees that the difference between the results calculated using MD simulations and the empirical equation at small cutoff distance is large, while as the cutoff distance increases, the difference between two results diminishes. If the value calculated using the empirical equation is taken as the 'real value', the simulation errors

at different cutoff distances are 630% at $r_c = 1.1225\sigma$, 40% at $r_c = 2.5\sigma$ and $< 10\%$ for $r_c > 4\sigma$, respectively.

In summary, the attractive force in MD simulations plays a role on determining liquid structure and thermodynamic properties, in particular in NPT ensembles. If attractive force is taken into account properly in the MD simulations, the results obtained in the two different ensembles will be the same and consistent with the corresponding experimental values or those calculated by using empirical equations. Ignoring the effect of the attractive force will results in incorrect answer, e.g., the pressure calculated in NVT ensembles and density in NPT ensembles.

10.4 Summary

The role of the attractive force in molecular dynamics simulation at high density is studied systematically in canonical (NVT) and isothermal-isobaric (NPT) ensembles using equilibrium molecular dynamics simulations. Results show that the attractive force in NVT ensembles plays little role in determining the equilibrium structure and self-diffusion coefficient, while it influences essentially on the pressure calculation. The attractive force in NPT ensembles impacts not only on the equilibrium structure, but also on the thermodynamic properties. To predict all properties of Lennard-Jones liquids correctly, the effect of the attractive force in MD simulations has to be taken into account properly, for example, to yield correct properties ($< 5\%$ errors), a long cutoff distance (4.5σ) should be used.

Chapter 11

Summary and Future Work

11.1 Summary

In this thesis, fundamental study of fluid transport through two nano devices, finite length nanopore (membrane) and nanosyringe, was carried out by using a novel pressure-driven NEMD method and an injection approach, respectively. The novel pressure-driven NEMD method has been successfully extended to study fluid properties in NPT ensembles. The following conclusions were extracted from the work performed in this thesis:

1. A novel pressure-driven NEMD approach was developed in this thesis. The advantages of this method, relative to the DCV-GCMD method that is commonly used, are that it eliminates disruptions to the system dynamics that are normally created by inserting or deleting particles from the control volumes, and that it is easy to implement for dense systems.

2. Solid wall-liquid interaction has a significant impact on the liquid transport in a finite length nanopore. In particular, the weak solid wall-liquid interaction causes liquid slipping on the solid wall, while strong interaction promotes sticking at the wall. The flow rate calculated by NEMD

simulations, subjected to a constant pressure drop across the channel, depends on the solid-liquid interaction and is proportional to the ratio of $\varepsilon_l/\varepsilon_{ls}$ for the system studied.

3. The effect of the entrance and exit on liquid transport through a nanopore depends on the solid wall-liquid interaction. The weaker the solid wall-liquid interaction, the stronger the entrance and exit effect.

4. A comparative study between continuum and atomistic approaches shows that the classical N-S equations with no-slip boundary conditions at the walls can be used to approximately predict liquid transportation through a finite length nanopore only under the condition of having a neutral-like solid wall-liquid interaction ($\varepsilon_s = \varepsilon_l$).

5. An unexpected wavelike liquid transport motion in the nanosyringe is elucidated by performing the NEMD simulation under constant injection condition, which differs from the motion of bulk flow in macro-channels.

6. The extra-pair positive/negative ions have a significant influence on both fluid transportation and charge distributions in the nanosyringe.

7. The NEMD pressure-driven method extended to perform EMD simulations in the NPT ensemble successfully generates uniformly spacial distributions of thermodynamic properties and instantaneous fluctuations. The method proposed in the thesis, compared with others used currently, is simpler and robust due to the fact that no extra degrees of freedoms are introduced into the system.

8. The study of the role of the attractive force /cutoff distance in MD simulations elucidates that the attractive force in NVT ensembles plays little

role in determining the equilibrium structure and self-diffusion coefficient, while influences essentially on the pressure calculation. The attractive force in NPT ensembles impacts not only on the equilibrium structure, but also on the thermodynamic properties. To predict all properties of Lennard-Jones liquids correctly, a larger cutoff distance (e.g., 4.5σ) should be used in MD simulations.

11.2 Future Work

With the successful development of the novel molecular dynamics method in this thesis, future studies on the following topics could be interesting and beneficial:

1. *Study of pure diffusion between two species materials driven by only chemical potential or density difference*

   Diffusivity, a transport property, plays an important role in many natural processes. Currently, there are several NEMD methods that have been used to study such processes, e.g., force field-driven NEMD simulation, DCV-GCMD method, etc. In these algorithms, the pressure and chemical potential (or density) differences between two reservoirs are set up simultaneously. Therefore, the diffusivity obtained by using these methods consists of two parts, i.e., a convection part from pressure difference and a diffusion part from chemical potential difference. There exists little work on diffusivity generated by a pure chemical potential difference (zero pressure difference) up to now. The method proposed in this thesis can easily overcome the problem (pressure and chemical potential difference existing simultaneously) in force field-driven NEMD simulation and DCV-GCMD algorithm. Work that will be carried out include the bulk

diffusion between two species separated by a sharp interface and the diffusion through a membrane. The chemical potential will be controlled by changing energy scale, molecular size or both of them.

2. *Transport of suspending DNA or polymer molecules in a solvent through a finite length nanopore*

   A DNA or polymer molecule moving through a nanopore faces a large entropic barrier. In order to overcome this barrier and pass through the pore, an external field or interaction is needed. For a DNA or polymer molecule transported through a finite length nanopore, many researchers [5, 7–10, 13, 14] contributed by using electrical fields or interaction between chain/pore. But in these studies, only DAN or polymer molecules (no solvent molecules) passed through nanochannels. For transport phenomenon of DNA or polymer molecules suspended in a solvent through a finite length nanopore, there is little study. The method proposed in this thesis can be applied to mimic a suspending DNA or polymer molecule in a solvent transport through a nanopore by using an electrical field or a combination of electrical and pressure fields.

3. *Electrokinetic nanochannel battery*

   Electrokinetic microchannel battery, a safe, non-polluting, completely renewable method of producing electric power, created by Dr. Kostiuk and Dr. Kwok's research group at the University of Alberta in 2003. This method converts the hydrostatic pressure directly into electrical current, i.e., pressure-driven flow in a microchannel induces a streaming current due to the presence of an electrical double layer (EDL) in the interface between the electrolyte solution and channel wall. In this method, the

channel size, concentration of ions and structure of EDL are important. Yang et al [21] pointed out that the streaming current in a microchannel is on the order of a nano-ampere and is additive. Therefore, increasing the number of channels per unit cross area should be an efficient method to improve the efficiency of the battery. If the channel size decreases from micro order to nano order, the number of channels on per unit area will increase 3 orders of magnitude. But as the size of the channel decreases, the flow properties in the nanochannel will be significantly different from those in the microchannel. Therefore, studying liquid transport, ion migration and EDL structure in the nanochannel for improving the properties of electrokinetic nanochannel battery is needed. Due to technology limitations, conducting experimental measurements in such small channels is still rather difficult at present. MD simulation could be applied as the first step to exploit the flow transport, ion migration and EDL structure in such nano-sized battery.

As potential algorithms, the methods proposed in this thesis can be used to study these suggested topics. However, there are many technical challenges ahead. For example, modeling DNA molecules and calculating long range electrical forces in this type of systems is challenging. Therefore, in order to use these methods, further research work will be needed.

BIBLIOGRAPHY

[1] J. Eijkel and A. Berg, Microfluidics Nanofluidics **1**, 249 (2005).

[2] B. J. Alder and T. E. Wainwright, J. Chem. Phys. **31**, 459 (1959).

[3] B. J. Alder and T. E. Wainwright, J. Chem. Phys. **31**, 459 (1959).

[4] R. Komanduri and L. M. Raff, Proc. Instn. Mech. Engrs **215 Part B**, B12600 (2001).

[5] S. E. Henrickson, M. Misakian, B. Robertson, and J. Kasianowicz, Phys. Rev. Lett. **85**, 3057 (2000).

[6] M. Muthukumar, Phys. Rev. Lett. **86**, 3188 (2001).

[7] E. A. Marzio and J. J. Kasianowicz, J. Chem. Phys. **117**, 4063 (2002).

[8] W. Sung and P. J. Park, Phys. Rev. Lett. **77**, 783 (1996).

[9] E. Slonkina and A. B. Kolomeisky, J. Chem. Phys. **118**, 7112 (2003).

[10] M. Akeson, D. Branton, J. J. Kasianowicz, E. Brandin, and D. W. Deamer, Biophys. J. **77**, 3227 (1999).

[11] C. Dellago, M. M. Naor, and G. Hummer, Phys. Rev. Lett. **90**, 105902 (2003).

[12] I. Szabo, G. Bathori, F. Tombola, M. Brini, A. Coppola, and M. Zoratti, J. Biological Chemistry **272**, 25275 (1997).

[13] I.-C. Yeh and G. Hummer, Proc. Natl. Acad. Sci. USA **101**, 12177 (2004).

[14] A. Aksimentiev, J. B. Heng, G. Timp, and K. Schulten, Biophys. J. **87**, 2086 (2004).

[15] J. J. Kasianowicz, E. Brandin, D. Branton, and D. W. Deamer, Proc. Natl. Acad. Sci. USA **93**, 13770 (1996).

[16] J. Hummer, J. C. Rasalah, and J. P. Nowaryta, Nature **414**, 188 (2001).

[17] M. Moseler and U. Landman, Science **289**, 1165 (2000).

[18] A. Meller, L. Nivon, E. Brandin, J. Golovchenko, and D. Branton, Proc. Natl. Acad. Sci. USA **97**, 1079 (2000).

[19] Q. Zhang, J. Zheng, A. Shevade, L. Zhang, S. H. Gehrke, G. S. Heffelfinger, and S. Jiang, J. Chem. Phys. **117**, 808 (2002).

[20] P. Keblinski, W. Ma, A. Maritan, J. Koplik, and J. R. Banavar, Phys. Rev. E. **47**, R2265 (1993).

[21] J. Yang, F. Lu, L. W. Kostiuk, and D. Y. Kwok, J. Micromech. MicroEng **13**, 963 (2003).

[22] R. Allen and J. P. Hansen, J. Chem. Phys. **119**, 3905 (2003).

[23] G. E. Karniadakis and A. Beskok, *Micro Flows: Fundamentals and Simulation* (Springer, New York, 2002).

[24] K. P. Travis, B. D. Todd, and D. J. Evans, Phys. Rev. E **55**, 4288 (1997).

[25] K. P. Travis and K. Gubbins, J. Chem. Phys. **112**, 1984 (2000).

[26] J. Dzubiella, R. J. Allen, and J. P. Hansen, J. Phys. Chem. **120**, 5001 (2004).

[27] G. S. Heffelfinger and F. Swol, J. Chem. Phys. **100**, 7548 (1994).

[28] J. M. D. MacElroy, J. Chem. Phys. **101**, 5274 (1994).

[29] F. Zhu, E. Tajkhorshid, and K. Schulten, Biophys. J. **83**, 154 (2002).

[30] O. Jepps and S. K. Bhatia, J. Chem. Phys. **120**, 5396 (2004).

[31] M. Firouzi, K. M. Nezhad, T. T. Tsotsis, and M. Sahimi, J. Chem. Phys. **120**, 8172 (2004).

[32] M. Majumder, N. Chopra, R. Andrewst, and B. J. Hinds, Nature **438**, 44 (2005).

[33] P. A. Thompson and S. Troian, Nature **389**, 360 (1997).

[34] J. Koplik, J. R. Banavar, and J. F. Willemsen, Phys. Fluids A **5**, 781 (1989).

[35] M. Cieplak, J. Koplik, and J. R. Bavanar, Phys. Rev. Lett. **86**, 803 (2001).

[36] J. L. Barrat and L. Bocquet, Phys. Rev. Lett. **82**, 4671 (1999).

[37] A. Jabbarzadeh, J. D. Atkinson, and R. I. Tanner, Phys. Rev. E **61**, 690 (2000).

[38] P. A. Thompson and M. O. Robbins, Phys. Rev. A **41**, 6830 (1990).

[39] R. Khare, P. Keblinski, and A. Yethiraj, International Journal of Heat and Mass Transfer **49**, 3401 (2006).

[40] I. Bitsanis, J. J. Magda, M. tirrell, and H. T. Davis, J. Chem. Phys. **87**, 1733 (1987).

[41] I. Bitsanis, S. A. Somers, H. T. Davis, and M. Tirrell, J. Chem. Phys. **93**, 3427 (1990).

[42] M. Cieplak, J. Koplik, and J. R. Bavanar, Physica A **287**, 153 (2000).

[43] K. P. Travis and D. J. Evans, Phys. Rev. E **55**, 1566 (1997).

[44] X. J. Fan, N. Phan-Thien, N. T. Yong, and D. Xu, Phys. Fluids **14**, 1146 (2002).

[45] X. J. Fan, N. Phan-Thien, N. T. Yong, X. Wu, and D. Xu, Phys. Fluids **15**, 11 (2003).

[46] G. Nagayama and P. Cheng, Int. J. of Heat Mass Transfer **47**, 501 (2004).

[47] V. P. Sokhan, D. Nicholson, and N. Quirke, J. Chem. Phys. **117**, 8531 (2002).

[48] B. D. Todd and D. J. Evans, J. Chem. Phys. **103**, 9804 (1995).

[49] W. Zhu, S. J. Singer, Z. Zheng, and . A. T. Conlisk, Phys. Rev. E **71**, 041501 (2005).

[50] J. Lyklema, S. Rovillard, and J. D. Coninck, Langmuir **14**, 5659 (1998).

[51] A. Jabbarzadeh, J. Atkinson, and R. Tanner, J. Non-Newtonian Fluid Mech. **69**, 169 (1997).

[52] A. Jabbarzadeh, J. Atkinson, and R. Tanner, J. Chem. Phys. **110**, 2612 (1999).

[53] P. A. Thompson and M. O. Robbins, Science: New Series **250**, 792 (1990).

[54] L. Xu, M. G. Sedugh, M. Sahimi, and T. T. Tsotsis, Phys. Rev. Lett. **80**, 3511 (1998).

[55] R. F. Cracknell, D. Nicholson, and N. Quirke, Phys. Rev. Lett. **74**, 2463 (1995).

[56] M. Lisal, W. R. Brennan, and F. R. Siperstein, J. Chem. Phys. **121**, 4901 (2004).

[57] D. R. Wheeler and J. Newman, J. Phys. Chem. B **108**, 18362 (2004).

[58] M. G. Martin and A. P. Thompson, J. Chem. Phys. **114**, 7174 (2001).

[59] G. Arya, H. Chang, and E. J. Maginn, J. Chem. Phys. **115**, 8112 (2001).

[60] G. S. Heffelfinger and F. van Swol, J. Chem. Phys. **100**, 7548 (1994).

[61] A. P. Thompson, D. M. Ford, and G. S. Heffelfinger, J. Chem. Phys. **109**, 6406 (1998).

[62] C. Huang, K. Nandakumar, P. Choi, and L. W. Kostiuk, J. Chem. Phys. **124**, 234701 (2006).

[63] C. Huang, P. Choi, K. Nandakumar, and L. W. Kostiuk, J. Chem. Phys. **126**, 224702 (2007).

[64] I. Bitsanis, T. K. Vanderlick, M. Tirrell, and H. T. Davis, J. Chem. Phys. **89**, 3152 (1988).

[65] R. Qiao and N. R. Aluru, J. Chem. Phys. **118**, 4692 (2003).

[66] L. Cheng, P. Fenter, K. L. Nagy, M. L. Schlegel, and N. C. Sturchio, Phys. Rev. Lett. **87**, 156103 (2001).

[67] A. Aksimentiev and K. Schulten, Proc. Natl. Acad. Sci. USA **101**, 4337 (2004).

[68] S. M. Moghimi, A. C. Hunter, and J. C. Murray, Fed. Amer. Soc. Experimental Biology **19**, 311 (2005).

[69] H. Fenniri, B. Deng, and A. E. Ribbe, J. Am. Chem. Soc. **124**, 11064 (2002).

[70] J. Yang and D. Y. Kwok, J. of Colloid and Interface Science **260**, 225 (2003).

[71] P. Bruesch and T. Christen, J. Applied Physics **95**, 2846 (2004).

[72] J. B. Freund, J. Chem. Phys. **116**, 2194 (2002).

[73] G. Balla and A. Koutselos, J. Chem. Phys. **119**, 11374 (2003).

[74] P. S. Crozier, R. L. Rowley, and D. Henderson, J. Chem. Phys. **114**, 7531 (2001).

[75] R. Qiao and N. R. Aluru, Langmuir **21**, 8972 (2005).

[76] T. Essmann, L. Perera, and M. L. Berkowitz, J. Chem. Phys. **103**, 8577 (1995).

[77] C. Sagui and T. A. Darden, Annu. Rew. Biophys. Biomol. Struct. **28**, 155 (1999).

[78] A. Y. Toukmaji and J. A. B. Jr., Computer Physics Communications **95**, 73 (1996).

[79] E. Spohr, J. Chem. Phys. **107**, 6342 (1997).

[80] L. Monticelli, C. Simoes, L. Belvisi, and G. Colombo, J. Phys.: Condens. Matter **18**, S329 (2006).

[81] T. Darden, D. York, and L. Pedersen, J. Chem. Phys. **98**, 10089 (1993).

[82] E. L. Pollock and J. Glosli, Computer Physics Communications **95**, 93 (1996).

[83] H. Daiguji, P. Yang, and A. Majumdar, Nano Letters **4**, 137 (2004).

[84] R. Qian and N. R. Aluru, J. Chem. Phys. **118**, 4692 (2003).

[85] A. P. Thompson, J. Chem. Phys. **119**, 7503 (2003).

[86] J. R. Ray and H. Zhang, Phys. Rev. E **59**, 4781 (1999).

[87] T. Cagin and J. R. Ray, Phys. Rev. A **37**, 247 (1988).

[88] F. O. Raineri and H. L. Friedman, J. Chem. Phys. **91**, 5642 (1989).

[89] H. J. C. Berendsen, J. P. M. Postma, W. F. van Gunsteren, A. DiNola, and J. R. Haak, J. Chem. Phys. **81**, 3684 (1984).

[90] S. Nose, J. Phys.: Condens. Matter **2**, SA115 (1990).

[91] S. Nose, Phys. Rev. E **47**, 164 (1993).

[92] W. G. Hoover, Phys. Rev. A **31**, 1695 (1985).

[93] H. A. Posch, W. G. Hoover, and F. J. Vesely, Phys. Rev. A **33**, 4253 (1986).

[94] H. C. Andersen, J. Chem. Phys. **72**, 2384 (1980).

[95] C. Braga and K. P. Travis, J. Chem. Phys. **123**, 134101 (2005).

[96] J. B. Sturgeon and B. B. Laird, J. Chem. Phys. **112**, 3474 (2000).

[97] J. M. Haile and H. W. Graben, J. Chem. Phys. **73**, 2412 (1980).

[98] G. J. Martyna, D. J. Tobias, and M. L. Klein, J. Chem. Phys. **101**, 4177 (1994).

[99] M. E. Tuckerman, J. Alejandre, R. Lopez-Rendon, A. L. Jochim, and G. J. Martyna, J. Phys. A: Math. Gen. **39**, 5629 (2006).

[100] C. Braga and K. P. Travis, J. Chem. Phys. **124**, 104102 (2006).

[101] W. G. Hoover, D. J. Evans, R. B. Hickman, A. J. C. Ladd, W. T. Ashurst, and B. Moran, Phys. Rev. A **22**, 1690 (1980).

[102] G. J. Martyna, M. E. Tuckerman, D. J. Tobias, and M. L. Klein, Molec. Phys. **87**, 1117 (1996).

[103] M. E. Tuckerman, Y. Liu, and G. J. Martyna, J. Chem. Phys. **115**, 1678 (2001).

[104] D. Chandler, J. D. Weeks, and H. C. Andersen, Science **220**, 787 (1983).

[105] D. Chandler and J. D. Weeks, Phys. Rev. Lett. **25**, 149 (1970).

[106] J. D. Weeks and D. Chandler, J. Chem. Phys. **54**, 5237 (1971).

[107] H. C. Andersen, J. D. Weeks, and D. Chandler, Phys. Rev. A **4**, 1597 (1971).

[108] L. Verlet and J. J. Weis, Phys. Rev. A **5**, 939 (1972).

[109] D. Beb-Amotz and G. Stell, J. Phys. Chem. B **36**, 2710 (1962).

[110] M. Bishop, A. Masters, and J. H. R. Clarke, J. Chem. Phys. **110**, 11449 (1999).

[111] T. Yamaguchi, Y. Kimura, and N. Hirota, J. Chem. Phys. **111**, 4169 (1999).

[112] S. Hess and M. Kroger, Phys. Rev. E **61**, 4629 (2000).

[113] L. Verlet, Phys. Rev. **165**, 201 (1968).

[114] L. Li, D. Bedrov, and G. D. Smith, Phys. Rev. E **71**, 011502 (2005).

[115] S. R. Challa and F. V. Swol, Phys. Rev. E **73**, 016306 (2006).

[116] A. J. Markvoort and P. A. Hilbers, Phys. Rev. E **71**, 066702 (2005).

[117] J. Delhommelle and P. T. Cummings, Phys. Rev. E **72**, 172201 (2005).

[118] E. Akhmatskaya, B. D. Todd, P. J. Daivis, D. J. Evans, K. E. Gubbins, and L. A. Pozhar, J. Chem. Phys. **106**, 4684 (1997).

[119] G. C. Maitland, M. Rigby, E. B. Smith, and W. A. Wakeham, *Intermolecular Forces: Their Origin and Determination* (Clarendon Press, Oxford, New York, 1981).

[120] S. Nose, J. Chem. Phys. **81**, 511 (1984).

[121] B. L. Holian and A. F. Voter, Phys. Rev. E **52**, 2338 (1995).

[122] M. J. Nuevo, J. Morales, and D. M. Heyes, Phys. Rew. E **58**, 5845 (1998).

[123] W. Yu, Z. Q. Wang, and D. Stroud, Phys. Rew. B **54**, 13946 (1996).

[124] M. Guthold, X. Zhu, C. Rivetti, G. Yang, , N. H. Thomson, S. Kasas, H. G. Hansma, B. Smith, P. K. Hansma, et al., Biophys. J. **77**, 2284 (1999).

[125] M. W. Mahoney and W. L. Jorgensen, J. Chem. Phys. **114**, 363 (2001).

[126] J. H. Irving and J. G. Kirkwood, J. Chem. Phys. **18**, 817 (1950).

[127] J. Petravic, Phys. Rew. B **72**, 014108 (2005).

[128] J. Weng, S. Park, J. R. Lukes, and C. Tien, J. Chem. Phys. **113**, 5917 (2000).

[129] A. Eisenstein and N. S. Gingrich, Physical Review **62**, 261 (1942).

[130] B. J. Yoon, M. S. Jhon, and H. Eyring, Proc. Natl. Acad. Sci. USA **78**, 6588 (1981).

[131] S. H. Lee, D. K. Park, and D. B. Kang, Bull Korean Chem. Soc. **24**, 178 (2003).

[132] M. Kawata and U. Nagashima, Chem. Phys. Lett. **340**, 165 (2001).

[133] A. Mansouri, C. Scheuerman, S. Bhattacharjee, D. Kwok, and L. Kostiuk, J. Colloid and Interface Science **292**, 567 (2005).

[134] B. A. Lowry, S. A. Rice, and P. Gray, J. Chem. Phys. **40**, 3673 (1964).

[135] J. P. Boon, J. C. Legros, and G. Thomaes, Physica **33**, 547 (1967).

[136] A. D. Bock, W. Grevendonk, and W. Herreman, Physica **37**, 227 (1967).

[137] J. Hellemans, H. Zink, and O. V. Paemel, Physica **40**, 395 (1970).

[138] R. DeVane, C. Ridley, R. W. Larsen, B. Space, P. B. Moore, and S. I. Chan, Boiphys. J. **85**, 2801 (2003).

[139] I. R. McDonald and K. Singer, Discuss. Faraday Soc. **43**, 40 (1967).

[140] S. C. Jain and V. S. Nanda, J. Phys. C: Solid St. Phys. **4**, 3045 (1971).

[141] G. Drazer, J. Koplik, and A. Acrivos, Phys. Rev. Lett. **89**, 244501 (2002).

[142] J. Naghizadeh and S. A. Rice, J. Chem. Phys. **36**, 2710 (1962).